APPEARANCE OF WOVEN CLOTH

A Dissertation

Presented to the Faculty of the Graduate School

of Cornell University

in Partial Fulfillment of the Requirements for the Degree of

Doctor of Philosophy

by

Piti Irawan

January 2008

© 2008 Piti Irawan

ALL RIGHTS RESERVED

APPEARANCE OF WOVEN CLOTH

Piti Irawan, Ph.D.

Cornell University 2008

The appearance of a particular fabric is produced by variations in both large-scale reflectance and small-scale texture as the viewing and illumination angles change across the surface. This thesis presents a study of the reflectance and texture of woven cloth that aims to identify and model the most important optical features of cloth appearance. New measurements are reported for a range of fabrics including natural and synthetic fibers as well as staple and filament yarns. A new scattering model for woven cloth is introduced that describes the reflectance and the texture based on an analysis of specular reflection from the fibers. Unlike data-based models, our procedural model requires no image data. It can handle a wide range of fabrics using a small set of physically meaningful parameters that describe the characteristics of the fibers, the geometry of the yarns, and the pattern of the weave. The model is validated against the measurements and by comparisons to high-resolution video of the real fabrics.

BIOGRAPHICAL SKETCH

The author was born on January 23, 1980 in Jakarta, Indonesia. From 1998 to 2002 he studied at Purdue University, where he received a bachelor's degree in Computer Science with a minor in Asian Studies. He then joined the Computer Science Ph.D. program at Cornell University and spent much of the time between 2002 and 2007 thinking about Computer Graphics. Out of personal interest, he pursued a graduate minor in Management.

for Anita

ACKNOWLEDGEMENTS

I would like to give my thanks to my advisor, Steve Marschner, for the support and encouragement he gave me over the course of my graduate study. This dissertation is the product of his confidence in me and the time he spent guiding me along the way. I would also like to thank my minor advisor, Wesley Sine, whose fun and instructive classes broaden my horizon and kept me sane. I am honored to have excellent people in my committee; Don Greenberg has been like a grandfather to me and the insights Joe Halpern and Johannes Gehrke brought from outside computer graphics were invaluable. I would like to thank Kavita Bala for being a proxy for Johannes and Kelly Patwell and Ganesh Ramanarayanan for helping me with the forms required by the Graduate School.

I had the pleasure of working with many wonderful people. I thank Jim Ferwerda for his guidance during the early years of my stay at Cornell. I thank Bruce Walter, Steve Westin, Kavita Bala, and Doug James for their feedbacks on my work. I thank Ken Torrance for lending his laboratory. Thanks to Hurf Sheldon and Martin Berggren for assisting me with cluster use and keeping my computer connected and running. Thanks to Cay Wilson for helping me with my Computer Science account. Thanks to Kelly Patwell, Becky Stewart, Linda Stephenson, and Peggy Anderson for administrative support. I am deeply indebted to my fellow students Jon Kaldor and Jon Moon; one Jon created the model of the platform used in the turntable sequence seen in Chapter 9 and the other helped me countless times with many aspects of this work. Thanks also to Ganesh Ramanarayanan, Kamal Aboul-Hosn, and Milind Kulkarni for sharing an office during my first year at Cornell.

Special thanks to my undergraduate mentor, Sally Hastings, whose guidance and kindness I recall whenever I think of Purdue.

I owe my deepest gratitude to my parents and my wife, Anita. Their support, encouragement, patience, and unconditional love are what kept me going.

This work was supported by the National Science Foundation through the CAREER grant CCF-0347303 and by an Alfred P. Sloan Research Fellowship.

TABLE OF CONTENTS

LIST OF TABLES

LIST OF FIGURES

LIST OF ALGORITHMS

LIST OF ABBREVIATIONS

BRDF	bidirectional reflectance distribution function
BTF	bidirectional texture function

LIST OF SYMBOLS

a	radius of the cross section of the yarn segment
A	attenuation function
α	uniform scattering
β	forward scattering
δ	filament smoothing
f_c	circular phase function
f_p	phase function
f_r	bidirectional reflectance distribution function (BRDF)
f_s	scattering function
G	geometry factor
$\mathbf{h}$	half vector
k_d	diffuse coefficient
k_s	specular coefficient
κ	spine curvature parameter
l	length of segment rectangle
$\mathbf{n}$	normal to the yarn surface
ω_i	incident direction
ω_r	exitant direction
ψ	fiber twist angle
$\hat{r}$	axis ratio
R	radius of curvature of the spine curve
$\mathbf{t}$	tangent to the fiber direction
T	bidirectional texture function (BTF)
$u_{\max}$	maximum inclination angle
w	width of segment rectangle
$\mathbf{x}_0$	spine curve

Chapter 1

Introduction

Cloth is an important material to render convincingly because it appears regularly in computer graphics scenes, especially those involving virtual humans in everyday environments. Fabric appearance is also important in applications of computer graphics in the textile, garment, and fabric care industries. Our goal is to develop a simple, easy-to-use procedural model for the appearance of cloth that efficiently captures the important features of its appearance based on physically meaningful parameters.

In scenes rendered for computer graphics, two aspects of cloth appearance are important to capture in an appearance model. The directional reflectance, which describes the total light reflected from a large (at least several millimeters across) area of fabric, determines the overall shading. At the same time, the texture of the weave pattern is visible in more close-up views. Each weave has its own distinctive texture that is an important part of its appearance.

We assume that a general-purpose cloth model needs to be realistic at image resolutions up to a few pixels per yarn, when yarns are resolved but not individual fibers. Resolutions higher than this are in the realm of macrophotography and need to be rendered using a complete model of the cloth's three-dimensional structure.

This work makes two contributions: a set of measurements and a model to fit them. We present new, detailed measurements of the anisotropic bidirectional reflectance distribution function (BRDF) of six fabrics representing four textile fibers and the three most common weave patterns, as well as texture measurements for some of the fabrics. To study the appearance of the fabrics in context, we also took high-resolution video of the fabrics in a draped configuration under controlled conditions.

Our second contribution is a new reflection model for woven fabrics. The model is based on an analysis of specular scattering from fibers that are spun into yarns and then woven into fabric based on a given weaving pattern. Its parameters are all physically meaningful, describing the scattering properties of the fibers and the geometry of the yarns and weave. The model predicts both BRDF and, by a simple mapping of specular highlights onto the cloth surface, the texture of specular highlights. It defines a spatially varying BRDF that fits into standard realistic rendering systems and can be integrated over incident light using standard methods.

Our model, then, is a physics-based model. In contrast, it is popular to render cloth using data-based approaches, such as bidirectional texture functions (BTFs). While physics-based models are derived from analysis of first principles, data-based models gather the reflection data by taking many pictures of the material to be modeled, store those data in a database, and query the database for the appropriate reflection data at render time. We shall compare the two distinct approaches in Chapter 3.

We validate our model against our measurements and find that it predicts the most important features both of the directional reflectance distribution and of the evolution of texture with viewing and illumination angle. Because all the directional variation in the model is due to specular reflection, an implication of this work is that specular reflection plays a more important role in the appearance of even quite matte fabrics than previously appreciated.

Chapter 2

Background

2.1 Cloth

Cloth is an indispensable material in life, with applications ranging from clothing to industrial uses. For some applications, the quality of cloth is judged on its appearance; for others, it is based on its durability, strength, and thermal resistance. These myriad forms of cloth arise from the variety of textile fibers and production methods used in the creation of the fabric. Because of their importance, in this section we will briefly describe the different fibers and manufacturing processes used in the production of cloth. Further information on cloth can be found in [24].

2.1.1 Textile fibers

Fibers used in cloth production can be classified into four broad categories based on their origin: animal, plant, mineral, and synthetic.

Animal fibers mostly come from hair or fur. Wool is the fiber derived from the hair of domestic sheep. Wool fabrics are thicker than other fabrics and used in clothing, carpet, felt, insulation, and upholstery. Cashmere wool (also known as pashmina) is derived from the hair of Cashmere goats and known for its incredibly soft fibers. Cashmere fabrics are prized as light-weight insulators without bulk and are fashioned into hats, socks, scarves, sweaters, and winter coats. Mohair is derived from the hair of Angora goats. In addition to durability and insulating properties, mohair is also known for its luster and sheen and used in socks, scarves, sweaters, coats, suits, and carpet, among others. Hair from alpaca, Angora rabbit, camel, llama, and vicuña is also harvested and used in a variety of clothing. Unlike wool, silk is derived from the cocoons of Chinese silkworm larvae. Silk is mainly known for its high luster, resulting from its triangular cross section [6, 26]. Silk fabrics are commonly used in clothing and furnishing.

Cotton fibers are strong, durable, and highly absorbent fibers harvested from cotton plants. Cotton has many uses and is the most widely used natural-fiber in clothing as well as "the single most important textile fiber in the world, accounting for nearly 40 percent of total world fiber production" [41]. Flax fibers come from the bast or skin of the stem of flax plant. Yarns and fabrics made from flax fibers are called linen. Linen fabrics are lustrous, strong, durable, stiff, often come with characteristic knots along the length of the yarns, and are used as furnishings, summer clothing, and canvasses. Other plant-based fibers include: coir, hemp, jute, piña, ramie, and sisal.

Mineral fibers, such as asbestos, basalt fiber, glass fiber, and metal fiber, are used mainly to manufacture technical textiles for non aesthetic purposes. These include insulators, spacesuits, cables, reinforcement fibers, and construction materials.

Unlike mineral fibers, synthetic fibers are mainly used in the production of clothing. Polyester is one of the most commonly used synthetic fibers in the world. Because of its wrinkle resistance, it is often used in clothing and furnishing in place of or with cotton. Nylon has the ability to vary its luster and was made as a synthetic replacement for silk. Nylon fibers are used in the production of women's stockings, carpets, guitar strings, and auto parts. Acrylic fibers are similar in appearance and feeling to wool and often used to imitate the more expensive cashmere. Other synthetic fibers include: aramid, Ingeo, Lurex, olefin, and spandex.

Fibers can also be classified into two types: staple fibers and filament fibers. Staple fibers—such as cotton and wool—are relatively short. To make staple yarns, staple fibers are twisted around one another so that they hold together by friction [49]. Because of this twisted structure, the fibers on the surface of a fabric made from staple yarns appear in a diagonal arrangement, usually with alternating directions for exposed parts of the warp and weft. We use the term "staple" to refer to twisted staple yarn.

In contrast, filament fibers—such as silk and many synthetic fibers—are very long. As the result, filament yarns do not need to be twisted together in order to hold together. In this case the fibers lie parallel to the overall axis of the yarn. We use the term "filament" to refer to untwisted filament yarn.

2.1.2 Production methods

Several methods exist to transform a collection of fibers into a piece of cloth, among them: weaving, knitting, and bonding. Weaving is the process of interlacing two sets of parallel yarns, known as the *warp* and *weft*, at right angles to each other to form a piece of cloth. Knitting and crocheting involve pulling loops of yarn (called stitches) through other loops of yarn for form a piece of cloth. Bonding is the process of joining fibers together through the use of an adhesive agent (for example, applying heat or chemical binders) to form a piece of cloth.

Each of these methods produces cloth with different characteristics. Weaving is the most common cloth production method and woven cloth makes up the majority of commercial fabrics. Depending on the textile fiber and weave pattern used, woven cloth can have very different appearances, from the matte denim found in blue jeans to the shiny silk charmeuse. Knitwear tends to be bulkier (with the exception of those made from very fine fibers such as cashmere) with very distinctive texture. Because of the arrangement of yarns, knitwear is also more elastic than woven cloth. Felt—cloth made from bonding processes—is tough and matte in appearance and often used to manufacture rugs and tents.

In this work, we confine our attention to the largest and most diverse class of cloth: woven cloth. We shall briefly look at the structure of woven cloth in more details in the next section.

2.2 Structure of Woven Cloth

As stated earlier, woven cloth is constructed by interlacing two sets of parallel yarns, known as the *warp* and *weft*, at right angles to each other. In the process of weaving, warp yarns are raised or lowered and weft yarns (also known as *fillings*) are inserted in the space that resulted. Figure 2.1 shows a loom with the warp yarns before the weft yarns are inserted. The pattern in which the warp and weft are interleaved varies greatly, but the majority of fabrics are made in one of the three simplest weave patterns: plain weave, twill, and satin [34]. Some examples of commonly found woven fabrics can be seen in Table 2.1. The weave patterns of the some of these fabrics can be seen in Figure 5.1.

Weaving creates a complex, regular geometry that can be considered, for purposes of appearance, to consist of a repeating pattern of visible segments of yarn. A warp yarn segment begins where the yarn emerges from behind one weft yarn, and continues until it next passes below another weft yarn (and similarly for weft segments). Inter-yarn forces make segments bend into curved shapes, convex toward the visible side. The degree of curvature is important to the appearance, and it depends on the stiffness of the yarn, the length of the segment, and the

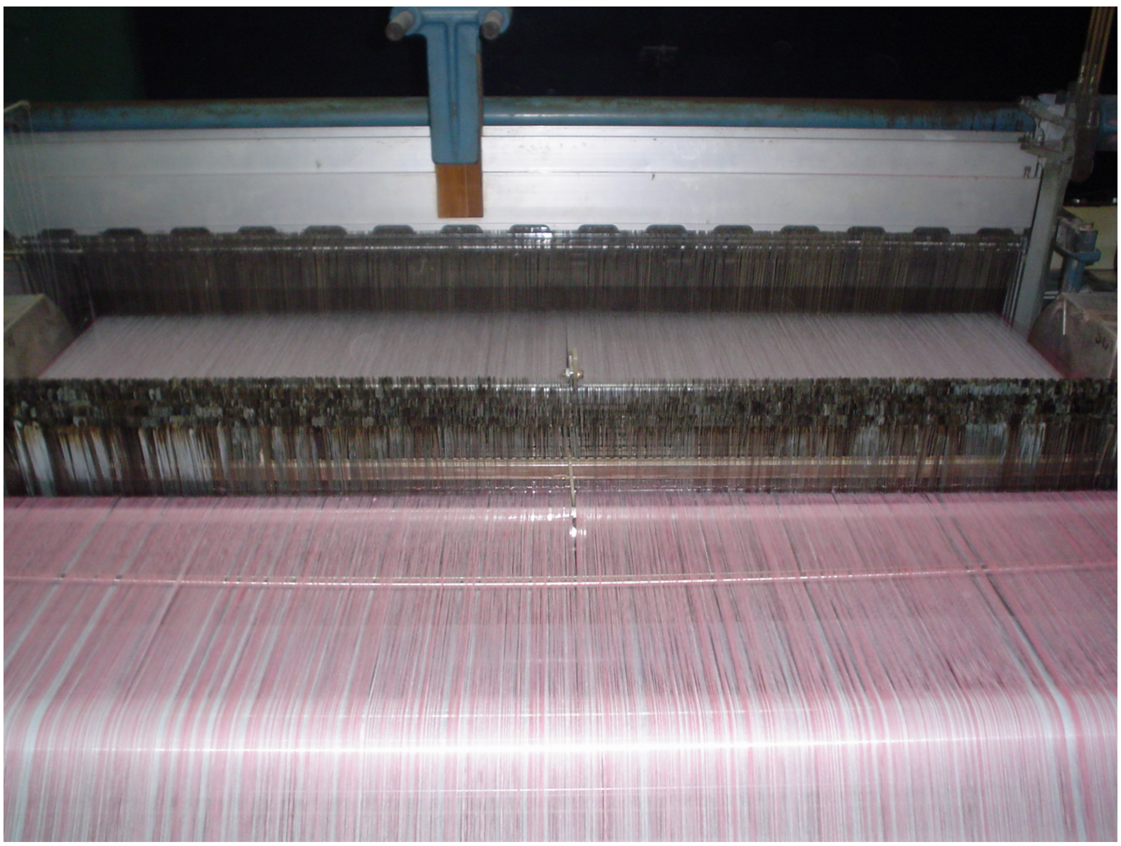

Figure 2.1: Loom with the warp yarns before the weft yarns are inserted.

Table 2.1: Examples of commonly found woven fabrics.

Woven fabric	Fiber	Type	Weave pattern
Batiste	cotton, wool, polyester	staple	plain weave
Broadcloth	wool	staple	plain weave, twill weave
Canvas	cotton	staple	plain weave
Chambray	cotton	staple	plain weave
Charmeuse	silk, polyester	filament	satin weave
Chiffon	silk	filament	plain weave
Chino	cotton	staple	twill weave
Denim	cotton	staple	twill weave
Duck	cotton	staple	plain weave
Gabardine	wool	staple	twill weave
Gingham	cotton	staple	plain weave
Muslin	cotton	staple	plain weave
Organdy	cotton	staple	plain weave
Organza	silk	filament	plain weave
Oxford	cotton	staple	plain weave
Poplin	cotton	staple	plain weave
Sateen	cotton	staple	satin weave
Satin	silk, nylon, polyester	filament	satin weave
Serge	wool	staple	twill weave
Shantung	silk	filament	plain weave
Taffeta	silk	filament	plain weave
Tweed	wool	staple	plain weave, twill weave
Twill	cotton, wool	staple	twill weave

tension in the yarn and in the other yarns it interacts with. For instance, satin and twill weaves include long warp segments that will tend to lie flat and exhibit lower curvature than the shorter weft segments. A plain weave fabric may have similar yarn properties and tension in the warp and weft, leading to warp and weft segments with similar shape (e. g., the polyester fabric we measured); or it may be made with dissimilar yarns and/or tension, causing dissimilar segment shapes (e. g., the silk shantung fabric).

2.3 Mathematical Preliminaries

Here we present notational convention and mathematical results in common use in later chapters.

In this work, vectors in a vector space $\mathbb{R}^n$ are denoted $\mathbf{v} = (\mathbf{v}_1, \mathbf{v}_2, \ldots, \mathbf{v}_n)^T$. Vectors in $\mathbb{R}^3$ are also denoted $\mathbf{v} = (\mathbf{v}_x, \mathbf{v}_y, \mathbf{v}_z)^T$ for convenience.

2.3.1 Rotation matrices

Let $R_x(\theta)$, $R_y(\theta)$, and $R_z(\theta)$ be the three matrices that rotates a vector by a counterclockwise angle θ about the x-, y-, and z-axes, respectively [48].

$$R_x(\theta) = \begin{bmatrix} 1 & 0 & 0 \\ 0 & \cos\theta & -\sin\theta \\ 0 & \sin\theta & \cos\theta \end{bmatrix}$$

$$R_y(\theta) = \begin{bmatrix} \cos\theta & 0 & \sin\theta \\ 0 & 1 & 0 \\ -\sin\theta & 0 & \cos\theta \end{bmatrix}$$

$$R_z(\theta) = \begin{bmatrix} \cos\theta & -\sin\theta & 0 \\ \sin\theta & \cos\theta & 0 \\ 0 & 0 & 1 \end{bmatrix}$$

2.3.2 Trigonometric identities

In this subsection we list trigonometric identities that are used in later chapters.

The first one is the simple inverse tangent identity:

$$\arctan(b, a) = \arctan(-a, b) + \frac{\pi}{2} \tag{2.1}$$

where $-\pi < \arctan(y, x) \leq \pi$ is the usual generalization of $-\pi/2 < \arctan(y/x) < \pi/2$. In many programming languages, this function is `atan2(y,x)`.

For any a and b, the following is true.

$$\begin{aligned} &\sqrt{a^2+b^2}\cos(x - \arctan(b, a)) \\ &= \sqrt{a^2+b^2}(\cos x \cos(\arctan(b, a)) + \sin x \sin(\arctan(b, a))) \\ &= \sqrt{a^2+b^2}\left(\cos x \tfrac{a}{\sqrt{a^2+b^2}} + \sin x \tfrac{b}{\sqrt{a^2+b^2}}\right) \\ &= a\cos x + b\sin x \end{aligned} \tag{2.2}$$

2.3.3 Conic sections

Ellipse

The formulae referenced in this subsection are standard formulae for ellipses; they and further information on ellipses can be found in [47]. Parametric equations for an ellipse are as follows.

$$\begin{aligned} x &= \hat{a}\cos t \\ y &= \hat{b}\sin t \end{aligned} \tag{2.3}$$

where $\hat{a}$ and $\hat{b}$ are the semimajor axis and semiminor axis of the ellipse, respectively.

The tangential angle $u(t)$ of the ellipse is given by

$$u(t) = \arctan\left(\frac{\hat{a}}{\hat{b}}\tan t\right)$$

and therefore

$$t(u) = \arctan\left(\frac{\hat{b}}{\hat{a}}\tan u\right) \tag{2.4}$$

The radius of curvature $R(t)$ of the ellipse is given by

$$R(t) = \frac{(\hat{b}^2\cos^2 t + \hat{a}^2\sin^2 t)^{1.5}}{\hat{a}\hat{b}} \tag{2.5}$$

Parabola

The formulae referenced in this subsection are standard formulae for parabolas; they and further information on parabolas can be found in [44]. Parametric equations for a parabola are as follows.

$$\begin{aligned} x &= -\hat{b}t^2 \\ y &= 2\hat{b}t \end{aligned} \tag{2.6}$$

where $\hat{b}$ is the distance from the vertex to the directrix or focus.

The tangential angle $u(t)$ of the parabola is given by

$$u(t) = \arctan t$$

and therefore

$$t(u) = \tan u \tag{2.7}$$

The radius of curvature $R(t)$ of the parabola is given by

$$R(t) = 2\hat{b}(1 + t^2)^{1.5} \tag{2.8}$$

Hyperbola

The formulae referenced in this subsection are standard formulae for hyperbolas; they and further information on hyperbolas can be found in [43]. Parametric equations for a hyperbola are as follows.

$$\begin{aligned} x &= \hat{a}\cosh t \\ y &= \hat{b}\sinh t \end{aligned} \tag{2.9}$$

where $\hat{a}$ and $\hat{b}$ are the semimajor axis and semiminor axis of the hyperbola, respectively.

The tangential angle $u(t)$ of the hyperbola is given by

$$u(t) = -\arctan\left(\frac{\hat{a}}{\hat{b}}\tanh t\right)$$

and therefore

$$t(u) = -\tanh^{-1}\left(\frac{\hat{b}}{\hat{a}}\tan u\right) \tag{2.10}$$

The radius of curvature $R(t)$ of the hyperbola is given by

$$R(t) = -\frac{(\hat{b}^2\cosh^2 t + \hat{a}^2\sinh^2 t)^{1.5}}{\hat{a}\hat{b}} \tag{2.11}$$

2.3.4 Dot and cross products

Let $\mathbf{u}$ and $\mathbf{v}$ be vectors in $\mathbb{R}^3$. The dot product of $\mathbf{u}$ and $\mathbf{v}$ can be defined as follows:

$$\mathbf{u}\cdot\mathbf{v} = |\mathbf{u}||\mathbf{v}|\cos\theta, \tag{2.12}$$

where $|\mathbf{u}|$ and $|\mathbf{v}|$ are the norms of $\mathbf{u}$ and $\mathbf{v}$ respectively and θ is the angle between the vectors. More information on the dot product can be found in [46].

The cross product of $\mathbf{u}$ and $\mathbf{v}$ can be defined as follows:

$$\mathbf{u}\times\mathbf{v} = \hat{x}(u_y v_z - u_z v_y) - \hat{y}(u_x v_z - u_z v_x) + \hat{z}(u_x v_y - u_y v_x), \tag{2.13}$$

where $(\hat{x}, \hat{y}, \hat{z})$ is a right-handed orthonormal basis. More information on the cross product can be found in [45].

The vector triple product identity (also known as the Lagrange's formula or the BAC-CAB identity) [23] relates dot products and cross products of vectors in $\mathbb{R}^3$.

$$\mathbf{a} \times (\mathbf{b} \times \mathbf{c}) = \mathbf{b}(\mathbf{a} \cdot \mathbf{c}) - \mathbf{c}(\mathbf{a} \cdot \mathbf{b}) \tag{2.14}$$

2.3.5 Gauss map and Gauss sphere

The Gauss map is a function $N : M \to S^2$ that maps an oriented surface M in Euclidean space $\mathbb{R}^3$ to the unit sphere S^2 in $\mathbb{R}^3$. The map associates every point on M to its oriented unit normal vector in S^2 . Further information on Gauss map can be found in [18].

The Gauss sphere is related to the Gauss map. In a Gauss sphere, unit vectors in $\mathbb{R}^3$—not limited to normal vectors of points on a surface—are mapped to a unit sphere S^2 in $\mathbb{R}^3$. Gauss sphere is a convenient construct that allows us to visualize the interactions of the various vectors that make up our models; the Gauss spheres are used in Chapters 6 (see Figures 6.3, 6.4, 6.5, and 6.6) and 7 (see Figures 7.3, 7.4, 7.5, and 7.7).

2.3.6 Matrix calculus

The material in this subsection was adapted from [14]. A slightly different approach to matrix calculus is explored in [8].

Let x and y be scalars and let $\mathbf{x} = (\mathbf{x}_1, \mathbf{x}_2, \ldots, \mathbf{x}_n)^T$ and $\mathbf{y} = (\mathbf{y}_1, \mathbf{y}_2, \ldots, \mathbf{y}_m)^T$ be vectors.

The derivative of $\mathbf{y}$ with respect to $\mathbf{x}$ is the $n \times m$ matrix

$$\frac{\partial \mathbf{y}}{\partial \mathbf{x}} \triangleq \begin{bmatrix} \frac{\partial \mathbf{y}_1}{\partial \mathbf{x}_1} & \frac{\partial \mathbf{y}_2}{\partial \mathbf{x}_1} & \dots & \frac{\partial \mathbf{y}_m}{\partial \mathbf{x}_1} \\ \frac{\partial \mathbf{y}_1}{\partial \mathbf{x}_2} & \frac{\partial \mathbf{y}_2}{\partial \mathbf{x}_2} & \dots & \frac{\partial \mathbf{y}_m}{\partial \mathbf{x}_2} \\ \vdots & \vdots & \ddots & \vdots \\ \frac{\partial \mathbf{y}_1}{\partial \mathbf{x}_n} & \frac{\partial \mathbf{y}_2}{\partial \mathbf{x}_n} & \dots & \frac{\partial \mathbf{y}_m}{\partial \mathbf{x}_n} \end{bmatrix} \tag{2.15}$$

The derivative of y with respect to $\mathbf{x}$ is the vector

$$\frac{\partial y}{\partial \mathbf{x}} \triangleq \begin{bmatrix} \frac{\partial y}{\partial \mathbf{x}_1} \\ \frac{\partial y}{\partial \mathbf{x}_2} \\ \vdots \\ \frac{\partial y}{\partial \mathbf{x}_n} \end{bmatrix} \tag{2.16}$$

The derivative of $\mathbf{y}$ with respect to x is the row vector

$$\frac{\partial \mathbf{y}}{\partial x} \triangleq \begin{bmatrix} \frac{\partial \mathbf{y}_1}{\partial x} & \frac{\partial \mathbf{y}_2}{\partial x} & \dots & \frac{\partial \mathbf{y}_m}{\partial x} \end{bmatrix} \tag{2.17}$$

As a corollary,

$$\begin{aligned} \tfrac{\partial}{\partial \mathbf{x}}|\mathbf{x}| &= \tfrac{\partial}{\partial \mathbf{x}}\sqrt{x_1^2 + \cdots + x_n^2} \\ &= \tfrac{1}{2}(x_x^2 + x_y^2 + x_z^2)^{-\frac{1}{2}} \left[2x_1 \ \dots \ 2x_n\right] \\ &= \tfrac{\mathbf{x}^T}{|\mathbf{x}|} \end{aligned}$$

Chapter 3

Prior Work

While most of the work on modeling cloth for computer graphics has focused on motion rather than appearance, several researchers have addressed the problem of rendering cloth.

3.1 BRDF and BTF

The fundamental descriptions of appearance used for rendering cloth are the *bidirectional reflectance distribution function* (BDRF) and the *bidirectional texture function* (BTF). The BRDF $f_r(\omega_i, \omega_r)$ is the ratio of radiance exiting a surface in the exitant direction ω_r to the irradiance arriving on the surface from an infinitesimal solid angle about the incident direction ω_i [33, 12]. The BRDF is symmetric with respect to exchanging its arguments; that is, $f_r(\omega_i, \omega_r) = f_r(\omega_r, \omega_i)$. The BTF is a similar description but for texture: it gives the texture that appears in an image of a surface as a function of the incident and reflection directions [7]. Since BRDF is a function of four variables, BTF is a function of six variables—the additional two specify the texture coordinate.

3.2 Measurements and Studies of Cloth BRDF

In the textile research community, luster was defined as a function of the ratio between specular reflection and diffuse reflection [22]. Buck and McCord provide some of the earliest quantitative measurements of luster of textiles [4]. Among their findings are: fabrics made of filament fibers exhibit the greatest luster, yarn twist tends to reduce luster, and knitted fabrics exhibit less luster than woven fabrics.

Tao and Sirikasemlert measured specular reflection from single-jersey knitted fabrics made from monofilament yarns and developed a theoretical model of the reflection based on three parameters: fiber refractive index, yarn cross-sectional shape, and incident light angle [40]. The model was later expanded to knitted fabrics made from twistless multifilament yarns [39]. Both models were developed to match goniophotometric measurements and no texture analysis or rendering was done.

In the computer vision community there is work involving reflection from fibers and woven materials. Lu et al. [27] presented a measurement and study of velvet BRDF. They discovered that velvet cloth has a matte and diffuse reflectance with specular reflectance near grazing angles and retroreflection. The same team [28] later presented an analysis of the shape of specular highlights on fiber-covered surfaces based on geometric considerations similar to those we used to derive our model.

Ngan et al. [32] measured velvet and two satin fabrics and fit analytical BRDF models to the measurements. They observed that the BRDFs of velvet and satin "far exceed the expressive power of simple analytical models" and approximated the cloth BRDF using a microfacet-based BRDF generator [3] with a tabulated microfacet distribution based on the measurements. This, however, requires high resolution measurements of the cloth being modeled.

Pont and Koenderink [36] presented a qualitative analysis of reflection from woven structures, emphasizing the double-peak effect that is observed in some woven structures (including the polyester cloth measured in the present paper).

That work, unlike ours, did not aim to present a complete BRDF model or to predict texture.

3.3 Modeling Cloth BRDF

Cloth often appears as an example of an unusual BRDF. Westin et al. [50] computed BRDFs for velvet and nylon by ray tracing models of the microstructure. In that work velvet was modeled as a collection of thin cylinders with randomly perturbed orientation. Yarns in the nylon cloth were modeled as flat cylinders and were interwoven according to the standard plain weave pattern.

Similarly, Volevich et al. [42] ray traced a plane of interwoven yarns to study scattering from a piece of artificial silk. Unlike Westin et al. [50], in that work the yarns were modeled as bundles of textile fibers, which in turn were modeled as very long and thin cylinders parallel to one another. These, therefore, were attempts to understand the appearance of woven (filament) cloth by explicitly modeling the structure of the cloth.

In their work on efficient rendering of spatial bidirectional reflectance distribution functions (SBRDF), McAllister et al. [30] measured anisotropic upholstery fabric and represented each texel using two Lafortune BRDF lobes.

Ashikhmin et al. [3] dispensed with explicit models and used a combination of two cylindrical Gaussian slope distributions to model satin as an example of their microfacet-based BRDF generator. Velvet was another example of their microfacet-based BRDF generator and it was modeled using an "inverse Gaussian" heightfield.

Yasuda et al. [52] presented a microfacet-based model that is compared to incidence-plane reflection measurements.

3.4 Modeling Cloth Texture

Other works have focused on the structure and texture of fabric. Adabala et al. [1] presented a method based on a microfacet model and procedural textures that is capable of rendering cloth with a variety of weave patterns at different levels of detail. Without data to support the model, however, it is hard to judge its correctness. Furthermore, while the model is procedural, its parameters are not physically meaningful and, as the result, fabric's appearance is not connected to its structure. Our understanding of the structure of woven cloth allows our model to produce and explain phenomena such as the double-peak effect described earlier.

Glassner, in a series of three articles [15, 16, 17], presented a way to compactly describe weave patterns and showed a digital loom to experiment with the rich and interesting patterns found in woven cloth.

Drago and Chiba [11] modeled woven painting canvases with spline surfaces shaded by a procedural texture.

Xu et al. [51] used a volume rendering approach called *lumislice* rendering to produce realistic close-ups of coarse knit fabrics. Their approach is related to our work because both consider a yarn as made up of helical fibers and take a volumetric approach to calculating the scattered light. The goals are different, however: our aim is an analytical model that works when yarns are barely resolved, whereas the lumislice was designed for closeups in which yarns are well resolved and fibers are prominent. Also, we focus on specular, rather than diffuse, reflection. This approach to modeling the texture of knitwear—modeling the mesostructure of the knitwear and using volumetric techniques to model the self-shadowing due to the thicker yarns used in knitted fabrics—are used in many other works [19, 20, 31, 9, 10, 5].

3.5 Data-based Approaches to Cloth Modeling

Because of its unusual BRDF and texture, simple analytical models often fail to represent cloth appearance well. One class of approach in cloth modeling abandons analytical models in favor of data-based ones. Data-based models such as [9] and [37] start by taking many pictures of the cloth to be modeled and store the images as compressed bidirectional texture function (BTF) [7] data in a database. At render time, the appropriate BTF data are then retrieved from the database.

By their nature, data-based models require large storage space and are able to model only the specific fabrics that have been captured and stored in the database. Although current research is beginning to address the problems of editing BTFs [25, 35], measurements of very similar materials will continue to be required, and the BTFs still cannot be controlled by parameters describing the structure of the fabrics. Given BTF data for a particular cloth, however, data-based models can reproduce that particular fabric very well. Data-based models, therefore, are well suited to situations where analytical models of the material to be modeled aren't available. We aim to extend the range of analytical models by making one for woven cloth available.

Because our model was built from first principles and is analytical in nature, it doesn't require any data at render time. Measurements of cloth BRDF and texture discussed in this work were used only for study and verification of our model; the model itself does not require any data.

Chapter 4

Overview of the Model

The idea behind our model is as follows: yarn segments are modeled as curved cylinders (Figure 4.1) made of spiralling fibers that reflect light specularly. As we will see later, specular reflection from the fibers forms a curved specular highlight on the surface of the segment. To get the total contribution to the BRDF from specular reflection, we can either integrate the reflection along the yarn segment (u direction) or around the yarn segment (v direction). Thus our BRDF model has two equations depending on how we choose to integrate the reflection.

The amount of light that is reflected at one point on the specular reflection curve is $G_u f_c A$ or $G_v f_c A$ (depending on how we choose to integrate the reflection), which consists of the following terms:

1. The geometry factor G_u or G_v. This is determined by the geometry of the yarn segment (including radius of curvature, size of the yarn segment, and change in specular reflection with change in illumination direction) and is discussed in Section 7.4.

2. The phase function f_c. This function describes the local behavior of the fibers, and it should be chosen according to the actual behavior of the fibers being modeled. In this work we use a phase function that is the sum of a constant and a forward-directed lobe detailed in Section 7.5.

3. The attenuation function A. This function describes the attenuation of light by other fibers on the way into and out of the yarn; it depends on the characteristics of the fibers as well as their microscopic arrangement. In

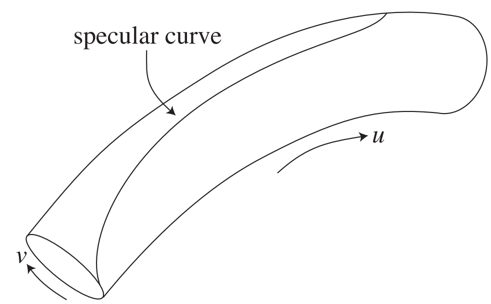

Figure 4.1: A yarn segment with a specular reflection curve.

this work we choose to use Seeliger's law as our attenuation function; this is described in Section 7.6.

Our model has two distinct incarnations: the reflectance model and the texture model. The reflectance model $f_r(\omega_i, \omega_r)$ is used when only the BRDF of the cloth is important (for example, in distant views of a large piece of cloth). The texture model $T(x, y, \omega_i, \omega_r)$, as the name implies, is used when the texture of the cloth is also important. Both models were built on top of the same set of assumptions and have the same average BRDF, which allows seamless switching between the two. (ω_i is incident direction, ω_r is exitant direction, and (x, y) is a point on the surface of the cloth.)

Our reflectance model consists of two functions:

$$f_{r,s}(\omega_i, \omega_r) = \int_{-u_{\max}}^{u_{\max}} G_v f_c A \, du \quad \text{or} \quad f_{r,s}(\omega_i, \omega_r) = \int_0^{2\pi} G_u f_c A \, dv$$

Similarly, our texture model consists of two functions:

$$T(x, y, \omega_i, \omega_r) \propto \chi G_u f_c A \frac{1}{\Delta x} \quad \text{or} \quad T(x, y, \omega_i, \omega_r) \propto \chi G_v f_c A \frac{1}{\Delta y}$$

The function χ equals 1 if the point (x, y) lands in the band of width Δx or Δy centered on the specular curve and 0 otherwise (see Figure 8.1). We shall elaborate on both models in Chapter 8.

Chapter 5

Measurements

We made three types of measurements: reflectance (BRDF) measurements, close-up texture (BTF) measurements, and turntable videos. The BTF measurements were made to understand the behavior of the highlights; in this work we use them primarily for illustrative purposes. The BRDF measurements and turntable videos are used to validate our reflectance and texture model.

The fabrics we measured were:

1. Black cotton fabric in a 3–1 twill weave.
2. Denim, a cotton fabric with blue weft and white warp in a 2–1 twill weave.
3. Red gabardine, a wool fabric in a 2–1 twill weave.
4. Red polyester lining cloth with filament yarns in a very symmetric plain weave.
5. Red charmeuse, a filament silk fabric in a satin weave.
6. Red shantung, a filament silk fabric with red weft yarns and much finer dark gray warp yarns in a plain weave.

The weave patterns of the fabrics we measured can be seen in Figure 5.1. In this work, we follow the convention that the warp yarns run vertically in the figures.

5.1 Reflectance

To measure the BRDFs of our materials, we illuminated them with a light source of small solid angle (a DC regulated fiber-optic illuminator) and measured the

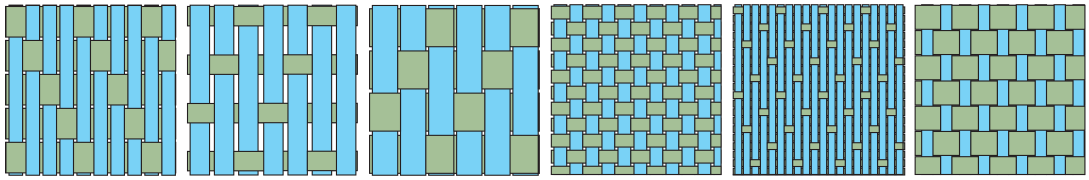

Figure 5.1: Weave patterns of our sample fabrics.

reflected radiance by photographing them with a scientific CCD camera (QImaging Retiga 1300i, with frame-sequential RGB filter). The positions of the source and camera were controlled by a four-axis spherical goniometer (see Figure 5.2). The linearity of the camera and stability of the source have been verified.

From the resulting images we computed the average of a small rectangle positioned at the center of rotation of the camera and source motion. The position in the image and with respect to the source were constant, eliminating the need for flat field calibration of the source or the camera, and the measured area was small enough to avoid significant variation in light source distance or incident angle over the measured area. The values were corrected for the cosine of the incident angle and normalized to a single measurement (per color channel) of a BRDF standard (Spectralon).

We measured datasets consisting of 225 incident directions for each of seven exitant directions. The incident directions are on a grid—generated using a MATLAB implementation of the concentric map described in [38]—covering the hemisphere out to approximately 75 degrees, and the viewing directions coarsely cover the hemisphere (with the assumption of 180° rotational symmetry) out to 60 degrees—in (elevation angle, azimuth angle) pairs: $(0°, 0°)$, $(30°, 0°)$, $(30°, 90°)$, $(60°, 0°)$, $(60°, 45°)$, $(60°, 90°)$, and $(60°, 135°)$.

The BRDF measurements can be seen in Figure 5.3, 5.4, 5.5, 5.6, 5.7, and 5.8.

Figure 5.2: Four-axis spherical goniometer.

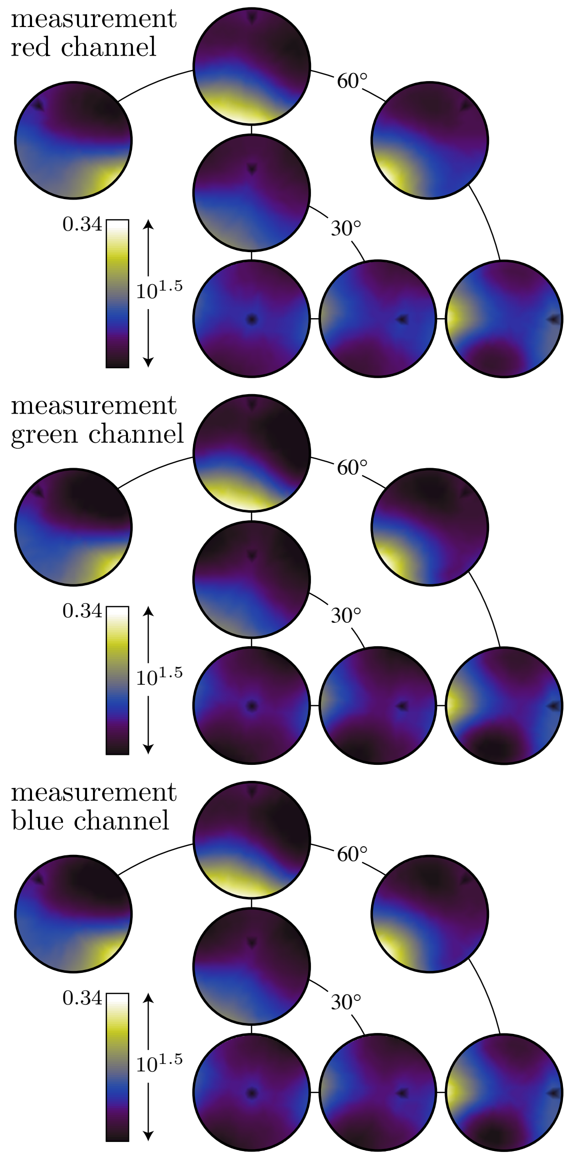

Figure 5.3: BRDF of cotton twill.

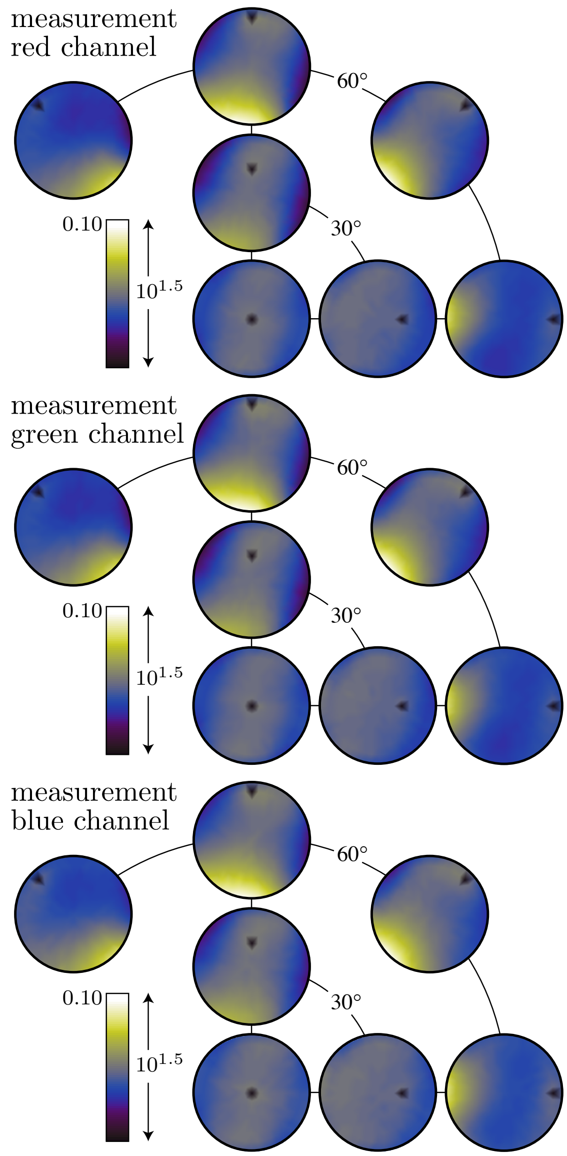

Figure 5.4: BRDF of cotton denim.

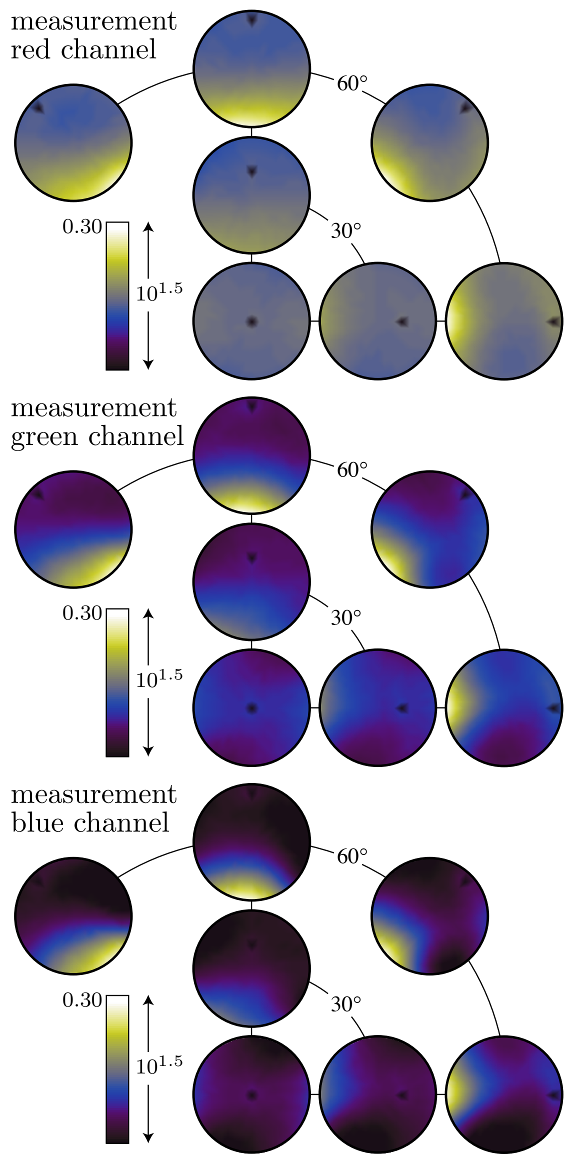

Figure 5.5: BRDF of wool gabardine.

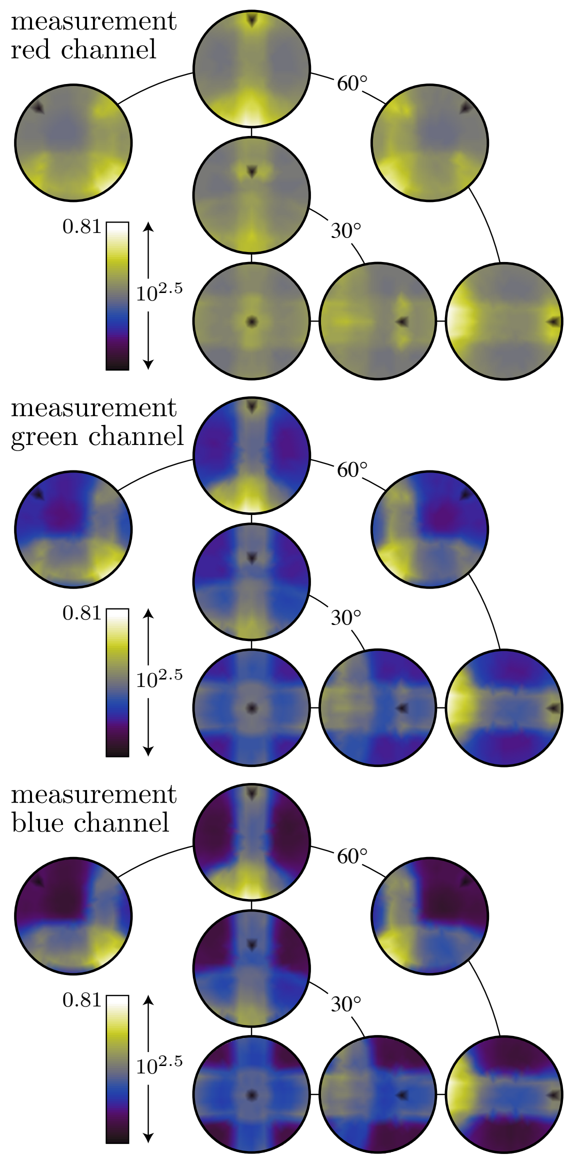

Figure 5.6: BRDF of polyester lining cloth.

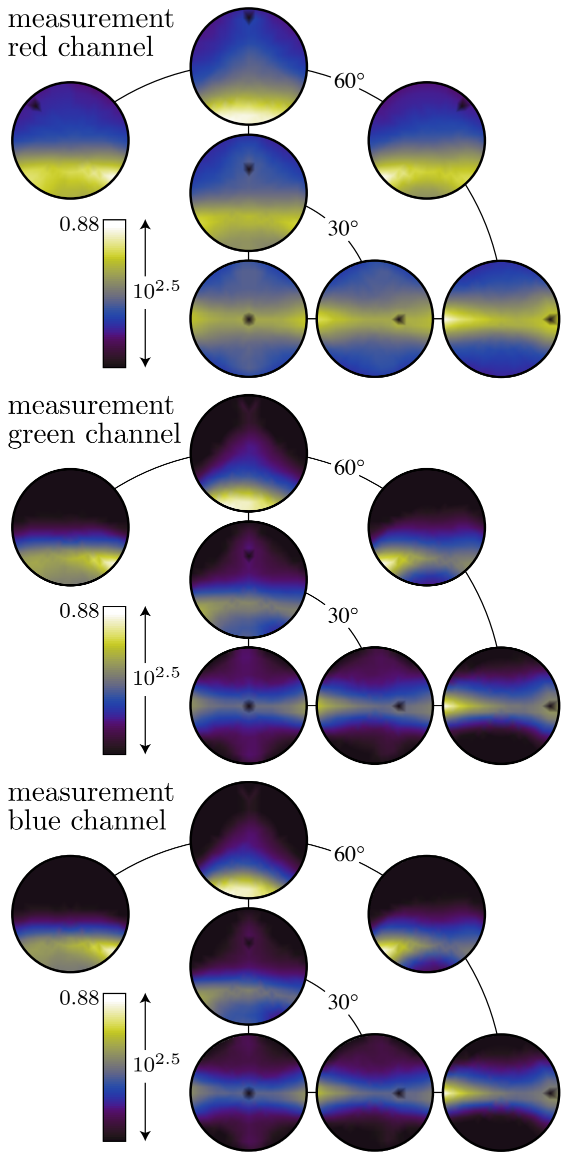

Figure 5.7: BRDF of silk charmeuse.

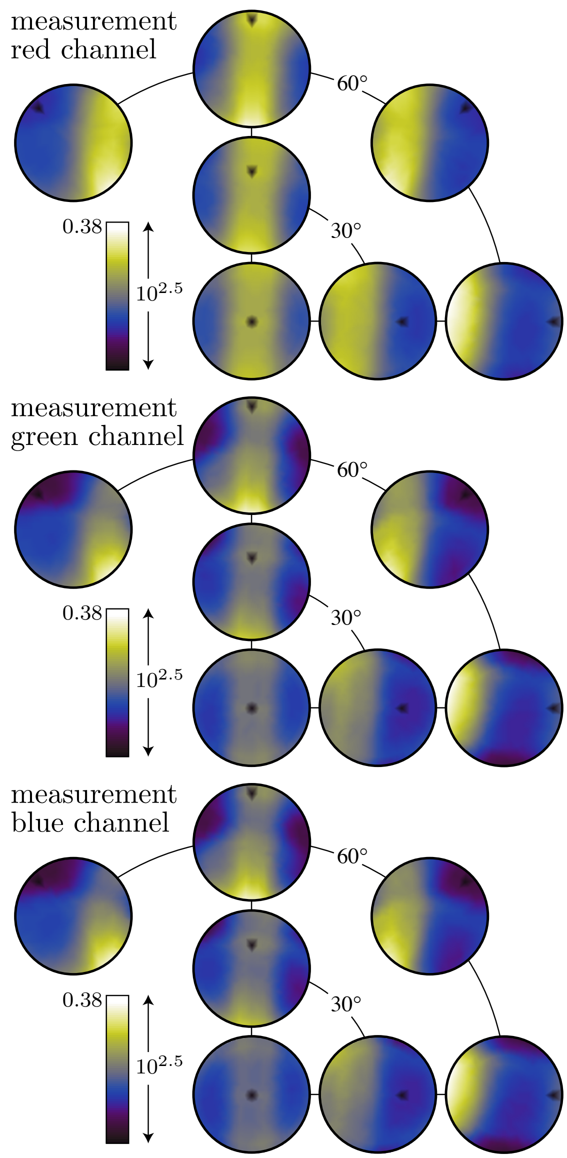

Figure 5.8: BRDF of silk shantung.

Each incident hemisphere is plotted in projection onto the tangent plane, with the warp direction vertical, and the hemispheres are arranged to indicate the exitant direction, which may also be seen by the shadow of the light source in the data. In the plots there is an obvious difference between filament yarns, which produce a pair of fairly classic anisotropic linear highlights (one from the warp yarns and one from the weft), and staple yarns, which produce still quite directional patterns but not distinct linear highlights. The BRDFs of staple fabrics are also asymmetric, even when the view direction is aligned with the warp or weft, because of the twist in the yarns. Also note that only the polyester is well balanced in the contribution of warp and weft; the others are all warp-dominated except shantung, which is heavily weft-dominated.

The plain weave filament fabrics both exhibit bright edges on the specular highlight, which are most noticeable on the polyester but also present on the warp component of shantung. This phenomenon has been explained by Pont and Koenderink [36] as an effect of varying curvature of the yarns, with lower curvature towards the ends of the visible segment, and has also been observed by others [32]. Most of the materials exhibit some retroreflection; and in particular the polyester shows a very sharp retroreflective peak that runs across the highlight (it is most noticeable in the 30° data). We believe that this is a result of interreflections between fibers of circular cross-section, but the phenomenon requires further study.

5.2 Texture

The second set of measurements was made using the same setup but with the camera attached rigidly to the platform on which the cloth rests and equipped with a macro lens at a magnification that enabled the yarns to be clearly discerned.

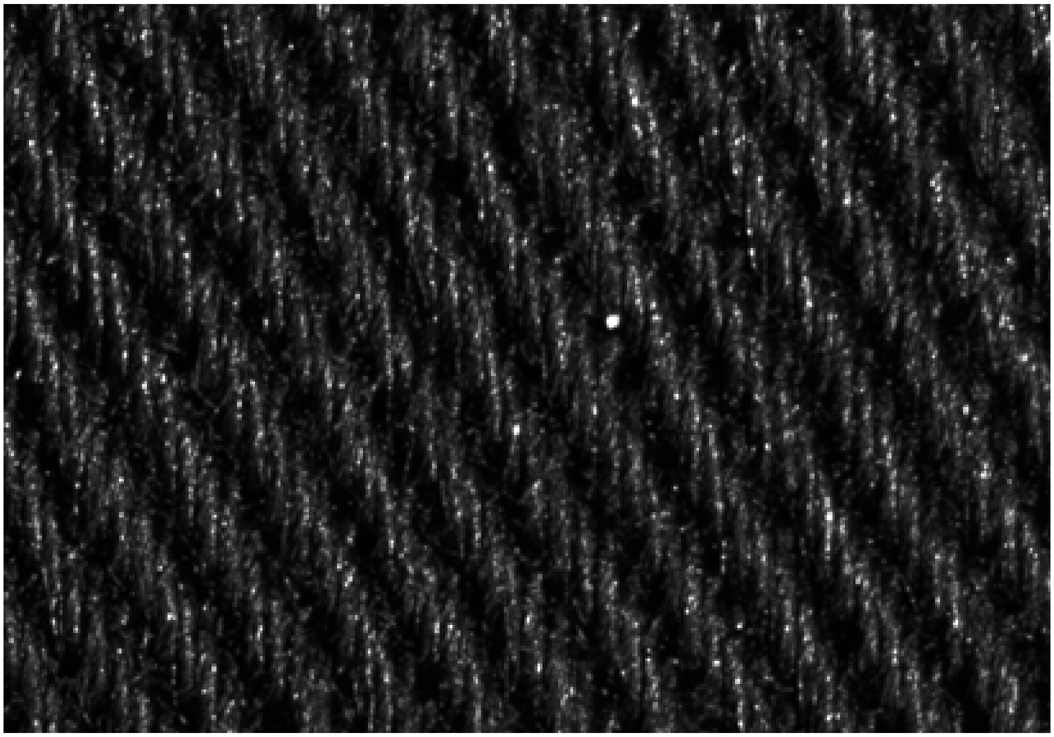

Figure 5.9: Raw texture measurement of black cotton twill.

Figure 5.10: Averaged texture measurement of black cotton twill.

A representative frame from the measurements of a piece of black cotton twill cloth is shown in Figure 5.9. In the photographs, the overall pattern is difficult to discern because of the natural irregularities of the yarns. To remove this random variation and make the systematic pattern more visible, we computed a regularly tiled pattern by averaging all the unit tiles in the measured image. The averaged image of the same piece of black cotton twill cloth under the same condition is shown in Figure 5.10.

Figures 5.11 and 5.12 show the texture of black and white cotton twill under various illumination directions. A particularly interesting feature of this measurement is the similarity of texture between low and high reflectance fabrics. One might expect to see a similar specular component with a much larger diffuse component for white; in fact, the specular peaks in white are between 9 and 25 times brighter than those in black. This suggests that the light contributing to the specular highlights is not simply due to surface reflection (which should be unaffected by dyeing the fibers) but also includes substantial multiple scattering from well-aligned fibers, which, as has been observed in other materials [29], continues to obey specular reflection geometry.

The similarity of these two textures suggests that specular reflection (including specular multiple scattering) is the main contributor to the texture of cloth. This is contrary to the commonly accepted notion that textures on matte-looking fabrics result primarily from diffuse reflection and shadowing–masking.

5.3 Turntable Sequences

To test our model in a more realistic context, we recorded high-resolution video of the same fabrics that were measured for BRDF under controlled conditions that

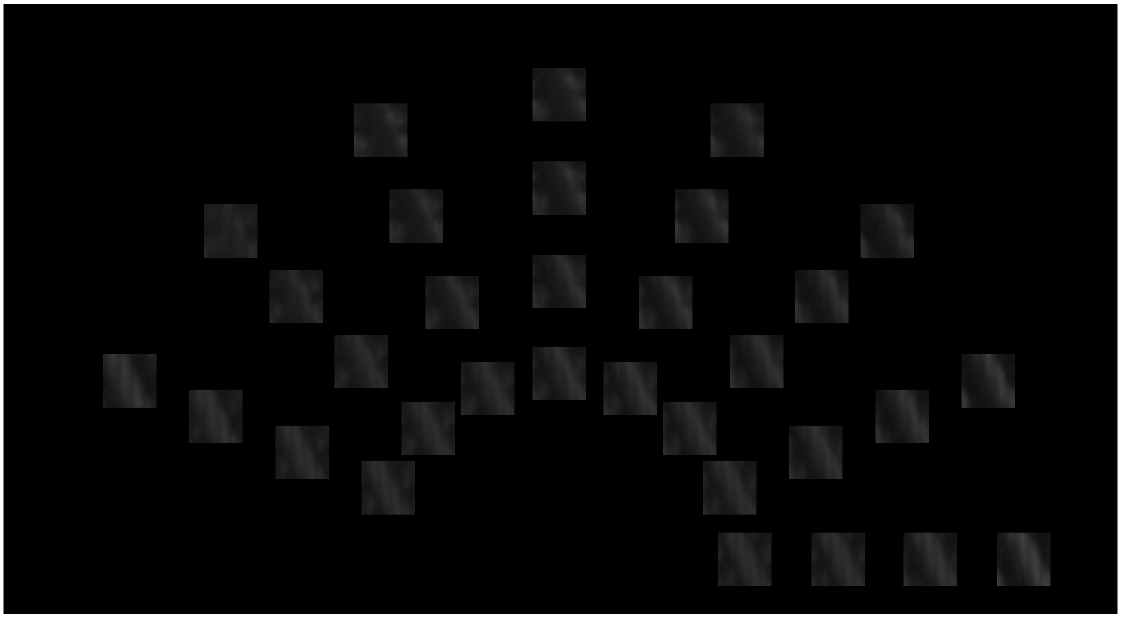

Figure 5.11: Texture of black cotton twill under various illumination directions. The images are arranged in four half-circles, each represents the elevation angle of the illumination direction (30°, 45°, 60°, and 75°).

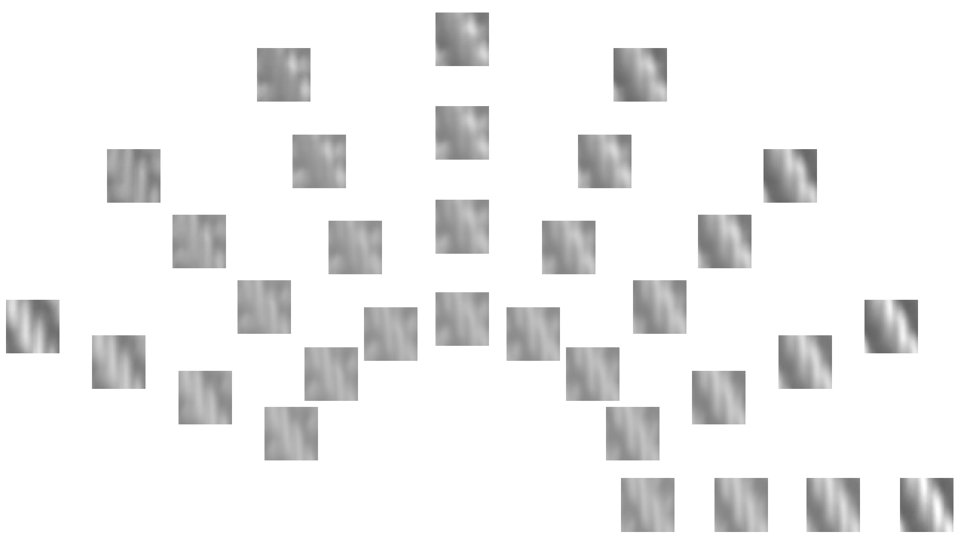

Figure 5.12: Texture of white cotton twill under various illumination directions. The images are arranged as in Figure 5.11.

allowed for comparison to renderings. To isolate the optical behavior from the confounding differences in appearance due to draping characteristics, we built a rigid form by coating draped black canvas with epoxy resin. The fabric samples were draped over the form in turn, ensuring that all the samples were photographed with the same geometry. The form also served to absorb transmitted light, thereby isolating reflection from transmission. We scanned the form with a laser range scanner and fit a surface that was used for rendering the comparisons. The video was captured using stop motion with a high-resolution still camera (Canon EOS 20D). The motion sequence includes a segment where the object rotates with the light and camera stationary, and a sequence where the light moves with the object and camera stationary. The turntable sequences are described in Chapter 9.

Chapter 6

Geometry

A piece of fabric can be thought of as a collection of *segment rectangles*—short visible segments of yarn on the surface of the fabric—arranged in a particular position and orientation relative to one another according to the weave pattern. Each of these segment rectangles represents a yarn segment, which, in turn, is modeled as a curved cylinder made up of fibers spiraling around its axis. Figure 6.1 shows a segment rectangle with its curved cylinder. This chapter describes the geometry of the curved cylinder in detail.

6.1 Assumptions

A yarn is made up of relatively long fibers that may be twisted together. When a staple yarn is straight, we assume that the fibers are aligned with helices spiraling around the yarn axis and that the vectors tangent to fibers near the surface of the yarn all make the same angle with the yarn axis. When the staple yarn is bent into a curved configuration, we assume that it takes on the shape of a tube with curved spine and circular cross section. We assume that the fibers' directions rotate with the cross section, remaining at the same angle to the spine. Since filament yarns are not twisted, the fibers are simply parallel to the yarn axis.

6.2 Geometry of a Yarn Segment

The geometry of a yarn segment (Figure 6.2) is defined in a coordinate system that has z parallel to the overall normal to the fabric surface, y parallel to the relevant

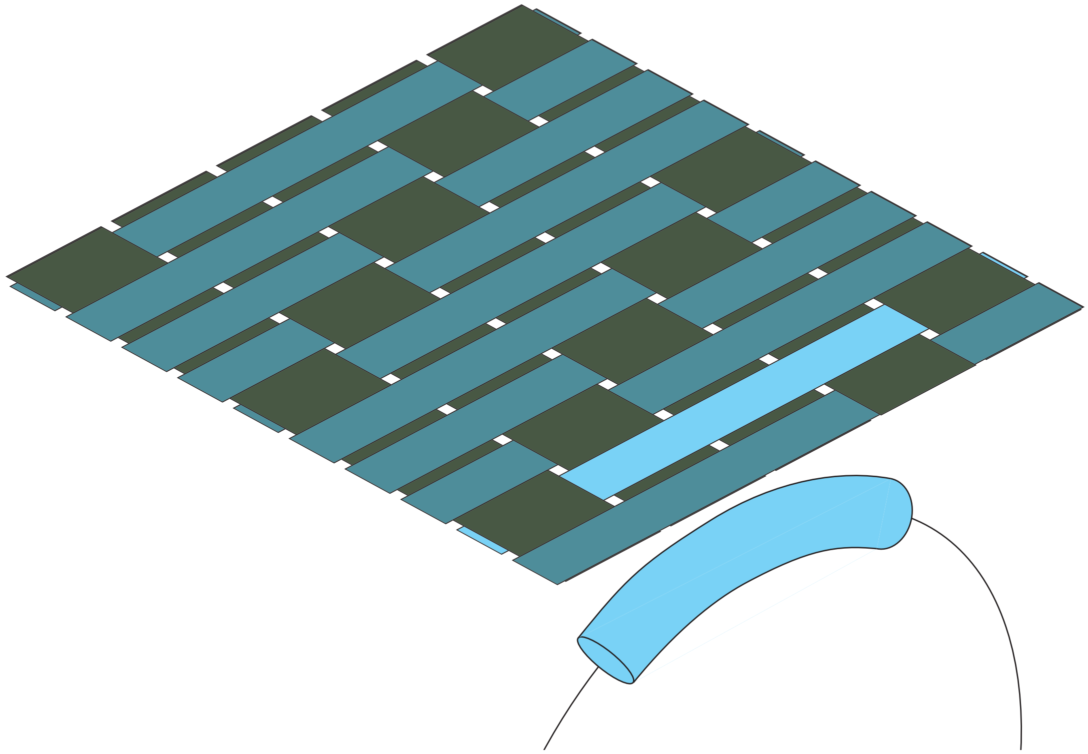

Figure 6.1: A segment rectangle with its curved cylinder.

weaving direction (the warp or weft direction), and x completing the right-handed orthonormal basis.

We model a yarn segment as a curved cylinder: a circular cross section with radius a swept perpendicularly along a spine curve $\mathbf{x}_0(u)$ in the y-z plane from $u = -u_{\max}$ to $u = u_{\max}$; here, $u_{\max}$ is the maximum inclination angle. We will discuss the parameter u a few paragraphs below.

Normally, the spine is a circular arc—resulting in a yarn segment in the shape of a torus segment—though some materials may require a different spine curve. The shape of the spine, however, only enters into the analysis through its curvature, denoted $R(u)$. When the spine is a circular arc, the radius of curvature of the spine is a constant R.

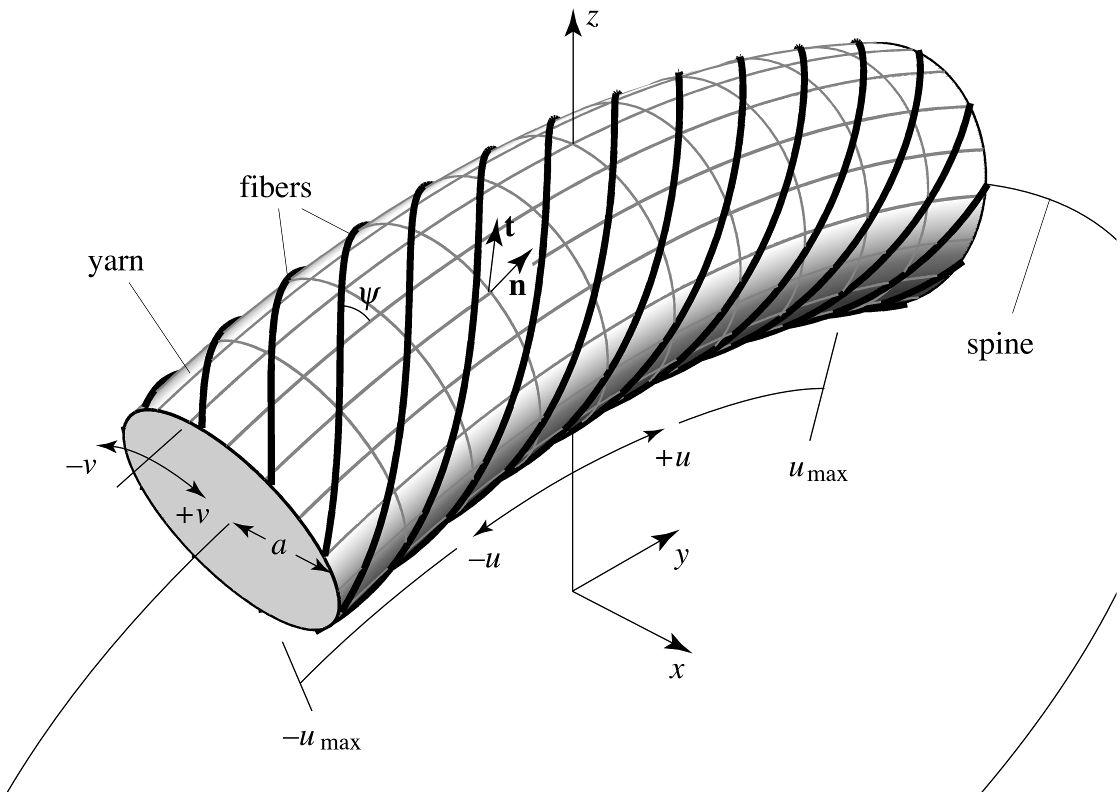

Figure 6.2: A yarn segment modeled as a curved cylinder parameterized by $-u_{\max} \leq u \leq u_{\max}$, $-\pi \leq v \leq \pi$, and $0 < r < a$. Textile fibers form helices around the cylinder with a constant twist angle $-\pi/2 < \psi < \pi/2$.

The yarn is parameterized by three variables: u, v, and r. The variable $-u_{\max} \leq u \leq u_{\max}$ is the angle between the spine's tangent and the y-axis (or, alternatively, between the spine's outward-directed normal and the z-axis). Parameterizing the spine by the angle u of course requires that each tangent angle occur only once. The variables $-\pi \leq v \leq \pi$ and $0 < r < a$ parameterize the circular cross section for each u in polar coordinates.

The normal to the yarn surface $\mathbf{n}$ is a function of u and v:

$$\begin{aligned} \mathbf{n}(u,v) &= R_x(-u)R_y(v)\begin{bmatrix} 0 \\ 0 \\ 1 \end{bmatrix} \\ &= \begin{bmatrix} \sin v \\ \sin u \cos v \\ \cos u \cos v \end{bmatrix} \end{aligned} \tag{6.1}$$

and the parameterization of the segment can be written as follows:

$$\mathbf{x}(u,v,r) = \mathbf{x}_0(u) + r\mathbf{n}(u,v).$$

As explained earlier, we assume that the tangents of the fibers are carried along with the cross section. Like $\mathbf{n}$, they also rotate with v:

$$\begin{aligned} \mathbf{t}(u,v) &= R_x(-u)R_y(v)\begin{bmatrix} -\sin\psi \\ \cos\psi \\ 0 \end{bmatrix} \\ &= \begin{bmatrix} -\cos v \sin\psi \\ \cos u \cos\psi + \sin u \sin v \sin\psi \\ -\sin u \cos\psi + \cos u \sin v \sin\psi \end{bmatrix} \end{aligned} \tag{6.2}$$

where $-\pi/2 < \psi < \pi/2$ is the twist angle of the fibers. At $\psi = 0$ we have a filament yarn, in which $\mathbf{t}(u,v) = (0, \cos u, -\sin u)^T$ is independent of v.

6.2.1 Normal to the yarn surface and fiber tangent on Gauss spheres

We can use Gauss spheres to visualize the various vectors we have in our model.

On a Gauss sphere, for a fixed u, the set of $\mathbf{n}(u, v)$ forms a circle of radius 1 (that is, a great circle) and center $(0, 0, 0)^T$ with normal $(0, \cos u, \sin u)^T$. Figure 6.3 shows half of the circles $(-\pi/2 \leq v \leq \pi/2)$ for several values of u.

On a Gauss sphere, For a fixed v, the set of $\mathbf{n}(u, v)$ forms a circle of radius $\cos v$ and center $(\sin v, 0, 0)^T$ with normal $(1, 0, 0)^T$. Figure 6.4 shows half of the circles $(-\pi/2 \leq u \leq \pi/2)$ for several values of v.

On a Gauss sphere, for a fixed u, the set of $\mathbf{t}(u, v)$ forms a circle of radius $|\sin \psi|$ and center $(0, \cos u \cos \psi, -\sin u \cos \psi)^T$ with normal $(0, \cos u, -\sin u)^T$. Figure 6.5 shows half of the circles $(-\pi/2 \leq v \leq \pi/2)$ for several values of u.

On a Gauss sphere, for a fixed v, the set of $\mathbf{t}(u, v)$ forms a circle of radius $\sqrt{1 - \cos^2 v \sin^2 \psi}$ and center $(-\cos v \sin \psi, 0, 0)^T$ with normal $(-1, 0, 0)^T$. Figure 6.6 shows half of the circles $(-\pi/2 \leq u \leq \pi/2)$ for several values of v.

6.3 Relation Between a Segment Rectangle and Its Curved Cylinder

Recall that we break a piece of fabric into segment rectangles, each of which represents a yarn segment. Also recall that we use a curved cylinder to model the yarn segment. We have examined the geometry of the curved cylinders, but we haven't discussed its relationship with the segment rectangle. This section illustrates the relationship for the simpler case involving circular spines (resulting in toroidal yarn segments). Details of this relationship for the general case involving non-circular

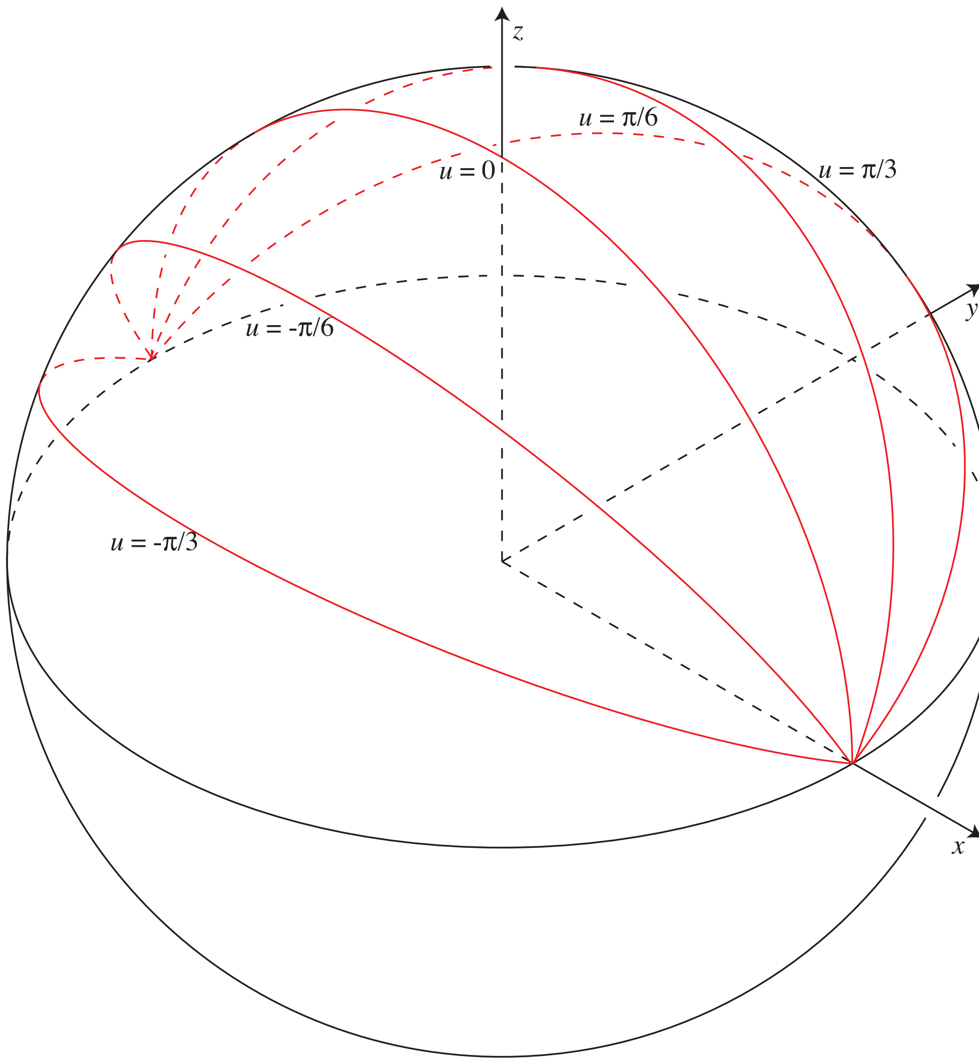

Figure 6.3: Set of normal $\mathbf{n}(u, v)$ for several values of u and $-\pi/2 \leq v \leq \pi/2$.

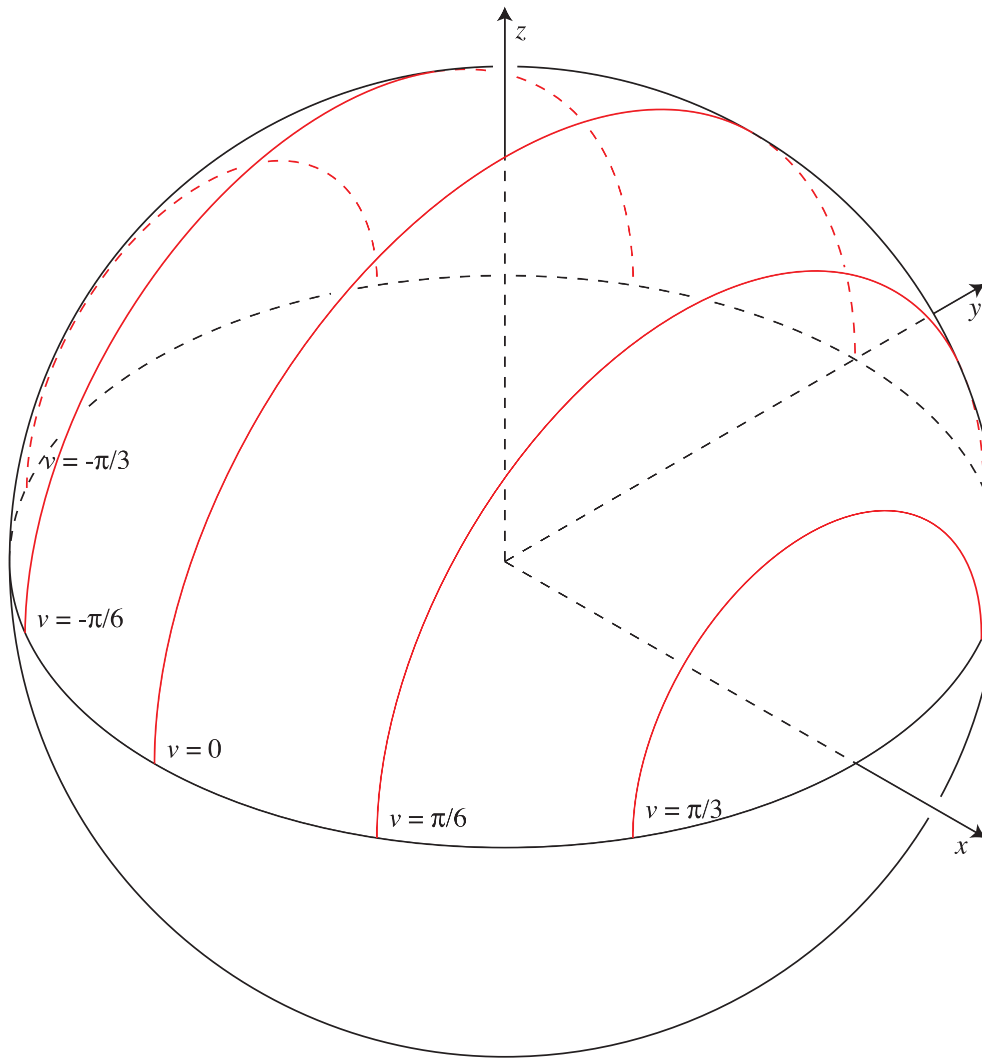

Figure 6.4: Set of normal $\mathbf{n}(u, v)$ for several values of v and $-\pi/2 \le u \le \pi/2$.

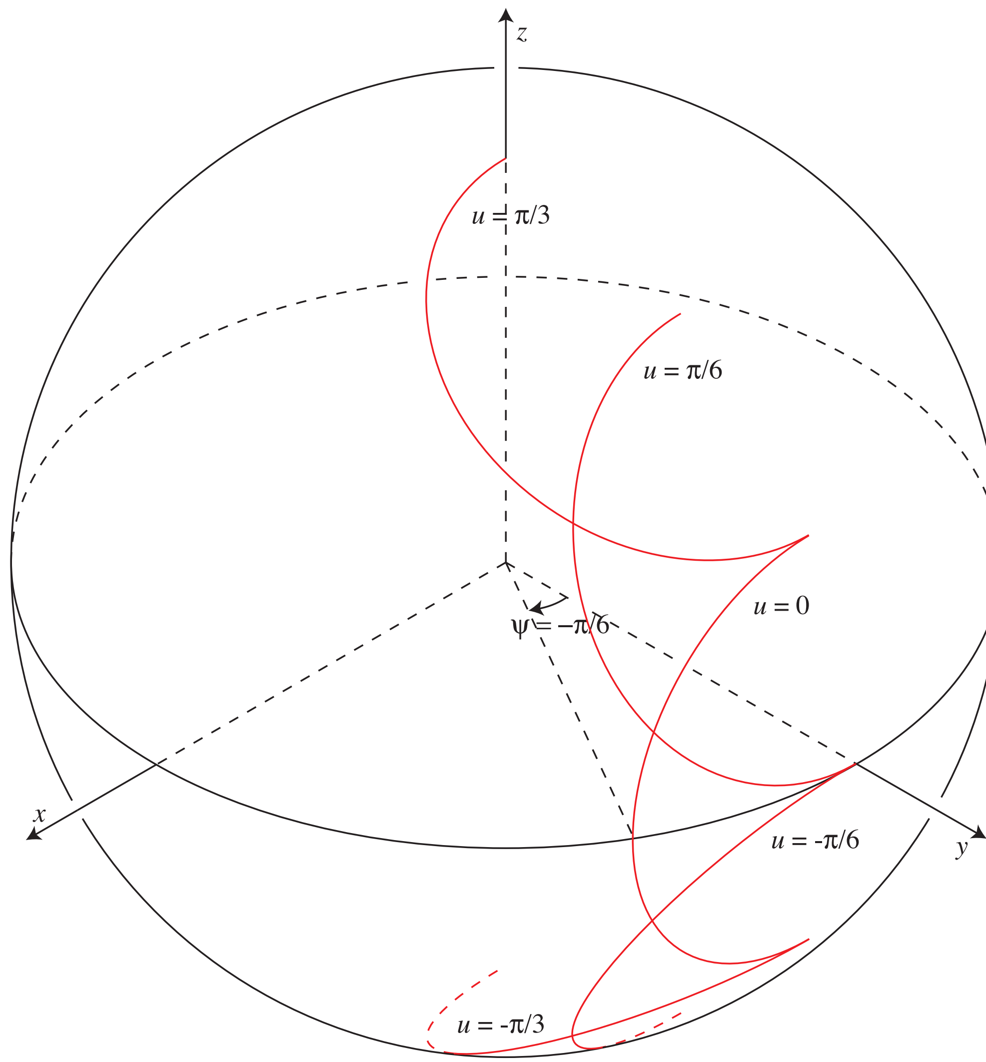

Figure 6.5: Set of tangent $\mathbf{t}(u, v)$ for several values of u and $-\pi/2 \leq v \leq \pi/2$. In this figure, $\psi = -\pi/6$.

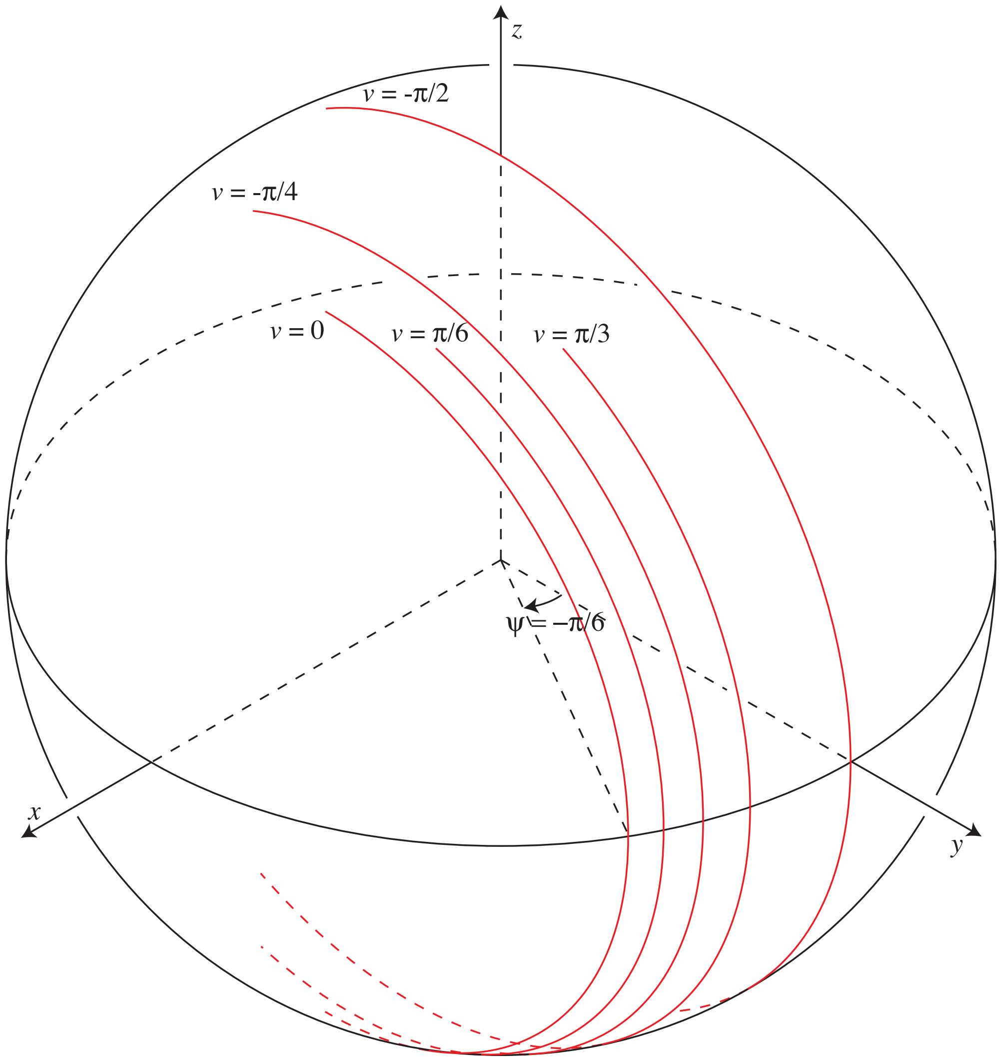

Figure 6.6: Set of tangent $\mathbf{t}(u, v)$ for several values of v and $-\pi/2 \leq u \leq \pi/2$. In this figure, $\psi = -\pi/6$.

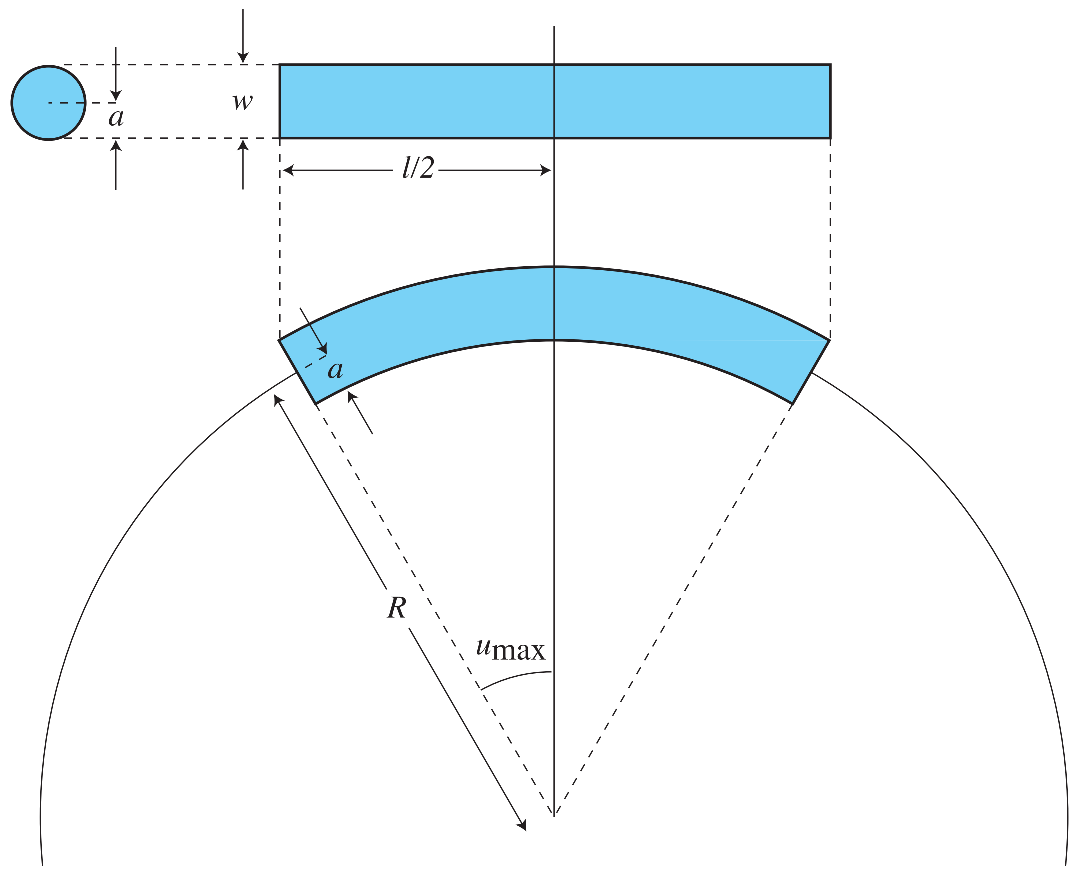

Figure 6.7: Relation between a toroidal yarn segment and the segment rectangle.

spines are discussed in the next section.

Let w and l be the width and length of a segment rectangle. Given the maximum inclination angle $u_{\max}$, our goal is to find R (the radius from the center of the torus hole to the center of the torus tube) and a (the radius of the torus tube). We do this by choosing the largest torus segment whose projection fits in the segment rectangle. Figure 6.7 illustrates this concept.

From the figure, we can see the following relations:

$$a = \frac{w}{2} \tag{6.3}$$

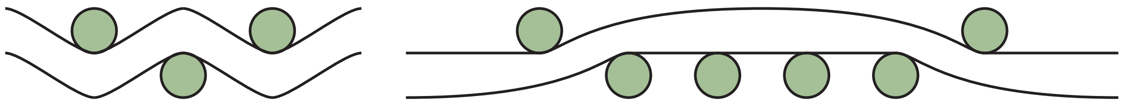

Figure 6.8: Cross section of yarns arranged in plain weave (left) and satin patterns (right).

and

$$R = \frac{0.5l - a \sin u_{\max}}{\sin u_{\max}}. \tag{6.4}$$

Note that this imposes the following constraint: $\frac{w}{2} \sin u_{\max} < \frac{l}{2}$.

6.4 Spine Curves and Radius of Curvature

When the spine of the curved cylinder is a circular arc, the yarn segment is a segment of a torus. In reality, however, the shape of the spine curve depends on the weave pattern and the tension between the yarns of the fabric. Yarn segments in a satin cloth are usually flatter overall and more curved at the ends, while yarn segments in a plain weave cloth are usually more curved at the center. Figure 6.8 shows the cross section of yarns arranged in plain weave and satin patterns. This section describes a way to adjust the curvature of the spine of the curved cylinder to control the shape of the yarn segment.

As in the previous section, the projection of the curved cylinder must fit in the segment rectangle (this implies that $a = \frac{w}{2}$ as shown in Figure 6.7). The spine curve is further constrained such that its tangent direction at the ends is $u_{\max}$. What we want is the ability to control the curvature of the yarn segment between its two ends.

We use conic sections to define the spine of the segment: ellipses for segments

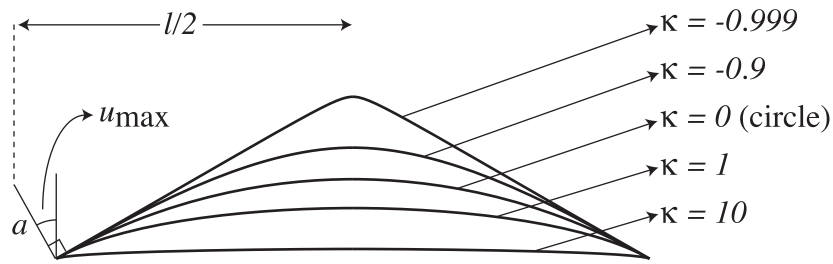

Figure 6.9: Effect of κ on the shape of the spine curve.

that are more curved at the ends, and ellipses, a parabola, or hyperbolas for segments that are less curved at the ends (that is, more curved at the center). The position and orientation of the conic sections are not important since we care only about the radius of curvature of the segment.

Curvature of the segment is controlled by the spine curvature parameter $-1 < \kappa < \infty$. The spine curve is a segment of a circle (and the yarn segment becomes a segment of a torus) for $\kappa = 0$. The more negative κ is, the more curved the segment is at the center. The more positive κ is, the more curved the segment is at the ends. The effect of κ on the shape of the spine curve is shown in Figure 6.9.

Given κ, we compute the axis ratio $\hat{r}$ as follows:

$$\hat{r} = 1 + \kappa(1 + \cot u_{\max}). \tag{6.5}$$

This variable determines whether the spine curve is a hyperbola, a parabola, or an ellipse; $\hat{r} < 0$ specifies a hyperbola, $\hat{r} = 0$ a parabola, and $\hat{r} > 0$ an ellipse ($\hat{r} = 1$ specifies a circle). Additionally, $\hat{r}$ relates the ellipse or hyperbola's semimajor axis $\hat{a}$ and semiminor axis $\hat{b}$ in the following way:

$$\hat{r} = \frac{\hat{b}}{\hat{a}}. \tag{6.6}$$

Given $\hat{a}$ and $\hat{b}$, we can compute the radius of curvature $R(u)$ required in eval-

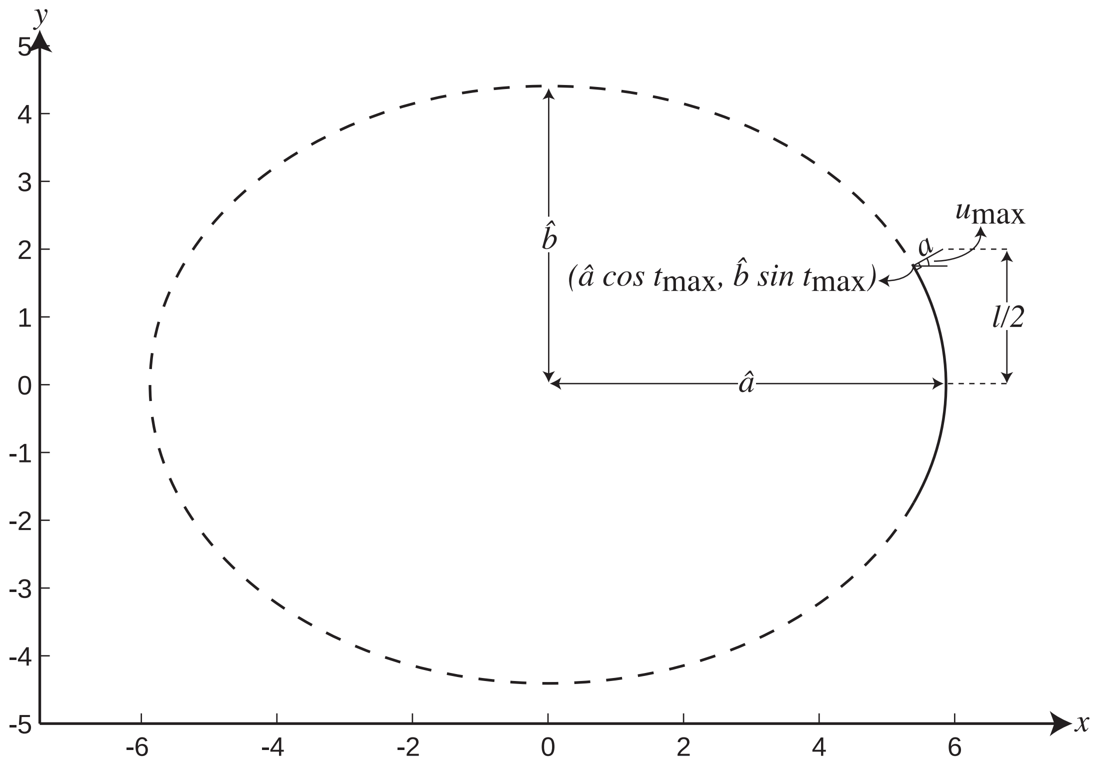

Figure 6.10: Elliptical spine curve (solid line) and the ellipse (dashed line) obtained from $\hat{r} = 0.75$, $u_{\max} = \pi/6$, $w = 1$, and $l = 4$.

uating the scattering model:

$$R(u) = \begin{cases} \frac{(\hat{b}^2 \cos^2 t(u) + \hat{a}^2 \sin^2 t(u))^{1.5}}{\hat{a}\hat{b}} & \text{if } \hat{r} > 0 \\ 2\hat{b}(1 + t(u)^2)^{1.5} & \text{if } \hat{r} = 0 \\ -\frac{(\hat{b}^2 \cosh^2 t(u) + \hat{a}^2 \sinh^2 t(u))^{1.5}}{\hat{a}\hat{b}} & \text{if } \hat{r} < 0 \end{cases} \tag{6.7}$$

where

$$\hat{b} = \begin{cases} \frac{0.5l - a \sin u_{\max}}{\sin t_{\max}} & \text{if } \hat{r} > 0 \\ \frac{0.5l - a \sin u_{\max}}{2t_{\max}} & \text{if } \hat{r} = 0 \\ \frac{0.5l - a \sin u_{\max}}{\sinh t_{\max}} & \text{if } \hat{r} < 0 \end{cases} \tag{6.8}$$

and $\hat{a}$ is computed from $\hat{b}$ and $\hat{r}$.

We will now derive the formulae above.

Elliptical spine curve ($\hat{r} > 0$)

Figure 6.10 shows an ellipse and the spine curve for $\hat{r} = 0.75$, $u_{\max} = \pi/6$, $w = 1$, and $l = 4$. The spine curve is the segment of the ellipse that extends from $-t_{\max}$ to $t_{\max}$. We can observe the following equation from the figure.

$$\hat{b}\sin t_{\max} = \frac{l}{2} - a\sin u_{\max}$$

Therefore, the semiminor axis $\hat{b}$ can be computed as follows.

$$\hat{b} = \frac{0.5l - a\sin u_{\max}}{\sin t_{\max}}$$

where $t_{\max}$ is computed using Equation 2.4.

$$t_{\max} = \arctan(\hat{r}\tan u_{\max})$$

The semimajor axis $\hat{a}$ can be computed using Equation 6.6.

$$\hat{a} = \frac{\hat{b}}{\hat{r}}$$

The radius of curvature $R(u)$ can then be computed using Equation 2.4 and Equation 2.5.

$$R(u) = \frac{(\hat{b}^2\cos^2 t(u) + \hat{a}^2\sin^2 t(u))^{1.5}}{\hat{a}\hat{b}}$$

For the special case $\hat{r} = 1$, we have a circle with radius

$$R = \frac{0.5l - a\sin u_{\max}}{\sin u_{\max}}$$

Notice that we arrive at the same formula found in Equation 6.4.

Parabolic spine curve ($\hat{r} = 0$)

Figure 6.11 shows a parabola and the spine curve for $\hat{r} = 0$, $u_{\max} = \pi/6$, $w = 1$, and $l = 4$. The spine curve is the segment of the parabola that extends from $-t_{\max}$

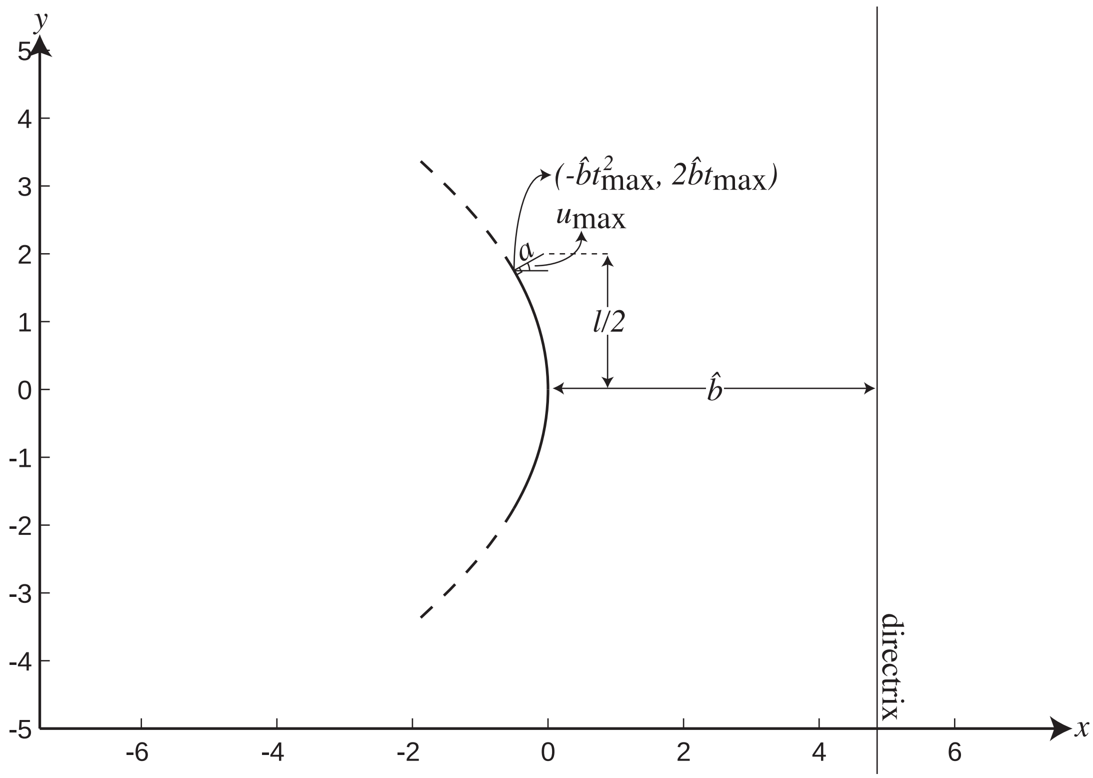

Figure 6.11: Parabolic spine curve (solid line) and the parabola (dashed line) obtained from $\hat{r} = 0$, $u_{\max} = \pi/6$, $w = 1$, and $l = 4$.

to $t_{\max}$. We can observe the following equation from the figure.

$$2\hat{b}t_{\max} = \frac{l}{2} - a \sin u_{\max}$$

Therefore, $\hat{b}$ can be computed as follows.

$$\hat{b} = \frac{0.5l - a \sin u_{\max}}{2t_{\max}}$$

where $t_{\max}$ is computed using Equation 2.7.

$$t_{\max} = \tan u_{\max}$$

The radius of curvature $R(u)$ can then be computed using Equation 2.7 and Equation 2.8.

$$R(u) = 2\hat{b}(1 + t(u)^2)^{1.5}$$

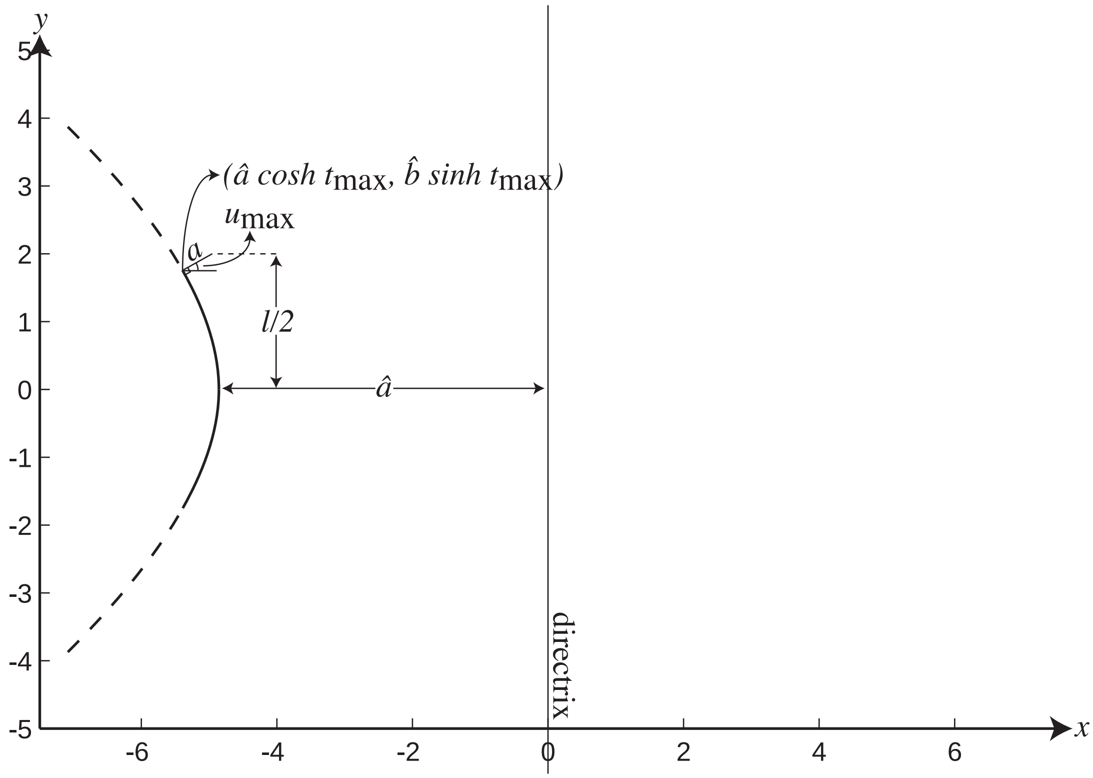

Figure 6.12: Hyperbolic spine curve (solid line) and the hyperbola (dashed line) obtained from $\hat{r} = -0.75$, $u_{\max} = \pi/6$, $w = 1$, and $l = 4$.

Hyperbolic spine curve ($\hat{r} < 0$)

Figure 6.12 shows a hyperbola and the spine curve for $\hat{r} = -0.75$, $u_{\max} = \pi/6$, $w = 1$, and $l = 4$. The spine curve is the segment of the hyperbola that extends from $-t_{\max}$ to $t_{\max}$. We can observe the following equation from the figure.

$$\hat{b} \sinh t_{\max} = \frac{l}{2} - a \sin u_{\max}$$

Therefore, the semiminor axis $\hat{b}$ can be computed as follows.

$$\hat{b} = \frac{0.5l - a \sin u_{\max}}{\sinh t_{\max}}$$

where $t_{\max}$ is computed using Equation 2.10.

$$t_{\max} = -\tanh^{-1}(\hat{r} \tan u_{\max})$$

The semimajor axis $\hat{a}$ can be computed using Equation 6.6.

$$\hat{a} = \frac{\hat{b}}{\hat{r}}$$

The radius of curvature $R(u)$ can then be computed using Equation 2.10 and Equation 2.11.

$$R(u) = -\frac{(\hat{b}^2 \cosh^2 t(u) + \hat{a}^2 \sinh^2 t(u))^{1.5}}{\hat{a}\hat{b}}$$

Chapter 7

Reflection

Recall from the previous chapter that we think of a piece of fabric as a collection of yarn segments, each modeled as a curved cylinder made up of fibers spiraling around its axis. Light that strikes these fibers reflects specularly into a cone centered on the local fiber axis (Figure 7.2). Different fibers reflect light that comes from the same direction into different cones, and by summing over all the fibers we can describe the scattering due to an entire yarn segment. The light scattered from the whole fabric is then simply a weighted sum of the light scattered by the different segments, together with a diffuse component.

By summing their contributions in this way, interactions between segments, including masking, shadowing, and inter-reflection, are disregarded. The model nonetheless succeeds in capturing the most important visual features of the fabrics we have studied, which suggests that the local reflection geometry is the most important factor in the appearance of woven cloth.

In this chapter, we describe light scattering from a yarn segment, derive the scattering function, and explain the various components of the function. While this material is important to the development of our model, readers interested only in the model itself may prefer to skip this chapter and go to Chapter 8 instead.

7.1 Assumptions

Our reflection model for fabric is based on some simple assumptions about the scattering behavior of the yarns that it is made from.

Since the fibers in a yarn are not tightly packed, the yarn must be treated as a volumetric medium, rather than as a reflecting surface. We do assume, however, that all important scattering happens close enough to the surface that their direction is the same as for fibers on the surface.

Because most textile fibers are fairly specular and locally well aligned, we assume that local reflection from the fibers is ideally specular: all light from a single incident direction is reflected into the cone that has the same inclination to the fiber tangent. Of course imperfections in the fibers and random variations in fiber orientation mean the highlight will not be perfectly sharp, but other aspects of the geometry serve to blur the highlight into a smooth distribution, and as long as that blur is large compared to the width of the actual distribution it is safe to use the ideal specular model. This assumption is important because it restricts significant contributions to the scattering integral to happen only under certain geometric conditions, significantly simplifying the model.

A second simplification about local reflection is that all scattering that happens outside of a local area of well-aligned fibers is diffuse. This means that all directional effects are treated as single scattering.

7.2 Scattering from a Yarn Segment

The goal of this section is to compute the scattering function of a yarn segment, in isolation from the rest of the cloth. The scattering function, $f_s(\omega_i, \omega_r)$, describes the contribution of incident irradiance arriving from the direction ω_i to scattered intensity exiting in the direction ω_r. The total scattered intensity is the integral of the scattering function over incident light from the entire sphere (denoted by "4π" below):

$$I_r(\omega_r) = \int_{4\pi} f_s(\omega_i, \omega_r) L_i(\omega_i) \, d\omega_i$$

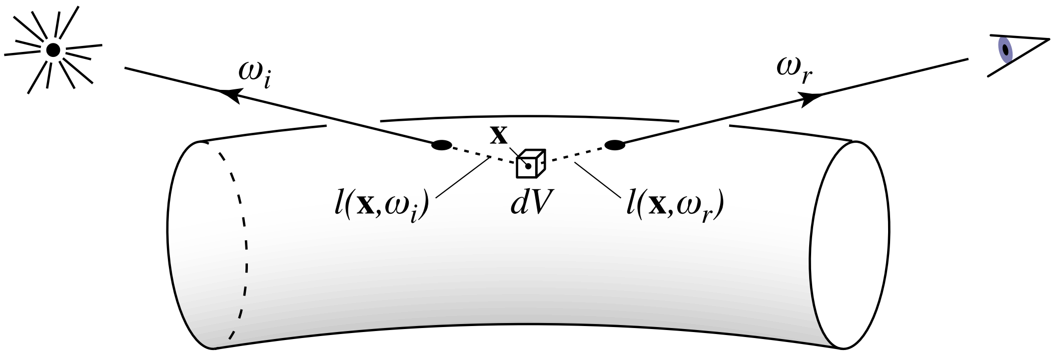

Figure 7.1: Scattering from a volume in a yarn segment.

In Subsection 7.2.1 we express I_r as a volume integral over the yarn segment, then in Subsection 7.2.2 we specialize to the case of specularly reflecting fibers. This establishes the general formula for the scattering function. In later sections we discuss the details of each of the terms in the scattering function.

7.2.1 Scattering integral for a yarn segment

Under the assumption that a yarn acts like a single-scattering medium, we can compute the contribution of a volume element $dV(\mathbf{x})$ to the intensity scattered in direction ω_r by integrating over the incident radiance distribution $L_i(\omega_i)$:

$$\frac{dI_r(\omega_r)}{dV} = \int_{4\pi} \sigma_s f_p(\omega_i, \mathbf{t}(\mathbf{x}), \omega_r) e^{-\sigma_t l(\mathbf{x},\omega_i)} e^{-\sigma_t l(\mathbf{x},\omega_r)} L_i(\omega_i)\, d\omega_i$$

where σ_s and σ_t are the volume scattering and attenuation coefficients, f_p is the phase function, and $l(\mathbf{x}, \mathbf{v})$ is the distance from the point $\mathbf{x}$ to the outside of the volume in the direction $\mathbf{v}$ (Figure 7.1). To obtain the total scattered intensity for a segment of yarn viewed at a distance from direction ω_r, we simply integrate this expression over the segment's volume:

$$I_r = \int \int_{4\pi} \sigma_s f_p(\omega_i, \mathbf{t}(\mathbf{x}), \omega_r) e^{-\sigma_t (l(\mathbf{x},\omega_i) + l(\mathbf{x},\omega_r))} L_i(\omega_i)\, d\omega_i\, dV(\mathbf{x}).$$

For a segment parameterized as described in Section 6.2, we have:

$$dV = dr \cdot r dv \cdot (R(u) + r\cos v)du$$

Therefore, we have:

$$\int_{-u_{\max}}^{u_{\max}} \int_0^{2\pi} \int_0^a \int_{4\pi} \sigma_s f_p(\omega_i, \mathbf{t}(\mathbf{x}), \omega_r) \\ e^{-\sigma_t(l(\mathbf{x},\omega_i)+l(\mathbf{x},\omega_r))} L_i(\omega_i)\, d\omega_i\, r(R(u) + r\cos v)\, dr\, dv\, du.$$

where $R(u)$ is the radius of curvature of the spine. With the assumption that scattering happens near the surface, $\mathbf{t}$ doesn't depend on r, and we can replace the volume element $r(R(u) + r\cos v)$ with its value at $r = a$, leaving the attenuation $e^{-\sigma_t(l(\mathbf{x},\omega_i)+l(\mathbf{x},\omega_r))}$ as the only quantity depending on r. Let A, called the attenuation function, be defined as follows:

$$A(\omega_i, u, v, \omega_r) = \int_0^a \sigma_s e^{-\sigma_t(l(u,v,r,\omega_i)+l(u,v,r,\omega_r))} dr.$$

Using this notation we arrive at

$$I_r(\omega_r) = \int_{-u_{\max}}^{u_{\max}} \int_0^{2\pi} \int_{4\pi} f_p(\omega_i, \mathbf{t}(u,v), \omega_r) L_i(\omega_i) A(\omega_i, u, v, \omega_r) \\ d\omega_i\;\; a(R(u) + a\cos v)\, dv\, du. \quad (7.1)$$

This equation can be used to define a scattering function that works for any phase function but requires a double integral over u and v to compute its value. Instead, we chose to make the assumption of ideal specular fibers, which allows us to remove one more integral, as explained in the next subsection.

7.2.2 Scattering from specular fibers

We have stated the assumption that local scattering from the fibers is ideally specular, as illustrated in Figure 7.2. This makes this integral simpler than over

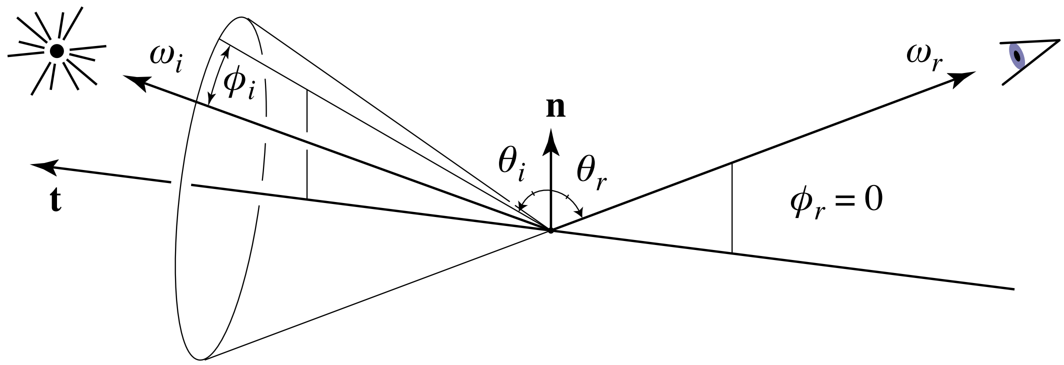

Figure 7.2: Geometry of specular reflection from a fiber. Reflected light depends only on incident light within the specular cone.

the whole sphere because only light on the specular cone can contribute to the overall scattering. To write this integral we introduce a spherical coordinate system aligned with $\mathbf{t}$, where $\omega_i = (\theta_i, \phi_i)$ and $\omega_r = (\theta_r, \phi_r)$. As seen in the figure, $\sin\theta_i = \omega_i \cdot \mathbf{t}$ and $\phi_i = 0$ when ω_i is coplanar with $\mathbf{t}$ and $\mathbf{n}$. Similarly, $\sin\theta_r = \omega_r \cdot \mathbf{t}$ and $\phi_r = 0$ when ω_r is coplanar with $\mathbf{t}$ and $\mathbf{n}$. We denote the difference $\phi_r - \phi_i$ as ϕ. Ideal specular reflection occurs exactly when $\mathbf{h} \cdot \mathbf{t} = 0$, where $\mathbf{h}$ is the *half vector*, the bisector of the directions ω_i and ω_r. In this coordinate system, light is only reflected from ω_i to ω_r when $\theta_i = -\theta_r$, as can be seen from Figure 7.2. This assumption about the phase function f_p can be expressed mathematically as a statement about the local scattering integral:

$$\int_{4\pi} f_p(\omega_i, \mathbf{t}, \omega_r) L_i(\omega_i)\, d\omega_i = \int_0^{2\pi} f_c(\theta_r, \phi) L_i(-\theta_r, \phi_i)\, d\phi$$

That is, the radiance scattered locally from the fibers is an integral of the incident radiance only over the specular cone; the rest of the incident sphere does not contribute. The function f_c is the “circular phase function,” which describes how scattered light is distributed over the specular cone. (If we were to write an expression for f_p it would involve the product of f_c with a delta function in terms of θ.) We are assuming for simplicity that f_c depends on $\phi = \phi_r - \phi_i$ rather than on ϕ_i and ϕ_r separately.

Substituting this lower-dimensional scattering integral back into Equation 7.1 we obtain

$$I_r(\omega_r) = \int_{-u_{\max}}^{u_{\max}} \int_0^{2\pi} \int_0^{2\pi} f_c(\theta_r, \phi) L_i(-\theta_r, \phi_i) A(\omega_i, v, \omega_r)\, d\phi \\ a(R(u) + a\cos v)\, dv\, du.$$

The 4D integral in Equation 7.1 has become a 3D integral, expressed as an integral over a 1D range of incoming directions for each point on the 2D surface of the yarn segment—that is, for a given surface point, only a one-dimensional subset of the incident sphere contributes. But it can also be interpreted as an integral along a 1D path across the surface for each point in a 2D range of incoming directions—that is, for a given incoming direction, only a one-dimensional subset of the surface contributes. In each case, the contributing points are exactly those for which $\mathbf{h} \cdot \mathbf{t} = 0$. This integral is in the coordinates (u, v, ϕ), but these variables can be computed from ω_i and u or from ω_i and v. If we reparameterize this integral by (ω_i, u) or by (ω_i, v), we can move the integral over ω_i to the outside, then extract a scattering function from the equation.

To reparameterize the integral with u on the outside, we need to express (ϕ, v) as a function of (ω_i, u) and find the Jacobian $|\partial(\phi, v)/\partial\omega_i|$. The integral then becomes:

$$I_r(\omega_r) = \int_{-u_{\max}}^{u_{\max}} \int_{4\pi} \sum_k f_c\, L_i\, A \left| \frac{\partial(\phi, v)_k}{\partial\omega_i} \right| a(R(u) + a\cos v_k)\, d\omega_i\, du$$

There will be zero, one, or two (ϕ, v) that satisfy $\mathbf{h} \cdot \mathbf{t} = 0$ for a given u and ω_i and, in general, we need to sum over the different solutions, which we call (ϕ_k, v_k).

However, the particular attenuation function A we use has the implication that at most one has a nonzero contribution.

To simplify, we introduce the *geometry factor*:

$$G_v(\omega_i, u, \omega_r) = \left| \frac{\partial(\phi, v)_k}{\partial \omega_i} \right| a(R(u) + a \cos v_k)$$

and rearrange the equation into the form of a scattering integral:

$$I_r(\omega_r) = \int_{4\pi} \left[\int_{-u_{\max}}^{u_{\max}} \sum_k G_v f_c(\theta_r, \phi_k) A(\omega_i, u, v_k, \omega_r)\, du \right] L_i(\omega_i)\, d\omega_i$$

from which we can read off the scattering function:

$$f_s(\omega_i, \omega_r) = \int_{-u_{\max}}^{u_{\max}} \sum_k G_v f_c(\theta_r, \phi_k) A(\omega_i, u, v_k, \omega_r)\, du. \tag{7.2}$$

Similarly, if we reparameterize with v on the outside we have:

$$f_s(\omega_i, \omega_r) = \int_0^{2\pi} \sum_k G_u f_c(\theta_r, \phi_k) A(\omega_i, u_k, v, \omega_r)\, dv. \tag{7.3}$$

where G_u is defined analogously to G_v.

These two integrals are equivalent except where the reparameterization fails. In particular, we cannot use u as the parameter for filament yarns (with $\psi = 0$) because $\mathbf{t}$ does not depend on v and therefore v cannot be written as a function of ω_i and u. We integrate over u for staple yarns and over v for the filament case.

7.3 Finding Ideal Specular Reflection

In order to compute the integral in the previous subsection, we need to be able to express v as a function of u and vice versa. Geometrically, we want to find the value of v at which the ideal specular reflection takes place given a value of u and vice versa.

Recall that ideal specular reflection occurs exactly when $\mathbf{h} \cdot \mathbf{t} = 0$, where $\mathbf{h}$ is the half vector. This means that, for given incoming and exitant directions, only a one-dimensional subset of the surface of the yarn segment contributes to the specular reflection. Since the surface of the yarn segment is parameterized using u and v, we can write v as a function of u, incoming direction ω_i, and exitant direction ω_r. Similarly, we can express u as a function of v, ω_i, and ω_r.

Solving the equality $\mathbf{h} \cdot \mathbf{t} = 0$ for v given u, ω_i, and ω_r results in the following equation.

$$\begin{aligned}
\mathbf{h} \cdot \mathbf{t} &= 0 \\
\mathbf{h}_x \cos v - (\mathbf{h}_y \sin u + \mathbf{h}_z \cos u) \sin v &= (\mathbf{h}_y \cos u - \mathbf{h}_z \sin u) \cot \psi \\
\cos(v - \arctan(-\mathbf{h}_y \sin u - \mathbf{h}_z \cos u, \mathbf{h}_x)) &= \tfrac{\mathbf{h}_y \cos u - \mathbf{h}_z \sin u}{\sqrt{\mathbf{h}_x^2 + (\mathbf{h}_y \sin u + \mathbf{h}_z \cos u)^2}} \cot \psi \\
v(\omega_i, u, \omega_r) &= \arctan(-\mathbf{h}_y \sin u - \mathbf{h}_z \cos u, \mathbf{h}_x) \\
&\quad \pm \arccos(D)
\end{aligned} \tag{7.4}$$

where

$$D = \frac{\mathbf{h}_y \cos u - \mathbf{h}_z \sin u}{\sqrt{\mathbf{h}_x^2 + (\mathbf{h}_y \sin u + \mathbf{h}_z \cos u)^2}} \cot \psi$$

If $|D| > 1$, no fiber tangent reflects light from ω_i to ω_r.

While not required in the analysis of ideal specular reflection, we will show that at most one of the two reflections satisfies $\mathbf{h} \cdot \mathbf{n} > 0$.

$$\begin{aligned}
\mathbf{h} \cdot \mathbf{n} &= 0 \\
(\mathbf{h}_y \sin u + \mathbf{h}_z \cos u) \cos v + \mathbf{h}_x \sin v &= 0 \\
\cos(v - \arctan(\mathbf{h}_x, \mathbf{h}_y \sin u + \mathbf{h}_z \cos u)) &= 0 \\
v &= v_0 \pm \tfrac{\pi}{2}
\end{aligned}$$

where

$$v_0 = \arctan(\mathbf{h}_x, \mathbf{h}_y \sin u + \mathbf{h}_z \cos u)$$

Therefore a reflection $v(\omega_i, u, \omega_r)$ satisfies $\mathbf{h} \cdot \mathbf{n} > 0$ if and only if $v_0 - \frac{\pi}{2} < v(\omega_i, u, \omega_r) < v_0 + \frac{\pi}{2}$.

We can further the derivation of Equation 7.4 as follows.

$$\begin{aligned} v(\omega_i, u, \omega_r) &= \arctan(-\mathbf{h}_y \sin u - \mathbf{h}_z \cos u, \mathbf{h}_x) \pm \arccos(D) \\ &= v_0 - \tfrac{\pi}{2} \pm \arccos(D) \end{aligned}$$

Since $0 \leq \arccos(D) \leq \pi$, $v_0 - \frac{\pi}{2} \leq v_0 - \frac{\pi}{2} + \arccos(D) \leq v_0 + \frac{\pi}{2}$, while $v_0 - \frac{\pi}{2} - \arccos(D) < v_0 - \frac{\pi}{2}$. Therefore, at most only one of the two reflections satisfies $\mathbf{h} \cdot \mathbf{n} > 0$.

For the filament case ($\psi = 0$), we have the following equation.

$$\begin{aligned} \mathbf{h} \cdot \mathbf{t} &= 0 \\ \mathbf{h}_y \cos u - \mathbf{h}_z \sin u &= 0 \\ \cos(u - \arctan(-\mathbf{h}_z, \mathbf{h}_y)) &= 0 \\ u(\omega_i, v, \omega_r) &= \arctan(-\mathbf{h}_z, \mathbf{h}_y) \pm \tfrac{\pi}{2} \end{aligned} \tag{7.5}$$

Since $-1 < \mathbf{h}_y < 1$ and $0 < \mathbf{h}_z \leq 1$, we know that $-\pi < \arctan(-\mathbf{h}_z, \mathbf{h}_y) < 0$ and, therefore, $-\frac{\pi}{2} < \arctan(-\mathbf{h}_z, \mathbf{h}_y) + \frac{\pi}{2} = \arctan(\mathbf{h}_y/\mathbf{h}_z) < \frac{\pi}{2}$. The other reflection occurs π radians away at the back of the yarn.

7.3.1 Ideal specular reflection on Gauss spheres

We can visualize the ideal specular reflection using Gauss spheres in the following way.

Recall that the set of fiber tangents can be visualized as a circle on a Gauss sphere (Figure 6.5 or 6.6). Since ideal specular reflection occurs when $\mathbf{h} \cdot \mathbf{t} = 0$, $\mathbf{h}$ must be perpendicular to $\mathbf{t}$. We can draw a great circle that contains all vectors that are perpendicular to $\mathbf{h}$. Ideal specular reflection occurs at the intersection of this great circle with the circle that contains the set of fiber tangents.

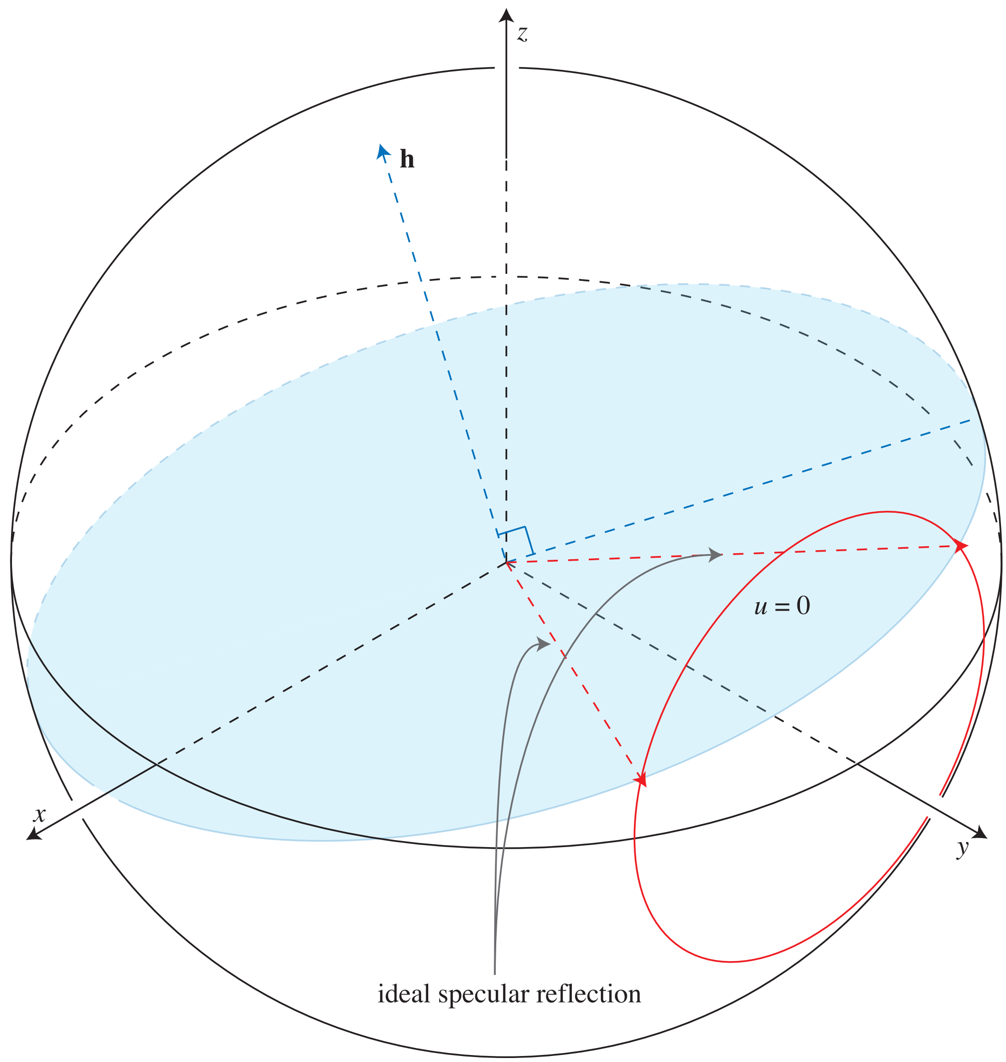

Figure 7.3: Ideal specular reflection $v(\omega_i, u, \omega_r)$ for staple (in this case, $\psi = -\pi/6$) given a particular $\mathbf{h} = (\omega_i + \omega_r)/|\omega_i + \omega_r|$ and $u = 0$.

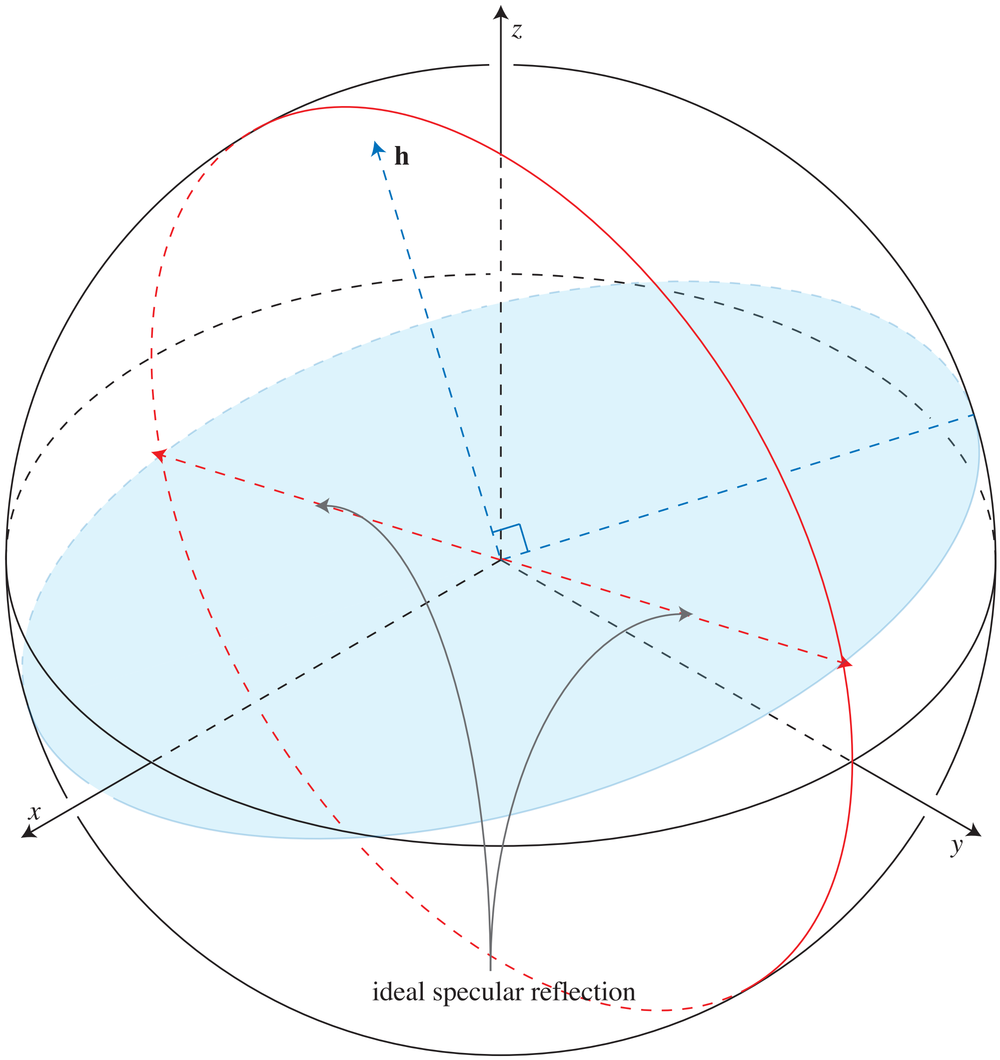

Figure 7.4: Ideal specular reflection $u(\omega_i, v, \omega_r)$ for filament ($\psi = 0$) given a particular $\mathbf{h} = (\omega_i + \omega_r)/|\omega_i + \omega_r|$.

An example of $v(\omega_i, u, \omega_r)$ for a particular $\mathbf{h}$ and $u = 0$ can be seen in Figure 7.3. The blue circle is the great circle that contains all vectors that are perpendicular to $\mathbf{h}$. The red circle is the set of fiber tangents at $u = 0$. Ideal specular reflection occurs at the intersection of the two circles. It may readily be seen from the figure that certain $\mathbf{h}$ results in a great circle that doesn't intersect the set of fiber tangents, as predicted by Equation 7.4.

For the filament case, the set of tangents forms a great circle. Therefore, the great circle defined by $\mathbf{h}$ always intersects the set of fiber tangents at two points that are π radians apart. An example of $u(\omega_i, v, \omega_r)$ for a particular $\mathbf{h}$ can be seen in Figure 7.4.

7.4 Geometry Factor

Computing the geometry factors in Equation 7.2 or Equation 7.3 requires evaluating the Jacobian of (ϕ, v) or (ϕ, u) with respect to ω_i and the curvature R.

For the Jacobian, we begin by observing that the allowed variation in ω_i is only in directions tangent to the unit sphere (since ω_i is a direction vector that cannot change length). Furthermore, ϕ is unchanged by a small change in ω_i perpendicular to the reflection cone, and u or v is unchanged by a small change in ω_i along the cone. So the determinant of the derivative is the product of the two directional derivatives:

$$\left|\frac{\partial(\phi, v)_k}{\partial \omega_i}\right| = \left|\frac{\partial \phi}{\partial \mathbf{e}_1}\right| \left|\frac{\partial v}{\partial \mathbf{e}_2}\right|$$

where $\mathbf{e}_1$ is the unit vector perpendicular to the cone at ω_i and $\mathbf{e}_2$ is the unit vector tangent to the unit sphere and to the cone at ω_i (see Figure 7.5).

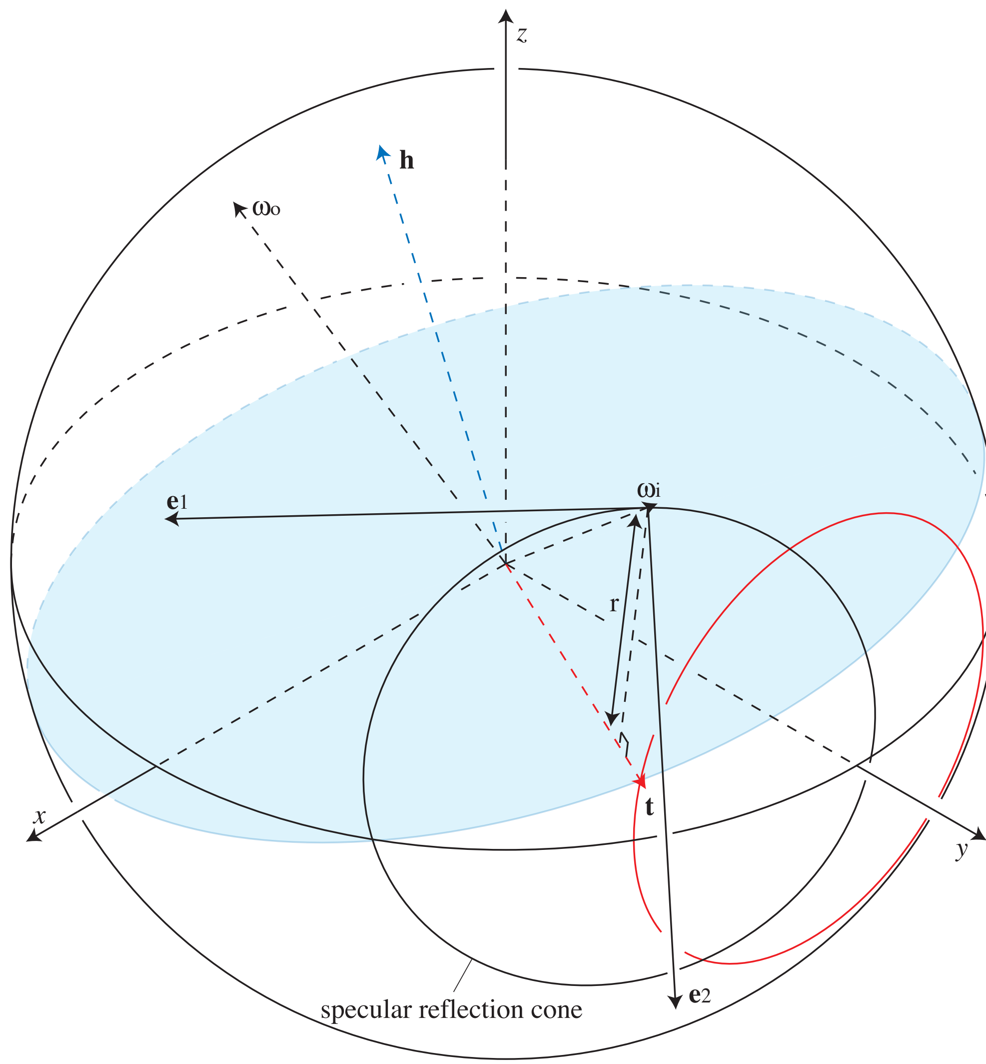

Figure 7.5: Specular reflection cone with the associated $\mathbf{e}_1$, $\mathbf{e}_2$ and the radius r; $\mathbf{e}_1 \perp \mathbf{e}_2$, $\mathbf{e}_1 \perp \omega_i$, and $\mathbf{e}_2 \perp \omega_i$.

Let r be the radius of the circle that is the base of the reflection cone.

$$\begin{aligned} r &= \sin(\mathbf{t}, \omega_i) \\ &= \sqrt{1 - (\mathbf{t} \cdot \omega_i)^2} \end{aligned}$$

An example of a specular reflection cone with the associated $\mathbf{e}_1$, $\mathbf{e}_2$, and the radius r can be seen in Figure 7.5.

By relating the arc length of a circle with its radius and central angle, the $\mathbf{e}_1$ derivative may readily be seen to be:

$$\left| \frac{\partial \phi}{\partial \mathbf{e}_1} \right| = \left| \frac{1}{r} \right|$$

The $\mathbf{e}_2$ derivative can be worked out geometrically by analyzing the effect of perturbing ω_i on the result of intersecting the plane $\mathbf{h} \cdot \mathbf{t} = 0$ with the set of fiber tangent for a fixed u (Figure 7.5). From the figure, we can observe that $\frac{\partial \omega_i}{\partial \mathbf{e}_2} = \frac{\mathbf{t} - (\omega_i \cdot \mathbf{t})\omega_i}{|\mathbf{t} - (\omega_i \cdot \mathbf{t})\omega_i|}$.

$$\begin{aligned} \frac{\partial \omega_i}{\partial \mathbf{e}_2} &= \frac{\mathbf{t} - (\omega_i \cdot \mathbf{t})\omega_i}{|\mathbf{t} - (\omega_i \cdot \mathbf{t})\omega_i|} \\ &= \frac{\mathbf{t} - (\omega_i \cdot \mathbf{t})\omega_i}{\sqrt{(\mathbf{t} - (\omega_i \cdot \mathbf{t})\omega_i)^2}} \\ &= \frac{\mathbf{t} - (\omega_i \cdot \mathbf{t})\omega_i}{\sqrt{\mathbf{t} \cdot \mathbf{t} - 2(\omega_i \cdot \mathbf{t})(\omega_i \cdot \mathbf{t}) + (\omega_i \cdot \mathbf{t})^2(\omega_i \cdot \omega_i)}} \\ &= \frac{\mathbf{t} - (\omega_i \cdot \mathbf{t})\omega_i}{\sqrt{1 - (\omega_i \cdot \mathbf{t})^2}} \\ &= \frac{\mathbf{t} - (\omega_i \cdot \mathbf{t})\omega_i}{r} \end{aligned}$$

Recall from Chapter 2 that:

$$\frac{\partial}{\partial \mathbf{x}} |\mathbf{x}| = \frac{\mathbf{x}^T}{|\mathbf{x}|}$$

We use the fact above to derive $\partial\mathbf{h}$.

$$\begin{aligned}
\frac{\partial\mathbf{h}}{\partial\omega_i} &= \frac{\partial}{\partial\omega_i}\frac{\omega_i+\omega_r}{|\omega_i+\omega_r|} \\
&= \frac{\partial}{\partial\omega_i}(\omega_i+\omega_r)|\omega_i+\omega_r|^{-1} \\
&= \frac{I}{|\omega_i+\omega_r|} - (\omega_i+\omega_r)|\omega_i+\omega_r|^{-2}\frac{\partial}{\partial\omega_i}|\omega_i+\omega_r| \\
&= \frac{I}{|\omega_i+\omega_r|} - (\omega_i+\omega_r)|\omega_i+\omega_r|^{-2}\frac{(\omega_i+\omega_r)^T}{|\omega_i+\omega_r|} \\
&= \frac{I}{|\omega_i+\omega_r|} - \frac{\frac{(\omega_i+\omega_r)}{|\omega_i+\omega_r|}\frac{(\omega_i+\omega_r)^T}{|\omega_i+\omega_r|}}{|\omega_i+\omega_r|} \\
&= \frac{I}{|\omega_i+\omega_r|} - \frac{hh^T}{|\omega_i+\omega_r|} \\
&= \frac{I-\mathbf{h}\mathbf{h}^T}{|\omega_i+\omega_r|} \\
\partial\mathbf{h} &= \frac{I-\mathbf{h}\mathbf{h}^T}{|\omega_i+\omega_r|}\partial\omega_i \\
\partial\mathbf{h} &= \frac{\partial\omega_i-(\mathbf{h}\cdot\partial\omega_i)\mathbf{h}}{|\omega_i+\omega_r|}
\end{aligned}$$

Since $\mathbf{h}$ is normal of a great circle (Figure 7.5), changing $\mathbf{h}$ rotates the great circle. Let $\partial\mathbf{a}$ be the vector that describes the axis of rotation as well as the magnitude. Note that the second term in $\partial\mathbf{h}$ becomes 0 by the cross product with $\mathbf{h}$ and we have:

$$\begin{aligned}
\partial\mathbf{a} &= \mathbf{h}\times\partial\mathbf{h} \\
&= \mathbf{h}\times\frac{\partial\omega_i}{|\omega_i+\omega_r|}
\end{aligned}$$

Next we want to compute how much the great circle shifts at the point of intersection with the set of fiber tangents when we rotate it (Figure 7.6). We use

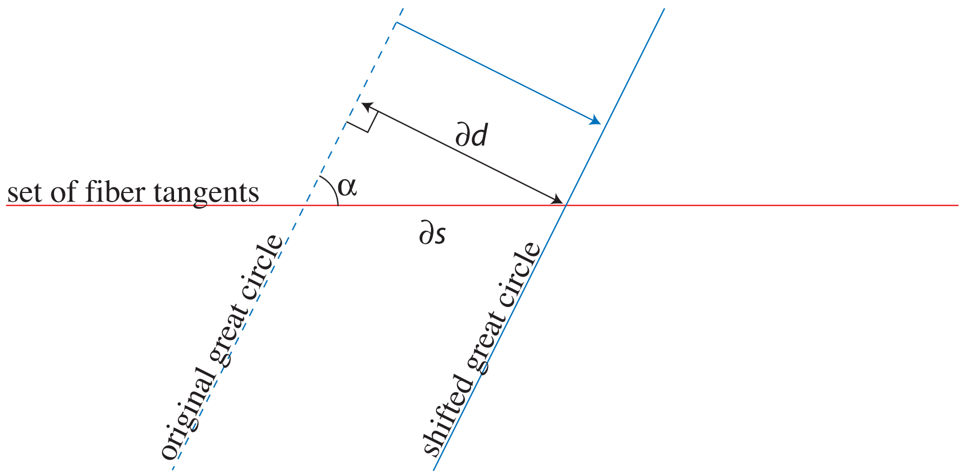

Figure 7.6: Original and shifted great circles and their intersections with the set of fiber tangents.

vector triple product (Equation 2.14) in the derivation below.

$$
\begin{aligned}
\partial d &= |\partial \mathbf{a} \times \mathbf{t}| \\
&= \tfrac{|(\mathbf{h} \times \partial \omega_i) \times \mathbf{t}|}{|\omega_i + \omega_r|} \\
&= \tfrac{|(\mathbf{t} \cdot \mathbf{h}) \partial \omega_i - (\mathbf{t} \cdot \partial \omega_i) \mathbf{h}|}{|\omega_i + \omega_r|} \\
&= \tfrac{|-(\mathbf{t} \cdot \partial \omega_i) \mathbf{h}|}{|\omega_i + \omega_r|} \\
&= \tfrac{\mathbf{t} \cdot \partial \omega_i}{|\omega_i + \omega_r|} \\
&= \tfrac{\mathbf{t} \cdot \mathbf{t} - (\omega_i \cdot \mathbf{t})(\mathbf{t} \cdot \omega_i)}{r|\omega_i + \omega_r|} \partial \mathbf{e}_2 \\
&= \tfrac{1 - (\omega_i \cdot \mathbf{t})^2}{r|\omega_i + \omega_r|} \partial \mathbf{e}_2 \\
&= \tfrac{r}{|\omega_i + \omega_r|} \partial \mathbf{e}_2
\end{aligned}
$$

We now compute $\sin \alpha$, where α is the angle the great circle makes with the set of fiber tangents (Figure 7.6). This can be computed by taking the magnitude of the cross product of the vector tangent to the great circle and the vector tangent to the set of fiber tangents at the intersection point. The former is $\mathbf{t} \times \mathbf{h}$ and the latter is simply the torus normal $\mathbf{n}$ at that point.

$$\begin{aligned}\sin\alpha &= |(\mathbf{t}\times\mathbf{h})\times\mathbf{n}| \\ &= |(\mathbf{n}\cdot\mathbf{t})\mathbf{h}-(\mathbf{n}\cdot\mathbf{h})\mathbf{t}| \\ &= |-(\mathbf{n}\cdot\mathbf{h})\mathbf{t}| \\ &= \mathbf{n}\cdot\mathbf{h}\end{aligned}$$

We can now compute the distance the intersection point moves because of the change in the great circle.

$$\begin{aligned}\partial s &= \tfrac{\partial d}{\sin\alpha} \\ &= \tfrac{r}{|\omega_i+\omega_r|(\mathbf{n}\cdot\mathbf{h})}\partial\mathbf{e}_2\end{aligned}$$

Finally, we relate the arc length ∂s and the radius of the circle that is formed by the set of fiber tangents to the central angle ∂v. Recall from Subsection 6.2.1 that, for a fixed u, the set of fiber tangents $\mathbf{t}(u,v)$ forms a circle of radius $|\sin\psi|$.

$$\begin{aligned}\partial v &= \tfrac{\partial s}{|\sin\psi|} \\ &= \tfrac{r}{|\omega_i+\omega_r|(\mathbf{n}\cdot\mathbf{h})|\sin\psi|}\partial\mathbf{e}_2 \\ \left|\tfrac{\partial v}{\partial\mathbf{e}_2}\right| &= \left|\tfrac{r}{|\omega_i+\omega_r|(\mathbf{n}\cdot\mathbf{h})|\sin\psi|}\right|\end{aligned}$$

Therefore, we have:

$$G_v(\omega_i,u,\omega_r)=\frac{a(R(u)+a\cos v_k)}{|\omega_i+\omega_r|(\mathbf{n}\cdot\mathbf{h})|\sin\psi|} \tag{7.6}$$

We now turn our attention to the filament case and derive the following term.

$$\left|\frac{\partial(\phi,u)_k}{\partial\omega_i}\right|=\left|\frac{\partial\phi}{\partial\mathbf{e}_1}\right|\left|\frac{\partial u}{\partial\mathbf{e}_2}\right|$$

An example of a specular reflection cone with the associated $\mathbf{e}_1$, $\mathbf{e}_2$, and the radius r for filament can be seen in Figure 7.7.

The derivation up to ∂d is exactly the same as in the previous subsection. Similar to the other case, $\sin\alpha$ can be computed by taking the magnitude of the

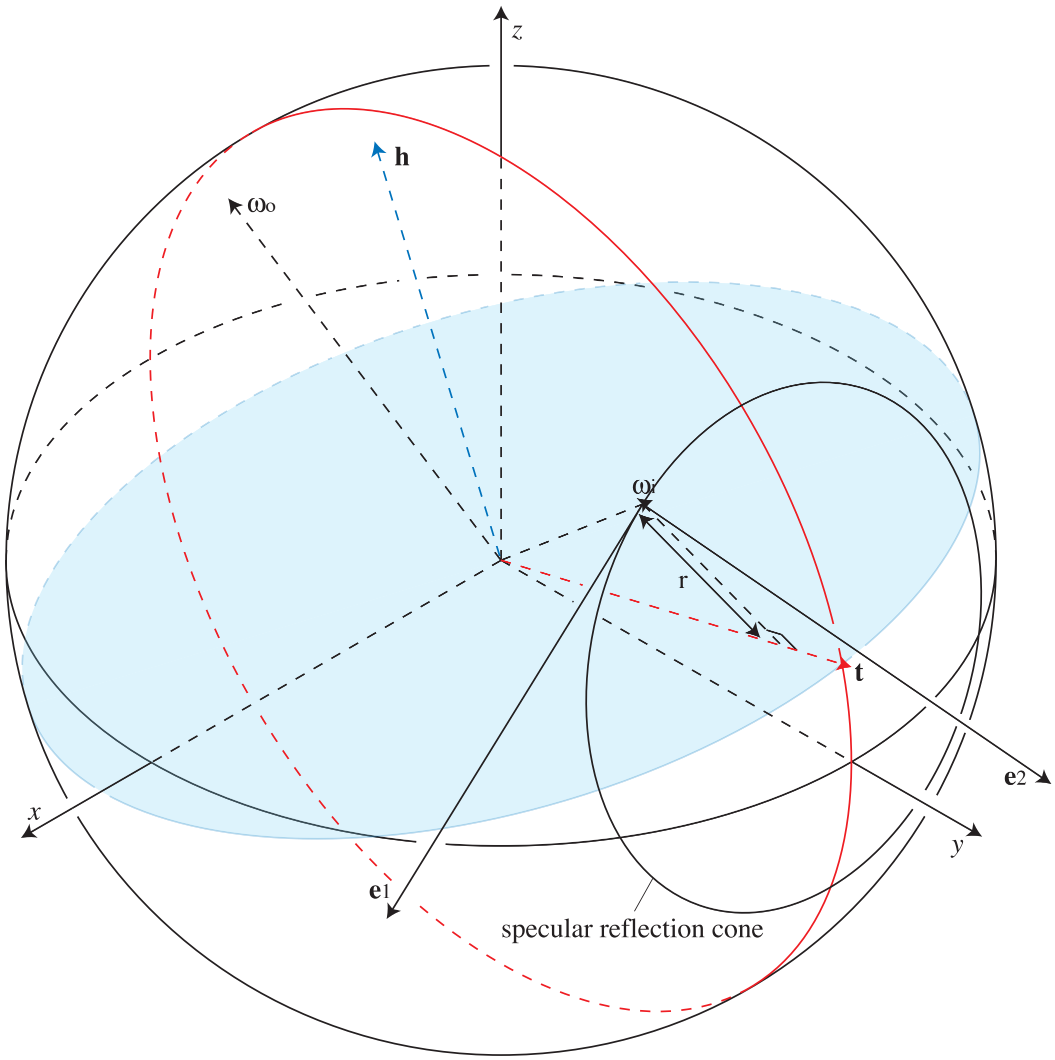

Figure 7.7: Specular reflection cone with the associated $\mathbf{e}_1$, $\mathbf{e}_2$ and the radius r for filament; $\mathbf{e}_1 \perp \mathbf{e}_2$, $\mathbf{e}_1 \perp \omega_i$, and $\mathbf{e}_2 \perp \omega_i$.

cross product of the vector tangent to the great circle and the vector tangent to the set of fiber tangents at the intersection point. The former is still $\mathbf{t} \times \mathbf{h}$; however, the latter is now $\frac{\mathbf{t}\times(1,0,0)^T}{|\mathbf{t}\times(1,0,0)^T|}$. Note that, for filament, $\mathbf{t} \perp (1,0,0)^T$ and therefore $|\mathbf{t} \times (1,0,0)^T| = 1$.

$$\begin{aligned}
\sin\alpha &= \left|(\mathbf{t} \times \mathbf{h}) \times (\mathbf{t} \times (1,0,0)^T)\right| \\
&= \left|((\mathbf{t} \times (1,0,0)^T) \cdot \mathbf{t})\mathbf{h} - ((\mathbf{t} \times (1,0,0)^T) \cdot \mathbf{h})\mathbf{t}\right| \\
&= \left|-((\mathbf{t} \times (1,0,0)^T) \cdot \mathbf{h})\mathbf{t}\right| \\
&= \left|(\mathbf{t} \times (1,0,0)^T) \cdot \mathbf{h}\right| \\
&= |(\mathbf{t} \times \mathbf{h})_x|
\end{aligned}$$

That is, $\sin\alpha$ equals the x component of $\mathbf{t} \times \mathbf{h}$.

We can now compute the distance the intersection point moves because of the change in the great circle.

$$\begin{aligned}
\partial s &= \tfrac{\partial d}{\sin\alpha} \\
&= \tfrac{r}{|\omega_i+\omega_r||(\mathbf{t}\times\mathbf{h})_x|}\partial \mathbf{e}_2
\end{aligned}$$

Finally, we relate the arc length ∂s and the radius of the circle that is formed by the set of fiber tangents to the central angle ∂u. For filament, the circle formed by the set of fiber tangents has radius of 1.

$$\begin{aligned}
\partial u &= \tfrac{\partial s}{1} \\
&= \tfrac{r}{|\omega_i+\omega_r||(\mathbf{t}\times\mathbf{h})_x|}\partial \mathbf{e}_2 \\
\left|\tfrac{\partial u}{\partial \mathbf{e}_2}\right| &= \left|\tfrac{r}{|\omega_i+\omega_r||(\mathbf{t}\times\mathbf{h})_x|}\right|
\end{aligned}$$

Therefore, we have:

$$G_u(\omega_i, v, \omega_r) = \frac{a(R(u_k) + a\cos v)}{|\omega_i + \omega_r||(\mathbf{t} \times \mathbf{h})_x|} \tag{7.7}$$

This completes the derivation of the geometry factors.

7.5 Phase Function

The phase function is a physical property of a particular type of fiber. Note that the desired phase function is not the phase function of an individual fiber but a phase function describing the effects of multiple scattering events occurring nearby in the yarn, all encountering the same fiber tangent. Since the fibers share the same tangent, the multiply scattered light will still stay in the specular cone, but will be more spread out around the cone.

Investigating the scattering properties of individual yarns and fibers in isolation to discover and model their behavior is an important research topic that is beyond the scope of the current work. Instead we use a generic phase function with the appropriate general properties that can be tuned to model different fibers. Preliminary measurements of single-fiber scattering, together with experience fitting the model to data, suggest that the phase function should be predominantly forward scattering, with a smaller uniform component. To this end we use a phase function that is the sum of a constant and a forward-directed lobe; we use the von Mises distribution [13], evaluated for the angle between the incident and exitant directions, for the lobe:

$$\begin{aligned} f_c(\theta_r, \phi) &= \alpha + g(-\omega_i \cdot \omega_r, \beta) \\ g(\cos x, b) &= \tfrac{\exp(b \cos x)}{2\pi I_0(b)} \end{aligned} \tag{7.8}$$

where α is the uniform scattering parameter, β is the forward scattering parameter, and $I_0(x)$ is a modified Bessel function of the first kind of order 0 [2]. We chose the von Mises function because it is continuous around the circle and has proven to work well in practice.

7.6 Attenuation Function

The attenuation function A describes the attenuation of light by other fibers on the way into and out of the yarn. Our framework allows A to let light scatter through the fiber, even when the scattering point is not facing both the light source and the camera. After some experiments with sophisticated models for A, we found that a very simple model, which is the limit of the more general case for shallow penetration depths, worked well. In this limit the curvature of the yarn surface may be neglected and Seeliger's law, which describes scattering from a medium below a flat surface [21], applies:

$$A(\omega_i, u, v, \omega_r) = \frac{\sigma_s}{\sigma_t} \frac{(\omega_i \cdot \mathbf{n})(\omega_r \cdot \mathbf{n})}{\omega_i \cdot \mathbf{n} + \omega_r \cdot \mathbf{n}} \tag{7.9}$$

where $\mathbf{n} = \mathbf{n}(u, v)$ and the dot products are all clamped to nonnegative values. This is the attenuation function we used for the results. The albedo σ_s/σ_t is unimportant because it can be absorbed into the specular coefficient. An important feature of this model is that it is zero when $\mathbf{h} \cdot \mathbf{n} < 0$, which guarantees that Equation 7.4 has at most one solution, making the sum over k in Equation 7.2 unnecessary.

For filament fibers, because the highlight will maintain full intensity right up to the moment it falls off the end of the segment (when $u(v)$ becomes greater then $u_{\max}$), it's necessary to include some form of smoothing at the ends of the integration domain, to simulate the gradual disappearance of the imperfect highlight in a real material (as contrasted with the sudden disappearance of the ideally sharp highlight in the model). We simply use a smoothstep cubic to fade out the contribution to the integral smoothly over an interval leading up to $u = u_{\max}$:

$$A_s(u) = A(u) \left(1 - s\left(\frac{|u| - (1 - \delta)u_{\max}}{\delta u_{\max}}\right)\right) \tag{7.10}$$

where $s(x)$ is a smooth step function that is 0 for $x \leq 0$ and 1 for $x \geq 1$ and smooth in value and derivative in between, and $0 \leq \delta < 1$ is filament smoothing parameter (δu_{max} is the size of the range over which the contribution ramps down).

Chapter 8

Reflectance Model and Texture Model

This chapter describes our two physically based appearance models for woven cloth: the reflectance model and the texture model. The reflectance model is used when only the reflectance of the fabric matters (for example, when the fabric is far enough from the camera that the texture is not visible). In contrast, as the name implies, the texture model is able to model the texture of the fabric. Both models are based on the results developed in the previous two chapters. Because of this, both models have the same BRDF and, therefore, switching between the models doesn't require any additional adjustments.

8.1 Reflectance Model

In the previous chapter, we derived the scattering functions $f_s(\omega_i, \omega_r)$ and explain the various components of the function. However, the function we actually need for rendering is the BRDF, $f_r(\omega_i, \omega_r)$, which describes the contribution of incident irradiance falling on the cloth surface from the direction ω_i to reflected radiance leaving the surface in the direction ω_r. With no consideration for correlated shadowing–masking or interreflection, we can derive f_r from f_s by assuming that light scatters from a segment according to f_s regardless of where it hits the segment, and also that the scattered light has the same probability of escaping the surface regardless of where it leaves the segment.

Under this assumption, we can apportion the incident irradiance uniformly to all the segments, so that each segment receives an average radiance of $L_i(\omega_i)\,(\omega_i)_z$ where $(\omega_i)_z$ is the z component of ω_i. The fraction of light escaping is also assumed to be proportional to $(\omega_i)_z$, and since the projected area over which it escapes is proportional to $(\omega_i)_z$, the radiance is simply proportional to the intensity of the segments.

This makes the relationship between f_r and f_s very simple: $f_r(\omega_i, \omega_r)$ is directly proportional to $f_s(\omega_i, \omega_r)$, and the constant of proportionality can be absorbed into the specular coefficient. Therefore f_s will serve directly as the specular component of our reflectance model.

There are, therefore, two ways to compute the BRDF, depending on how we parameterize the integral:

$$f_{r,s}(\omega_i, \omega_r) = \int_{-u_{\max}}^{u_{\max}} G_v f_c A \, du \quad \text{or} \quad f_{r,s}(\omega_i, \omega_r) = \int_0^{2\pi} G_u f_c A \, dv. \tag{8.1}$$

As noted in Chapter 7, we integrate over u for staple yarns and over v for filament yarns.

8.2 Texture Model

In order for a fabric to look realistic, the distinctive texture of reflections from individual yarns must be reproduced when the cloth is rendered at high enough magnification. All that is required for good results is to very roughly predict the position and shape of the highlight; if the magnification is high enough to resolve details within a yarn, a more detailed model such as lumislice rendering [51] must be used.

Since our reflectance model already computes the highlight location in order to evaluate the various geometry-dependent terms, we can make use of this information to "unroll" the integrand into a texture in a way that satisfies the constraint that the average brightness in texture space equals the value of the BRDF. We do

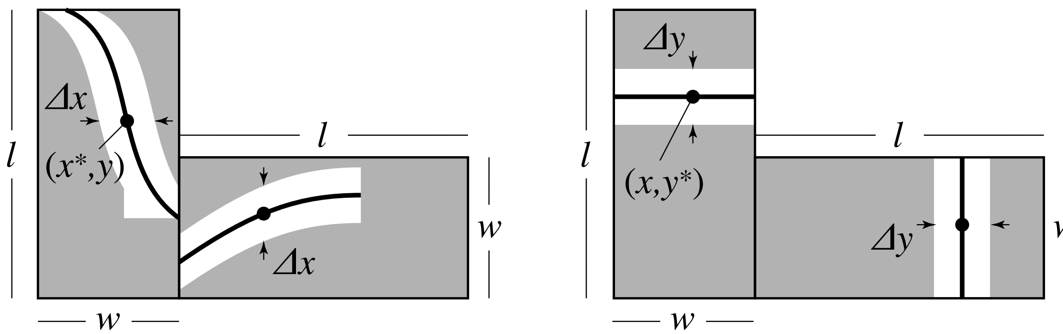

Figure 8.1: The specular highlight in the texture is a fixed-width band around the ideal highlight curve.

this by mapping u and v linearly to the segment rectangle on the cloth surface. In the texture space, the segment rectangle is parameterized by $-w/2 \le x \le w/2$ and $-l/2 \le y \le l/2$ (recall that w and l are the width and length of the segment rectangle). To unroll the yarn surface we map (x, y) to (u, v) using

$$\begin{aligned} u &= \frac{2u_{\max}}{l} y \\ v &= \frac{\pi}{w} x \end{aligned} \tag{8.2}$$

This approach ignores visibility and foreshortening effects, but it nonetheless produces a realistic highlight texture.

The scattering model predicts an infinitely thin highlight, whose shape is defined by the function $v(u, \omega_i)$ or $u(v, \omega_i)$. We widen this curve into a band of constant width in the dependent coordinate: a constant width Δx for staple yarns and constant width Δy for filament yarns. Therefore, the texture model returns a non-zero value only if the point (x, y) lands inside this band of constant width. This process is illustrated in Figure 8.1.

We can find whether (x, y) lands inside the band as follows: first use Equation 8.2 to map y (or x) to get u (or v). Then compute the location of ideal specular reflection $v(\omega_i, u, \omega_r)$ (or $u(\omega_i, v, \omega_r)$) using Equation 7.4 (or Equation 7.5). Next use Equation 8.2 to remap $v(\omega_i, u, \omega_r)$ (or $u(\omega_i, v, \omega_r)$) to get $x(v)$ (or $y(u)$). Finally, clamp $x(v)$ to the range $\pm(w - \Delta x)/2$ (or clamp $y(u)$ to the range $\pm(l - \Delta y)/2$). The point (x, y) lands inside the band if and only if $|x - x(v)| < \Delta x/2$ (or $|y - y(u)| < \Delta y/2$). We can encode this in a function $\chi(x, y, \omega_i, \omega_r)$ defined as follows:

$$\chi = \begin{cases} 1 & \text{if } |x - x(v)| < \frac{\Delta x}{2} \\ 0 & otherwise \end{cases} \quad \text{or} \quad \chi = \begin{cases} 1 & \text{if } |y - y(u)| < \frac{\Delta y}{2} \\ 0 & otherwise \end{cases} . \tag{8.3}$$

If the reflectance model is a BRDF $f_{r,s}(\omega_i, \omega_r)$, the texture model is a BTF (bidirectional texture function) $T(x, y, \omega_i, \omega_r)$. Recall that we have the constraint that the average brightness in texture space equals the value of the BRDF. Mathematically, this is expressed as follows:

$$f_{r,s}(\omega_i, \omega_r) = \frac{1}{lw} \int_A T(x, y, \omega_i, \omega_r) dA. \tag{8.4}$$

Depending on how we parameterize the equation above, we have:

$$\frac{1}{lw} \int_{-l/2}^{l/2} T(x, y, \omega_i, \omega_r) \Delta x dy \quad \text{or} \quad \frac{1}{lw} \int_{-w/2}^{w/2} T(x, y, \omega_i, \omega_r) \Delta y dx$$

for the staple or filament case. The brightness of the specular reflection, which varies along the highlight but not across it, is calculated to match the average value of the texture to the BRDF. To make these averages match Equation 8.1 we need:

$$\begin{aligned} T(x, y, \omega_i, \omega_r) &= \chi lw G_u f_c A \left| \frac{du}{dy} \right| \frac{1}{\Delta x} \\ &= \chi lw G_u f_c A \frac{2u_{\max}}{l} \frac{1}{\Delta x} \\ &= \chi 2w u_{\max} G_u f_c A \frac{1}{\Delta x} \end{aligned} \quad \text{or} \quad \begin{aligned} T(x, y, \omega_i, \omega_r) &= \chi lw G_v f_c A \left| \frac{dv}{dx} \right| \frac{1}{\Delta y} \\ &= \chi lw G_v f_c A \frac{\pi}{w} \frac{1}{\Delta y} \\ &= \chi \pi l G_v f_c A \frac{1}{\Delta y} \end{aligned} . \tag{8.5}$$

With the BTF defined in this way, the average value of the texture over a region of the image with constant shading geometry will match the value of the BRDF:

Figure 8.2: Illustration of the texture at three different magnifications, each a factor of two from its neighbor. The simple, blocky shape of individual highlights is sufficient to represent the appearance of the ribs found in twill cloth.

in essence, the antialiasing filter of the rendering system is performing the integral that is done by quadrature in the reflectance model.

The result of the texture model for the black twill cloth can be seen in three different magnifications in Figure 8.2. Despite the simple, blocky shape of individual highlights, together they form an accurate representation of the ribs found in twill cloth and only at a very large magnification do they look artificial.

8.2.1 Noise

Since most textiles are not perfectly regular, we introduced two simple noise sources to improve the appearance of the renderings. Although noise is *ad hoc* and essentially separate from the model, the randomness is very important for visual quality.

To model irregularities in fiber structure, we scale the brightness of the specular component by a fixed noise texture with values drawn from the exponential distribution (between 0 and ∞ with mean 1). The noise is constant over each of a grid of k by k rectangles in a yarn segment. The parameter k controls the coarseness of the noise. This signal-independent multiplicative noise will not affect the average BRDF.

The shape of a yarn segment depends on the stiffness and the tension of the yarn, as well as the stiffness and the tension of the yarn crossing under the segment. In some materials these yarn properties vary significantly but slowly along the yarns, leading to a distinctive cross-hatch texture traditionally seen in linen and silk materials. We define a 1D Perlin noise function along each yarn and modulate $u_{\max}$ for a segment based on the noise values for its yarn and also the yarns crossing it.

8.3 Computing the Models

Our model defines a function of ω_i and ω_r based on the parameters in Table 8.1, which describe the fibers, the yarns, and the weave pattern. All these parameters (other than the specular and diffuse coefficients) are directly meaningful in terms of the physical model of the fabric. A complete description of a fabric starts with a single set of fiber parameters and diffuse coefficients. Then for each distinct type of yarn segment in the weave pattern, we need a set of yarn and weave parameters and a specular coefficient. All the examples in this paper have two distinct segment types, one warp and one weft.

The models are defined as the sum of a diffuse component and a specular component for each segment:

$$k_d + \sum_j k_{s,j} f_{r,j}(\omega_i, \omega_r)$$

where k_d and the $k_{s,j}$ are the diffuse coefficient and the specular coefficients.

If one is interested only in the reflectance of the fabric but not in the texture,

Table 8.1: All the parameters of the reflectance model.

Parameter	Purpose	Typical values
Fiber properties		
α	uniform scattering	0 to 0.1
β	forward scattering	2 to 5
δ	filament smoothing	0 to 1
Yarn geometry		
ψ	fiber twist angle	$-\pi/2$ to $\pi/2$
$u_{\max}$	maximum inclination angle	0 to $\pi/2$
κ	spine curvature	-1 to ∞
Weave pattern		
w	width of segment rectangle	0.1 mm to 1 mm
l	length of segment rectangle	0.1 mm to 1 cm
Coefficients		
k_s	specular coefficient	0 to ∞
k_d	diffuse coefficient	0 to ∞

the reflectance model is sufficient. On the reflectance model, the BRDF $f_r(\omega_i, \omega_r)$ is evaluated by computing the integral in Equation 8.1 using the parameters for the j^{th} segment type (normally one for warp and one for weft). In most cases this must be done numerically. The plots for this work were computed using the default quadrature routine in MATLAB. In practice, however, simple numerical integration methods (such as Trapezoidal Rule with 11 samples) are sufficient since the integrand is well behaved and no special precautions are required in integrating it.

If, instead, the texture of the fabric is desired, one has to use the texture model. In the texture model, as stated earlier, the integration in the BRDF $f_r(\omega_i, \omega_r)$ is performed automatically by the antialiasing filter of the rendering system. That is, only the integrand needs to be evaluated and no quadrature is required. Therefore, whether on the reflectance model or on the texture model, we need to evaluate the integrand.

8.3.1 Staple yarn

The algorithm is as follows: given texture coordinates on the cloth, find the type of yarn segment, j, that the shading point falls into and the (x, y) coordinates relative to the center of that segment's rectangle. Compute u from y using Equation 8.2 and then find the point where the ideal specular reflection occurs $v(\omega_i, u, \omega_r)$ using Equation 7.4. Next, we evaluate the geometry factor G_v using Equation 7.6, the phase function f_c using Equation 7.8, and the attenuation function A using Equation 7.9. Multiply the three together and we have the integrand. On the reflectance model, depending on the numerical integration method used, this process is repeated several times on different points on the fabric. The pseudocode for the reflectance model on staple yarn can be seen in Algorithms 1 and 2.

On the texture model, we instead compute $x(v)$ from this $v(\omega_i, u, \omega_r)$ using Equation 8.2 and clamp it to the range $\pm(w - \Delta x)/2$. Compute χ using Equation 8.3. Finally, compute the BTF $T(x, y, \omega_i, \omega_r)$ using Equation 8.5 and return the sum of $k_s T(x, y, \omega_i, \omega_r)$ and k_d. The pseudocode for the texture model on staple yarn can be seen in Algorithm 5.

8.3.2 Filament yarn

The algorithm is as follows: given texture coordinates on the cloth, find the type of yarn segment, j, that the shading point falls into and the (x, y) coordinates relative to the center of that segment's rectangle. Compute v from x using Equation 8.2 and then find the point where the ideal specular reflection occurs $u(\omega_i, v, \omega_r)$ using Equation 7.5. Next we evaluate the geometry factor G_u using Equation 7.7, the phase function f_c using Equation 7.8, and the attenuation function A_s using Equation 7.9 and Equation 7.10. Multiply the three together and we have the integrand. On the reflectance model, depending on the numerical integration method used, this process is repeated several times on different points on the fabric. The pseudocode for the reflectance model on filament yarn can be seen in Algorithms 3 and 4.

On the texture model, we instead compute $y(u)$ from this $u(\omega_i, v, \omega_r)$ using Equation 8.2 and clamp it to the range $\pm(l - \Delta y)/2$. Compute χ using Equation 8.3. Finally, compute the BTF $T(x, y, \omega_i, \omega_r)$ using Equation 8.5 and return the sum of $k_s T(x, y, \omega_i, \omega_r)$ and k_d. The pseudocode for the texture model on filament yarn can be seen in Algorithm 6.

```
f_r(ω_i, ω_r) = integrate staple integrand from −u_max to u_max;
return k_d + k_s f_r(ω_i, ω_r);
```

Algorithm 1: Reflectance model on staple yarn

```
Compute u from y using (8.2);
Compute ideal specular reflection location v(ω_i, u, ω_r) using (7.4);
if |v(ω_i, u, ω_r)| < π/2 then
    Compute G_v using (7.6);
    Compute f_c using (7.8);
    Compute A using (7.9);
    return G_v f_c A;
else
    // ideal specular reflection is not visible
    return 0;
end
```

Algorithm 2: Staple integrand

```
fr(ωi, ωr) = integrate filament integrand from −π/2 to π/2;
return kd + ks fr(ωi, ωr);
```

Algorithm 3: Reflectance model on filament yarn

```
Compute v from x using (8.2);
Compute ideal specular reflection location u(ωi, v, ωr) using (7.5);
if |u(ωi, v, ωr)| < u_max then
    Compute G_u using (7.7);
    Compute f_c using (7.8);
    Compute A_s using (7.9) and (7.10);
    return G_u f_c A_s;
else
    // ideal specular reflection is not visible
    return 0;
end
```

Algorithm 4: Filament integrand

Compute u from y using (8.2);
Compute ideal specular reflection location $v(\omega_i, u, \omega_r)$ using (7.4);
if $|v(\omega_i, u, \omega_r)| < \pi/2$ **then**
    Compute G_v using (7.6);
    Compute f_c using (7.8);
    Compute A using (7.9);
    Compute $x(v)$ from $v(\omega_i, u, \omega_r)$ using (8.2);
    Clamp $x(v)$ to the range $\pm(w - \Delta x)/2$;
    Compute χ using (8.3);
    Compute BTF $T(x, y, \omega_i, \omega_r)$ using (8.5);
    return $k_d + k_s T(x, y, \omega_i, \omega_r)$;
else
    `// ideal specular reflection is not visible`
    return 0;
end

Algorithm 5: Texture model on staple yarn

```
Compute $v$ from $x$ using (8.2);
Compute ideal specular reflection location $u(\omega_i, v, \omega_r)$ using (7.5);
if $|u(\omega_i, v, \omega_r)| < u_{max}$ then
    Compute $G_u$ using (7.7);
    Compute $f_c$ using (7.8);
    Compute $A_s$ using (7.9) and (7.10);
    Compute $y(u)$ from $u(\omega_i, v, \omega_r)$ using (8.2);
    Clamp $y(u)$ to the range $\pm(l - \Delta y)/2$;
    Compute $\chi$ using (8.3);
    Compute BTF $T(x, y, \omega_i, \omega_r)$ using (8.5);
    return $k_d + k_s T(x, y, \omega_i, \omega_r)$;
else
    // ideal specular reflection is not visible
    return 0;
end
```

Algorithm 6: Texture model on filament yarn

Chapter 9

Results

We implemented our reflectance model in MATLAB for data fitting and the texture model in a Monte Carlo ray tracing system written in Java for rendering. In the renderer, the cloth model acts as a spatially varying BRDF. It receives texture coordinates, a shading frame, and incident and exitant directions, and it uses the texture model to compute a BRDF value that is returned to the system.

The general behavior of the model can be understood starting from the degenerate case of $\psi = 0$ and $u_{\max} = \epsilon$ (for a small nonzero ϵ), which describes a surface covered with parallel, perfectly specular fibers and would produce a very bright and thin anisotropic highlight (like a machined metal surface). As $u_{\max}$ is increased, the range of tangents present expands, causing the highlight to spread out. The distribution of intensity across the highlight is controlled by the shape of the yarn segment. A circular torus creates a fairly uniform highlight; a shape that is straighter near the ends leads to bright edges (as seen in the polyester); a shape that is flatter near the middle would lead to a highlight that falls off smoothly with long tails. In this filament mode, the model behaves somewhat like (though not identically to) a microfacet BRDF with a long, narrow facet normal distribution. Increasing $u_{\max}$ from zero also causes the highlight to broaden, but in a different and asymmetric way. The fiber parameters control the intensity disribution *along* the highlight. The weave parameters principally serve to establish the texture and to balance the brightness of warp and weft, though they do subtly affect the reflection pattern by affecting the relationship between R and a.

To compare our model to the BRDF data, we selected parameters by a com-

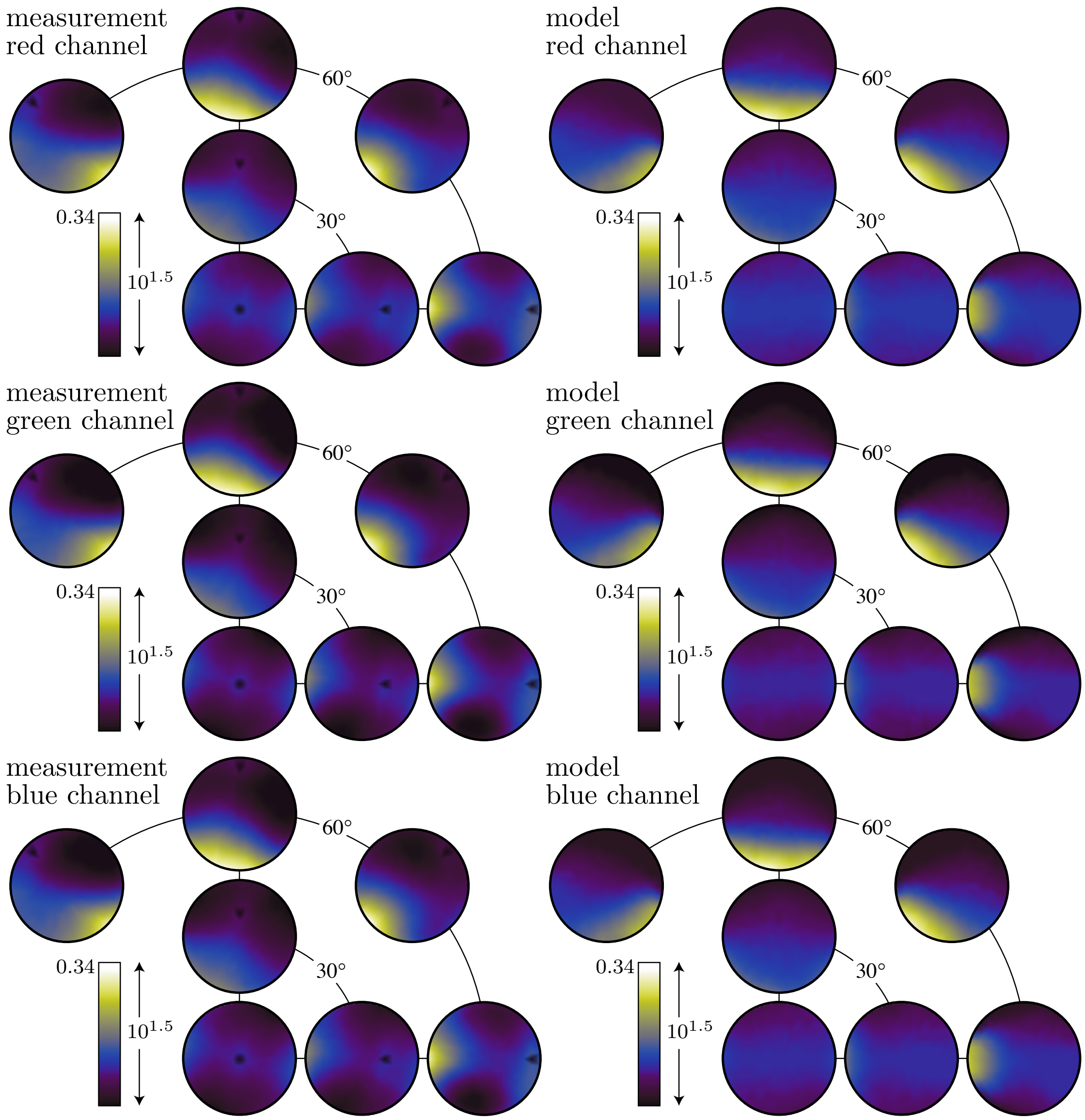

Figure 9.1: BRDF comparison: cotton twill.

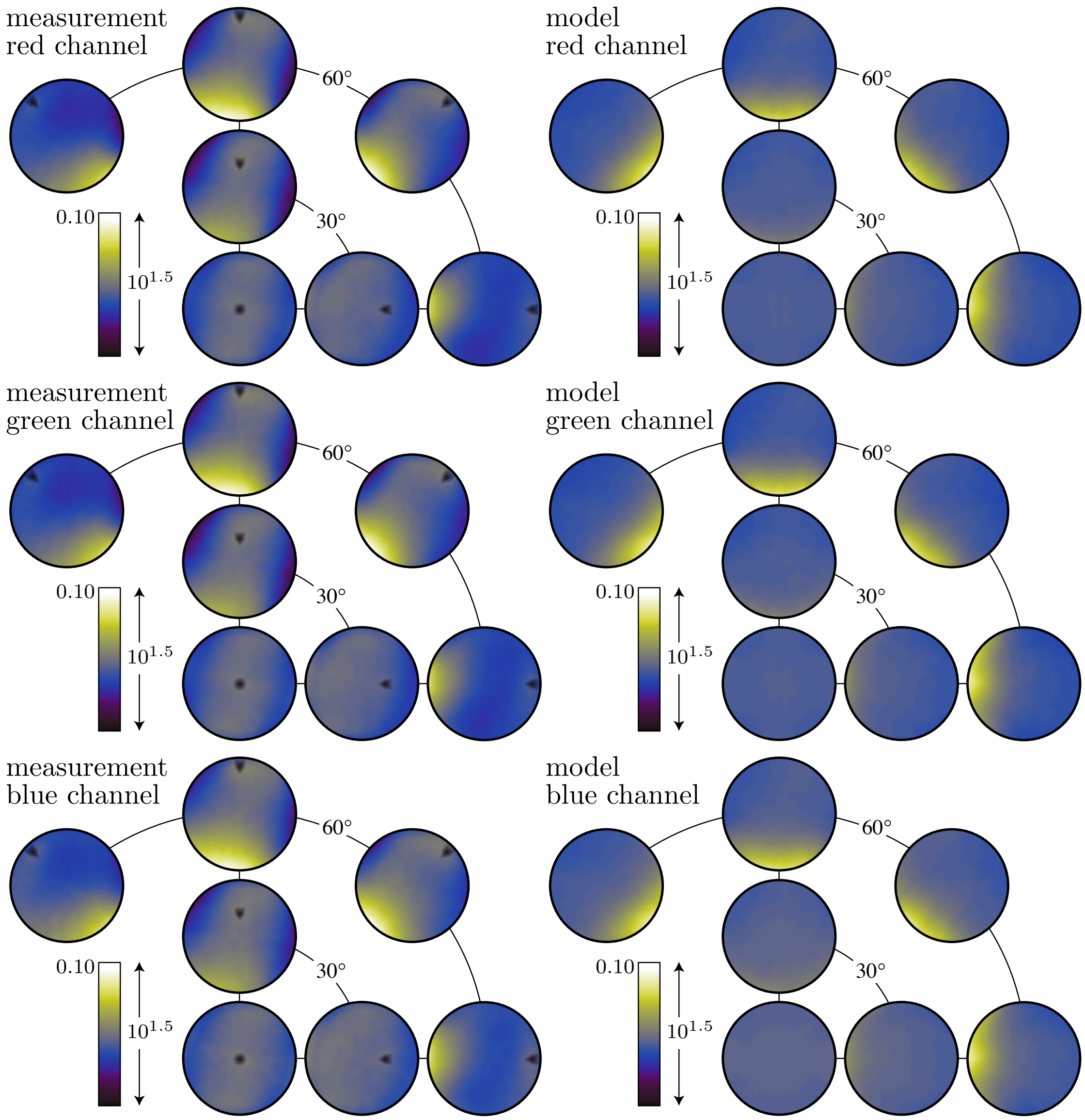

Figure 9.2: BRDF comparison: cotton denim.

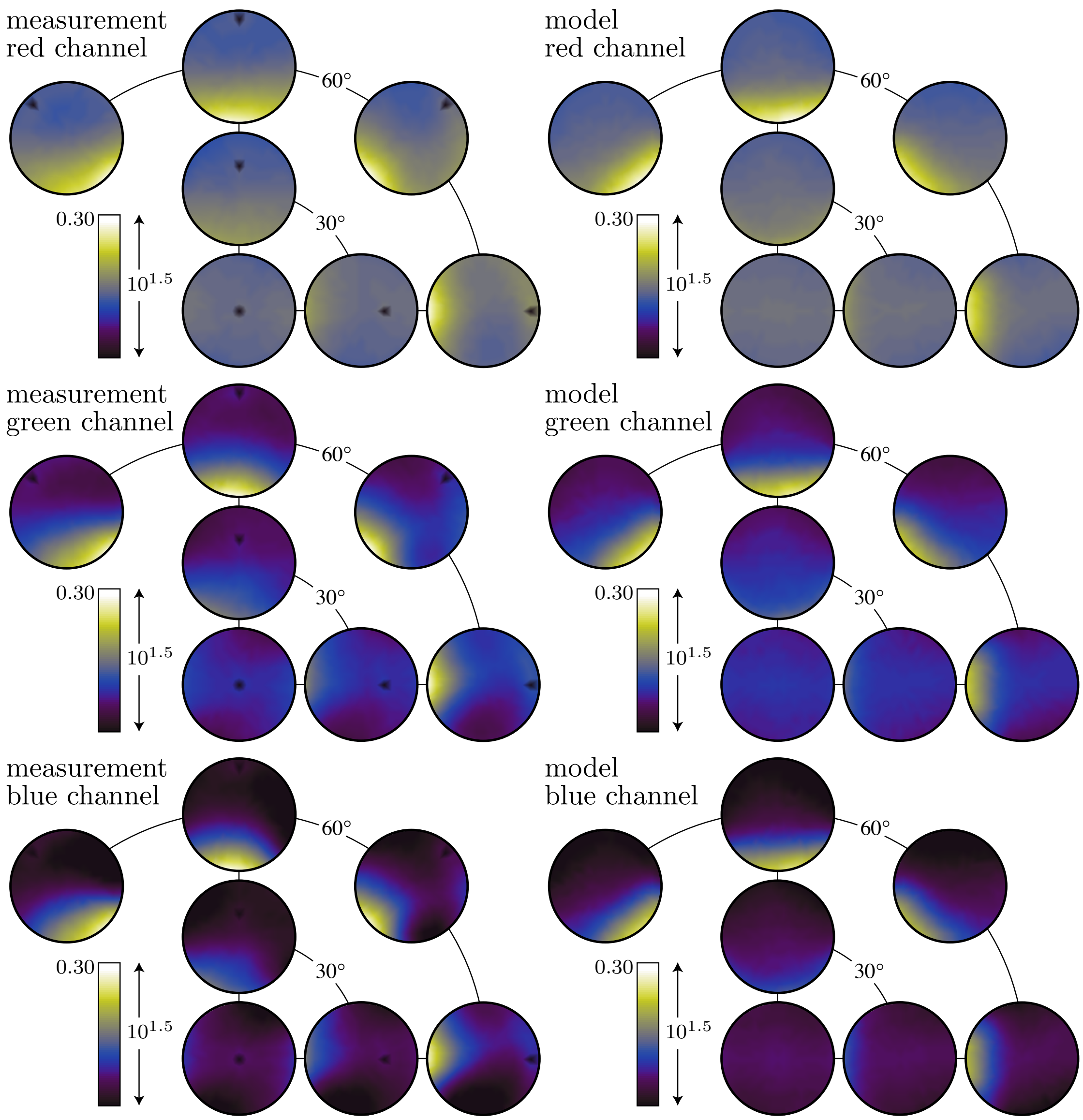

Figure 9.3: BRDF comparison: wool gabardine.

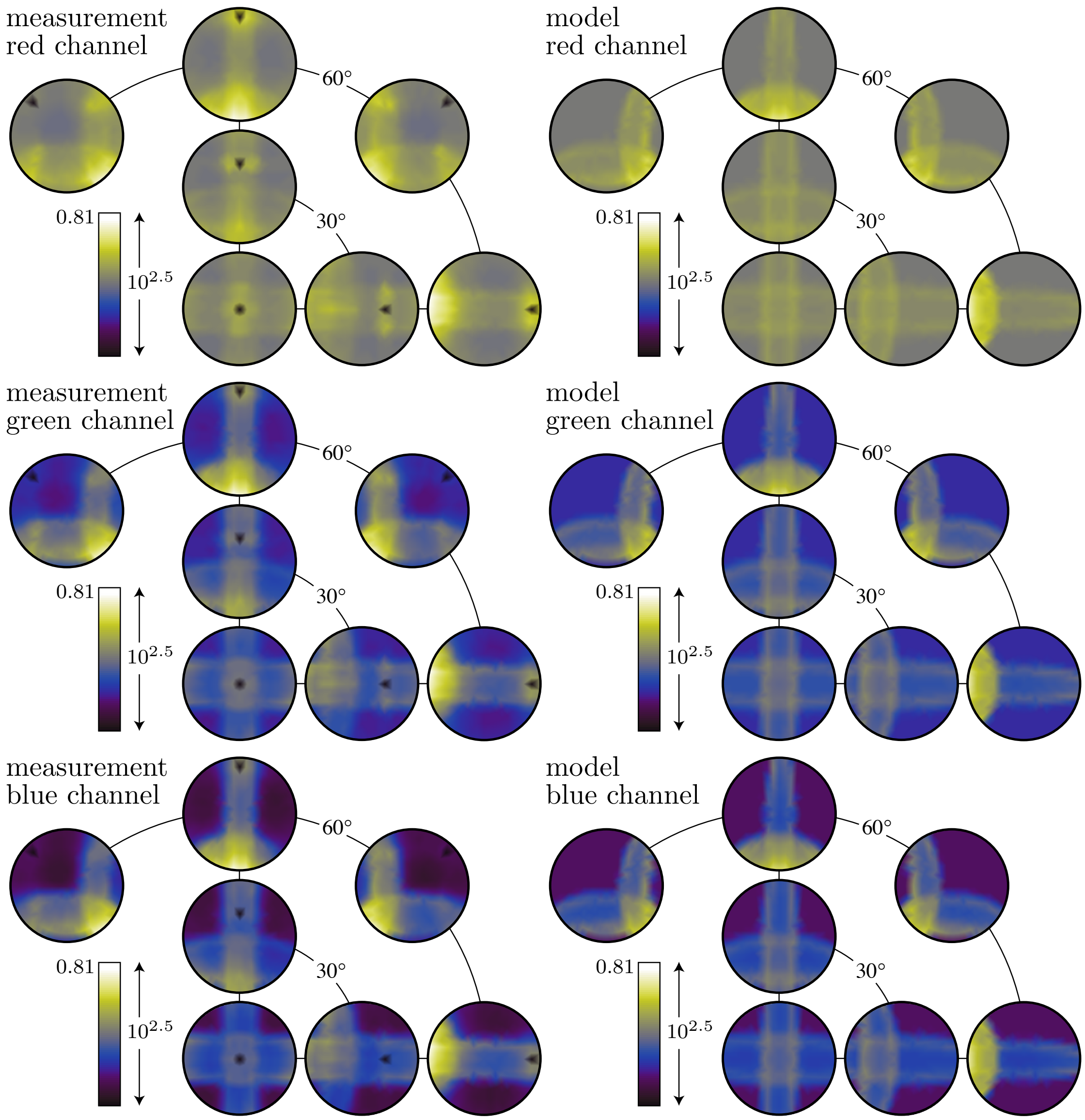

Figure 9.4: BRDF comparison: polyester lining cloth.

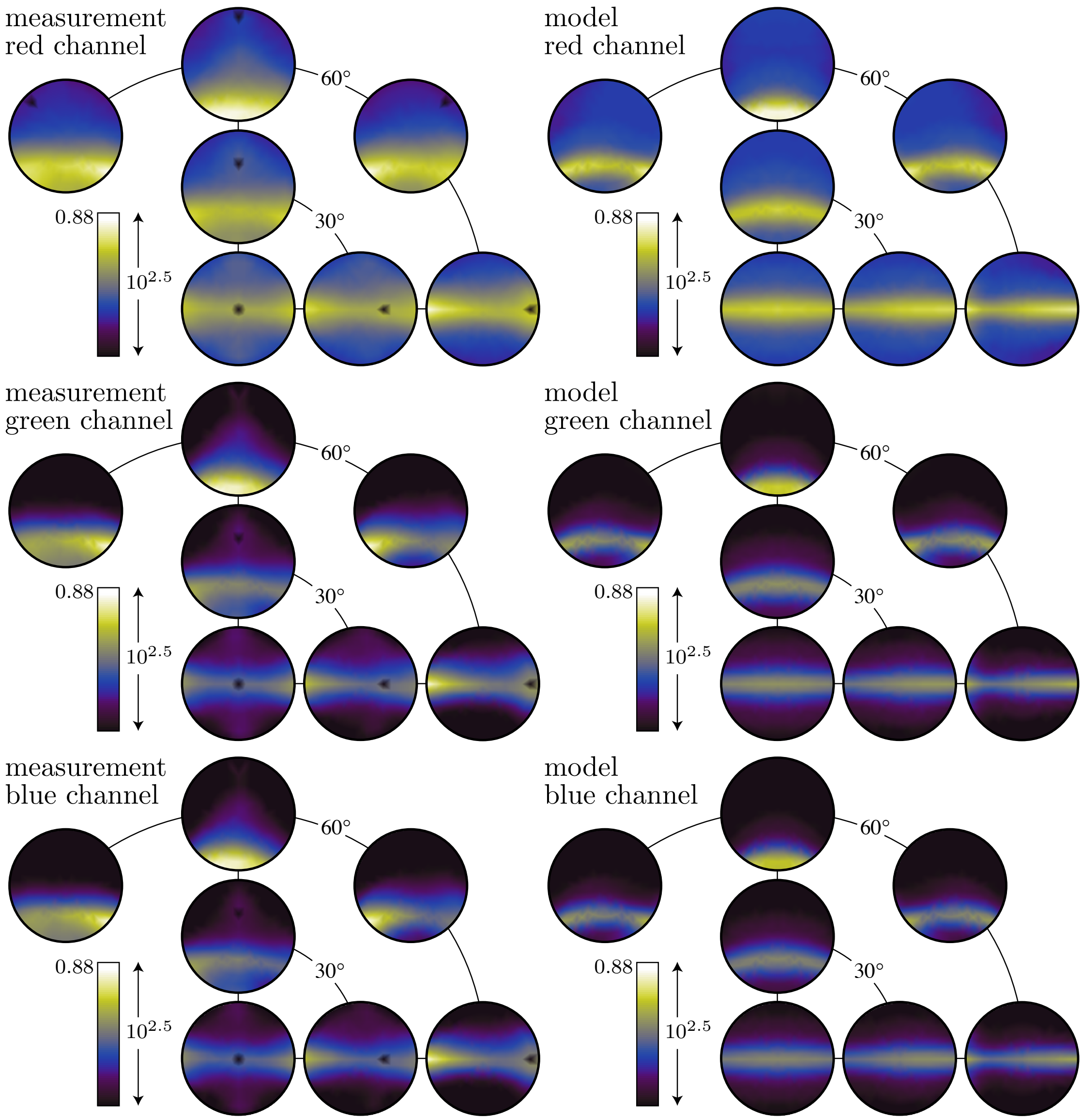

Figure 9.5: BRDF comparison: silk charmeuse.

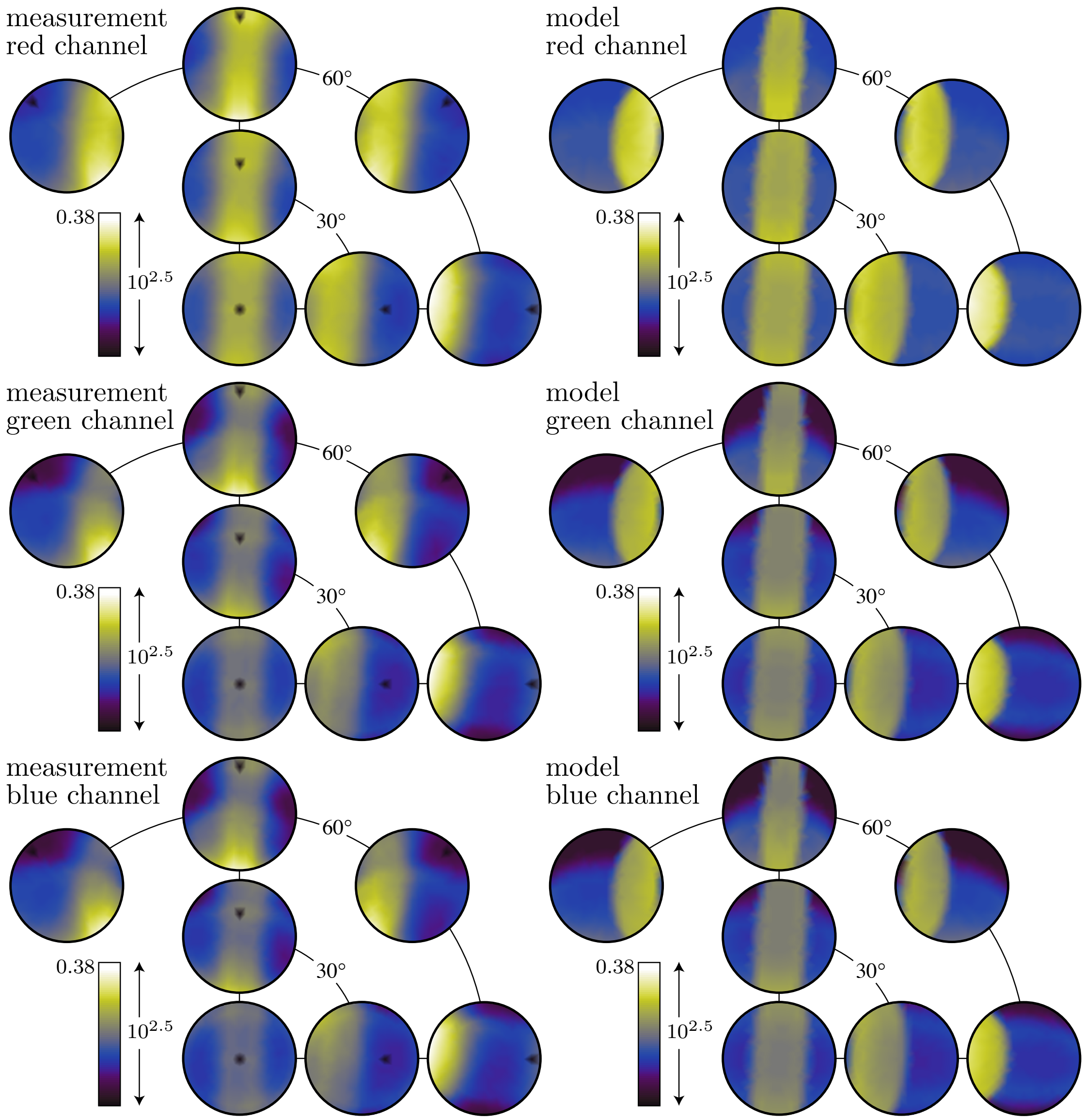

Figure 9.6: BRDF comparison: silk shantung.

bination of direct measurement and manual and automatic fitting. The model produces complex multi-component BRDFs, and fully automatic fitting proved unreliable because of the difficulty of balancing fit in highlights against more diffuse regions, fitting a weak weft component underneath the much brighter warp residual, and balancing texture appearance against BRDF fit.

The weave dimensions and approximate values of ψ were measured by observing the samples under a microscope, then $u_{\max}$, ψ, α, and β were chosen by plotting the model BRDF for a coarse grid of parameters and picking parameters to yield a good match to the measurement BRDF. For each setting of these parameters, automatic linear fitting was used to obtain specular and diffuse coefficients to match the data. Comparisons between the reality and the model can be seen in Figures 9.1, 9.2, 9.3, 9.4, 9.5, and 9.6.

The median relative error was 21%, 18%, 12%, 19%, 40%, and 28% for cotton twill, cotton denim, wool gabardine, polyester lining cloth, silk charmeuse, and silk shantung, respectively. The 80$^{\text{th}}$ percentile relative error was 36%, 34%, 27%, 39%, 69%, and 54%. Note that our fitting procedure did not attempt to minimize this error metric.

Using the same parameters as in the BRDF comparisons, we rendered animation sequences to match the known viewing, illumination, and surface geometry from the turntable videos (described in Chapter 5). To compare them to the videos (captured with a different camera), we computed a color space transformation from photographs of a standard color chart and applied it to put the rendered images in the color space of the photographs. Please refer to the accompanying video for the complete turntable sequences. Weave patterns of the fabrics we analyzed are shown in Figure 5.1.

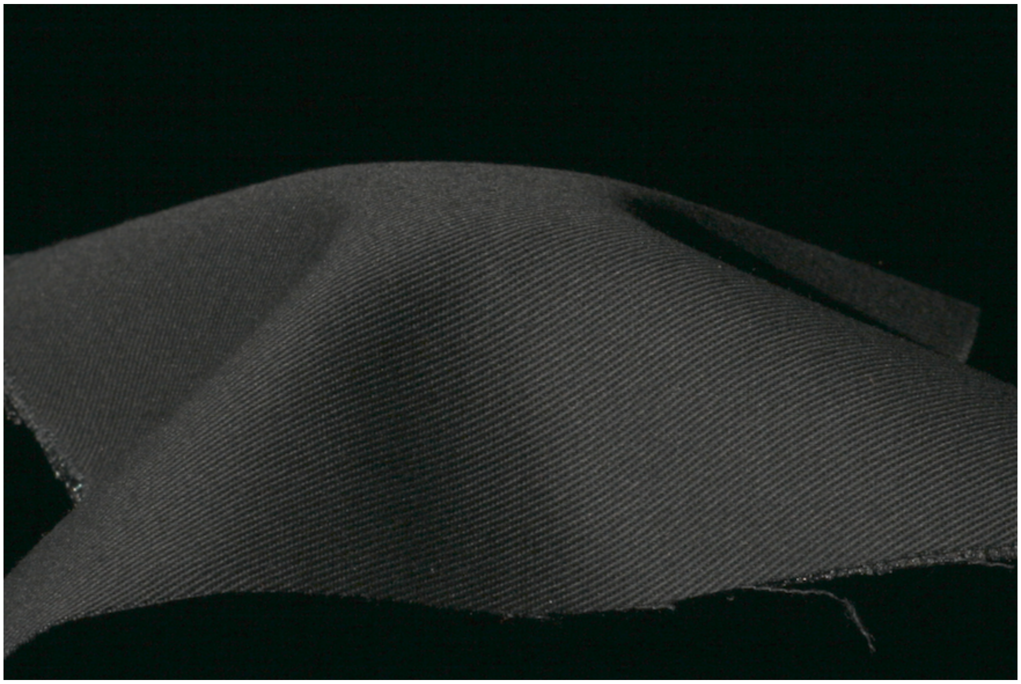

Figure 9.7: A frame from turntable video of cotton twill

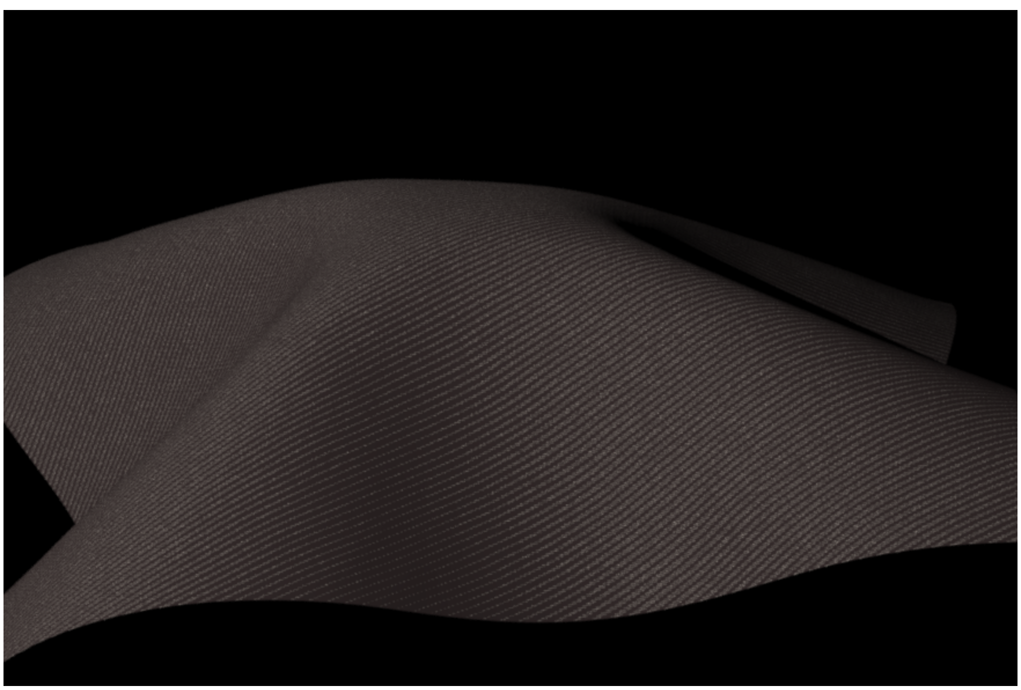

Figure 9.8: Rendering of cotton twill

Figure 9.9: A frame from turntable video of cotton denim

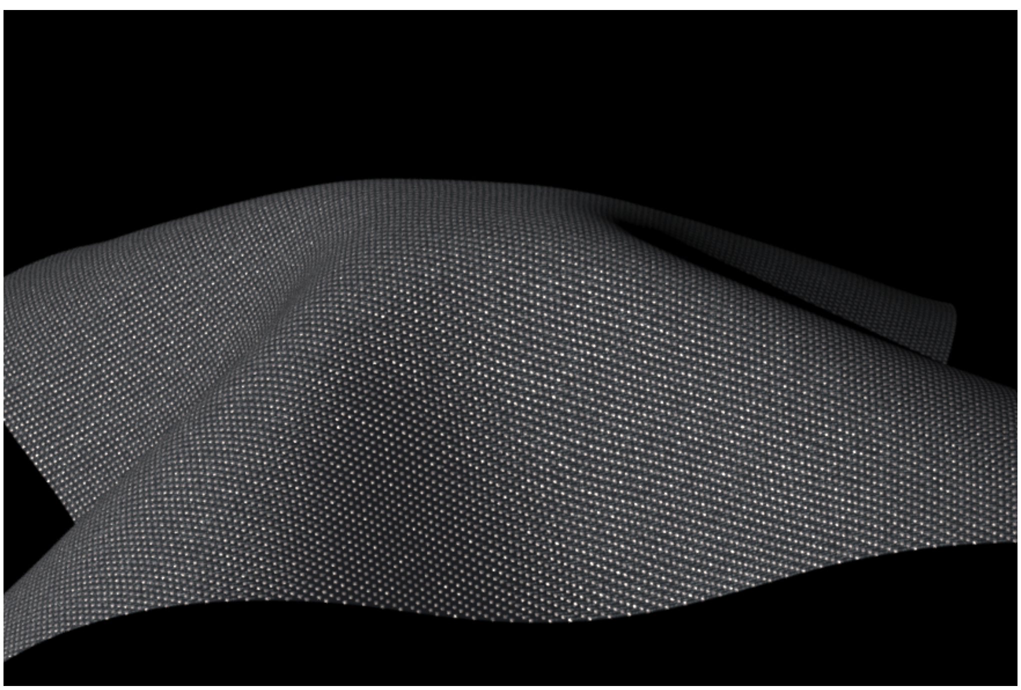

Figure 9.10: Rendering of cotton denim

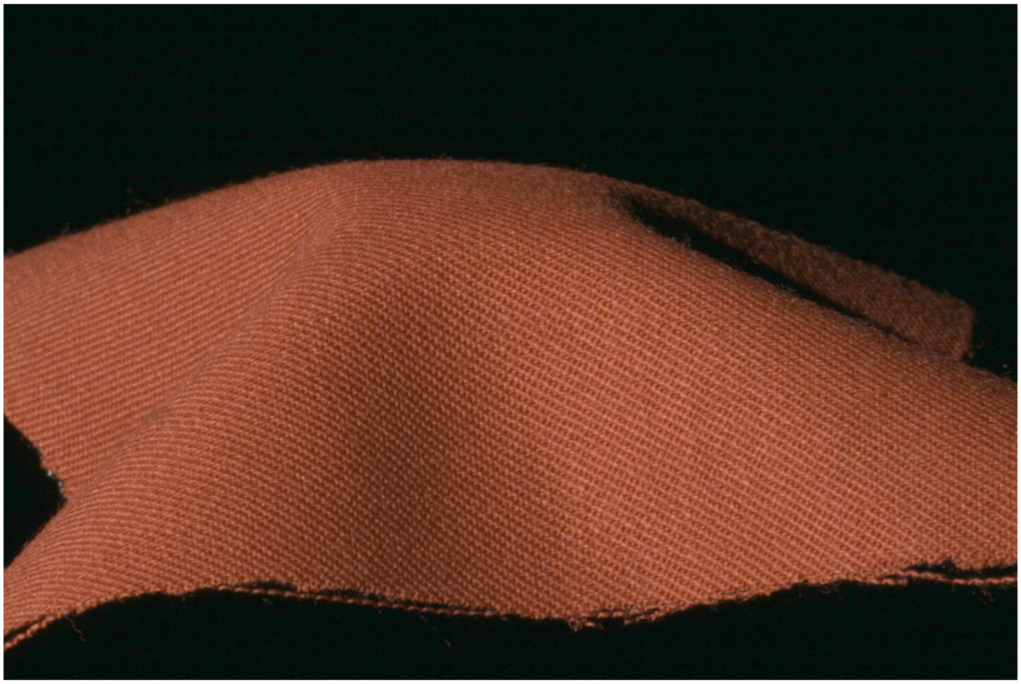

Figure 9.11: A frame from turntable video of wool gabardine

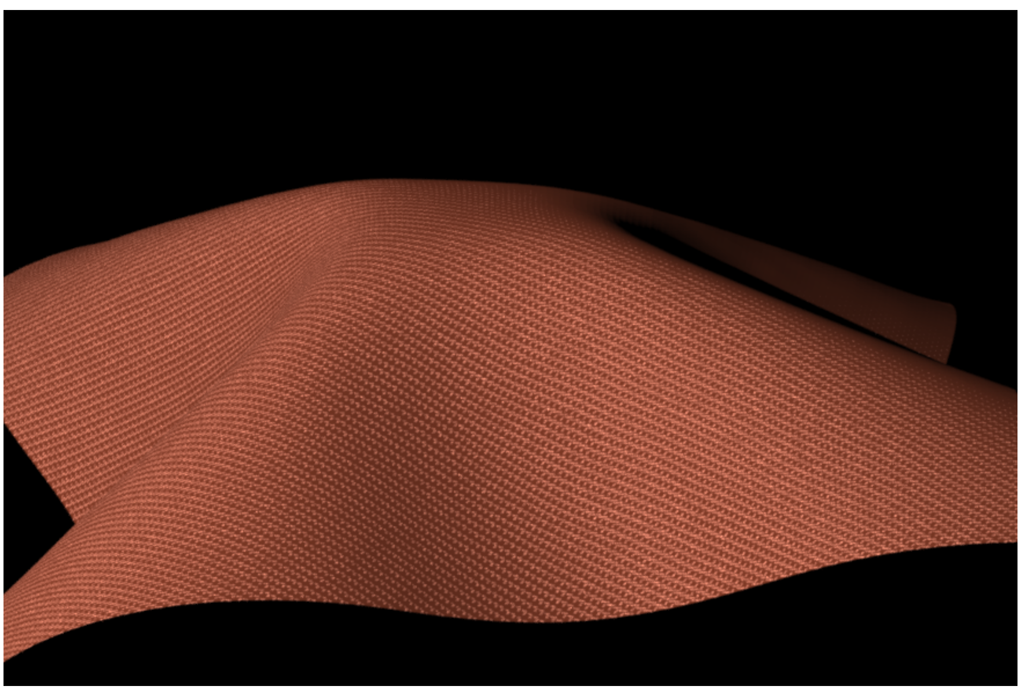

Figure 9.12: Rendering of wool gabardine

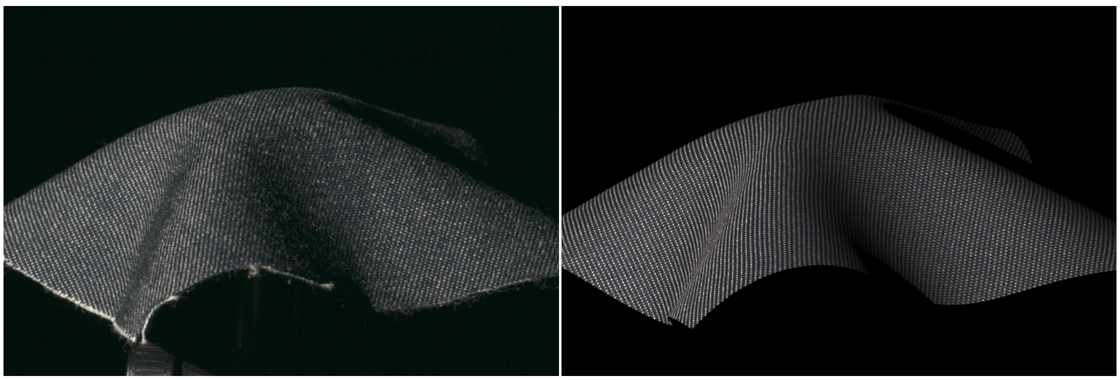

Figure 9.13: The darkening effect of shadowing and masking can be seen at grazing angle on denim (left image). Because our model lacks a shadowing and masking term, our rendered image (right image) doesn't have this darkening effect. This demonstrates the extent to which shadowing and masking affect the BRDF of cloth.

9.1 Staple Fabrics

The BRDFs of staple fabrics are asymmetrical with a forward-scattering lobe. This general structure is well matched by our model (though our forward-scattering lobe is not as strong as the reality). One interesting feature in the BRDFs is the darkening at grazing angles due to shadowing and masking. This effect can be observed in the accompanying turntable video, in particular on denim. However, it is relatively minor (see Figure 9.13) and suggests that shadowing and masking have less influence on the appearance of staple cloth than is commonly accepted.

Because of the fairly subtle BRDFs, texture is often the prominent feature of staple fabrics. Our model is able to replicate the twill ribs in cotton twill, including the small dots of reflections between the ribs. For cotton denim, we are able to model the white dots seen in the photograph and also the thin slivers of blue reflections between the white dots. The wool gabardine is coarser than the cotton twill with a higher ratio of weft to warp area and the red dots between the twill ribs are easier to notice here. Even though our texture model operates purely in a 2D manner (simple, blocky highlights on rectangles), the three fabrics rendered using our model give an illusion of depth and three-dimensional structure.

9.2 Filament Fabrics

The contribution of the warp and weft yarns to the BRDFs of filament fabrics can be easily discerned from looking at the BRDF plots. Filament fabrics with warp and weft yarns of the same color and brightness, such as our polyester lining cloth, have a cross shaped BRDF. In warp-dominated filament fabrics, such as our silk charmeuse, one of the bars of the cross is less prominent; conversely, in

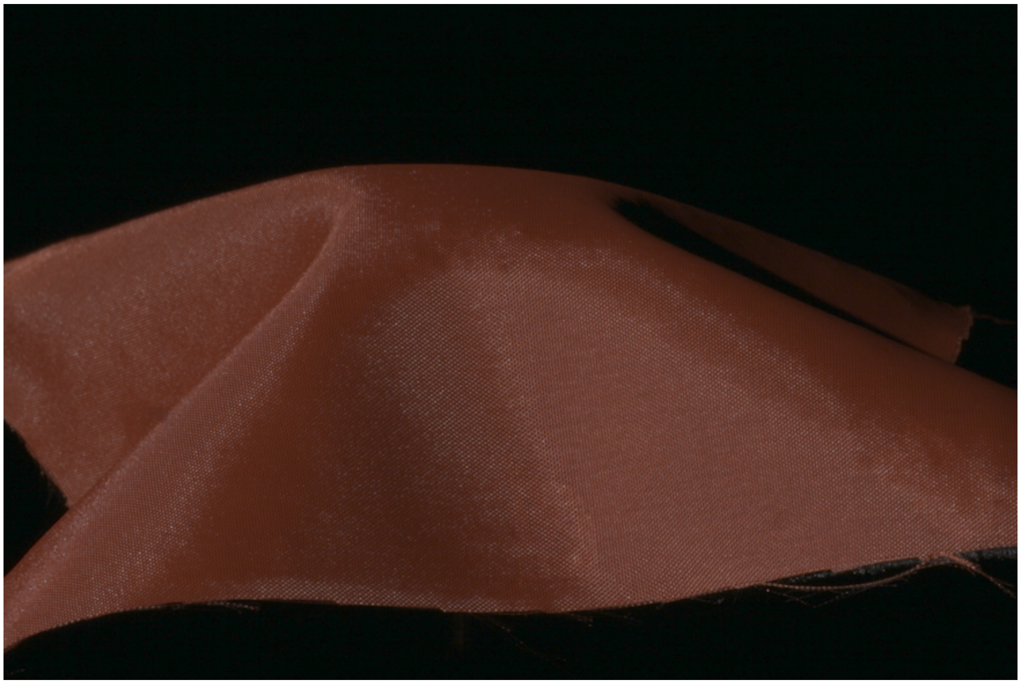

Figure 9.14: A frame from turntable video of polyester lining cloth

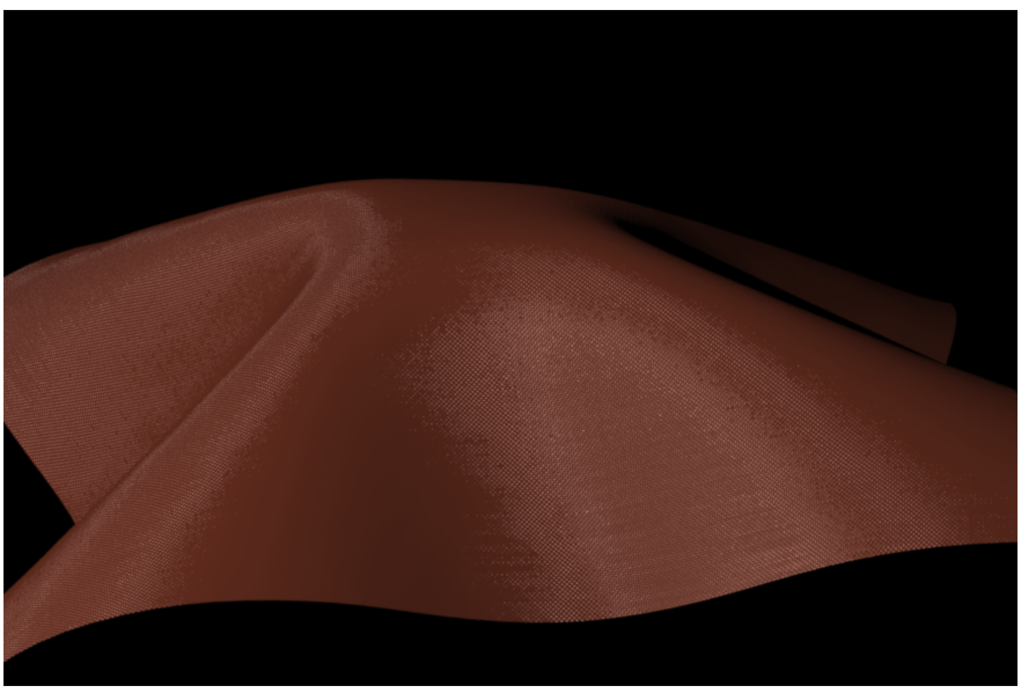

Figure 9.15: Rendering of polyester lining cloth

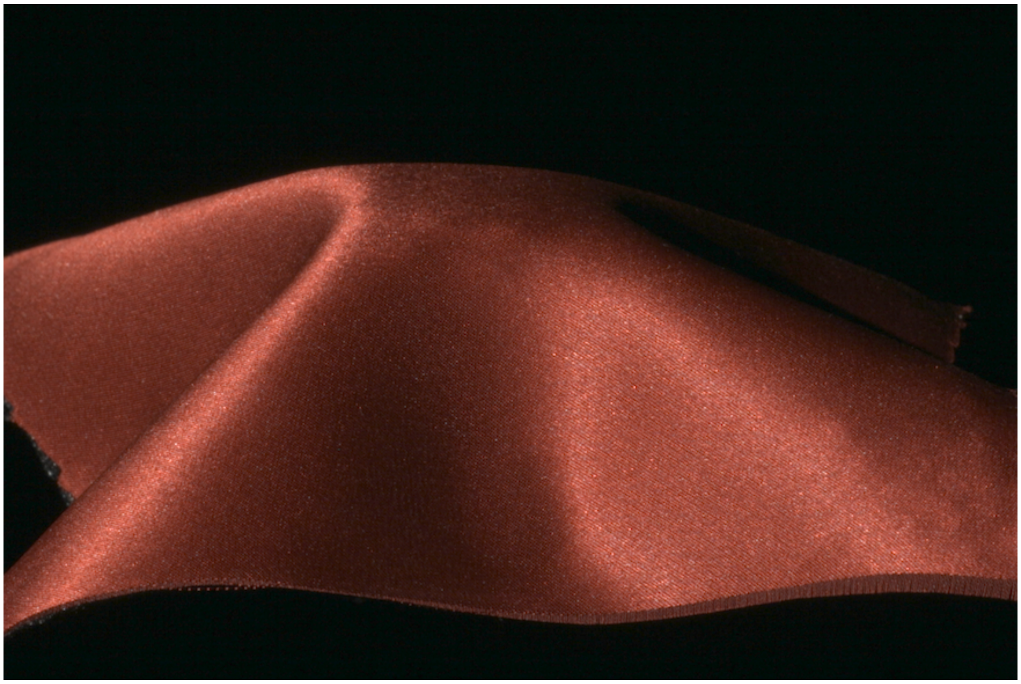

Figure 9.16: A frame from turntable video of silk charmeuse

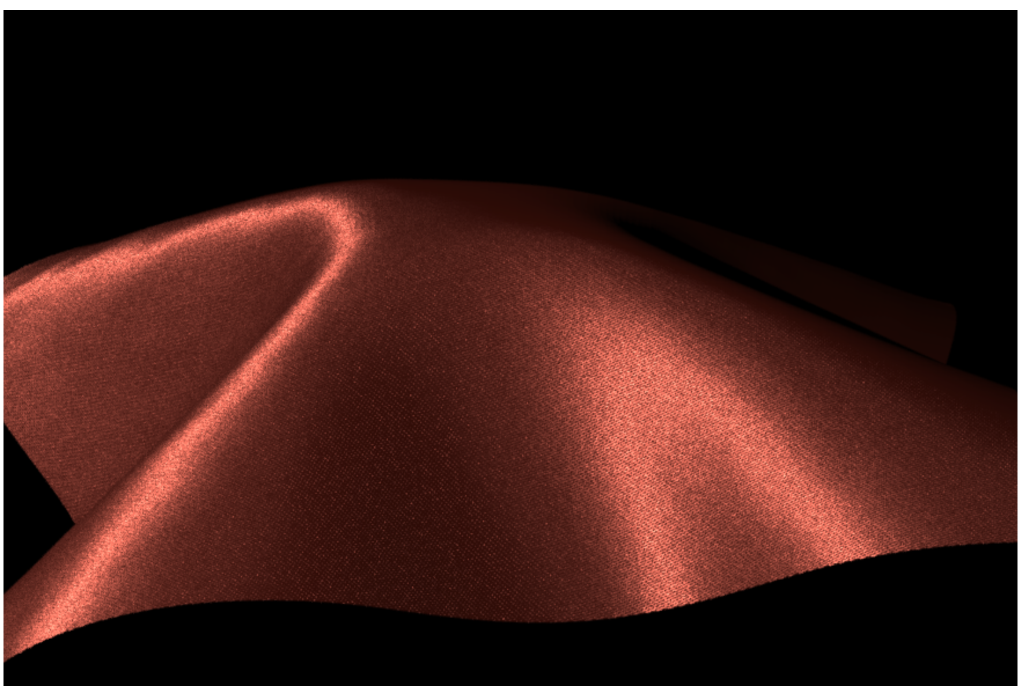

Figure 9.17: Rendering of silk charmeuse

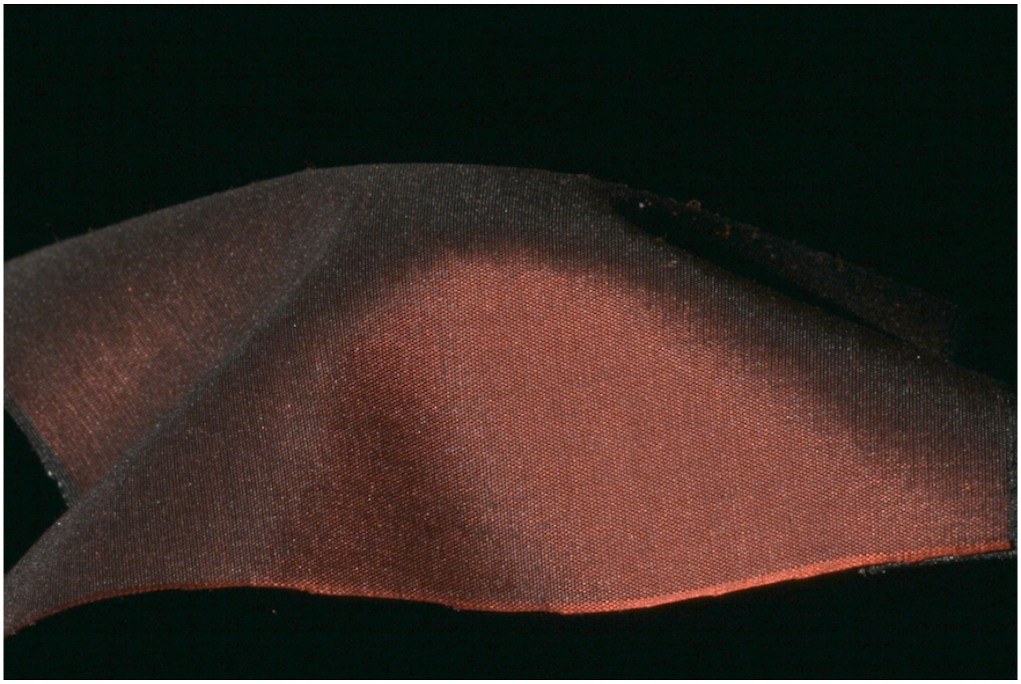

Figure 9.18: A frame from turntable video of silk shantung

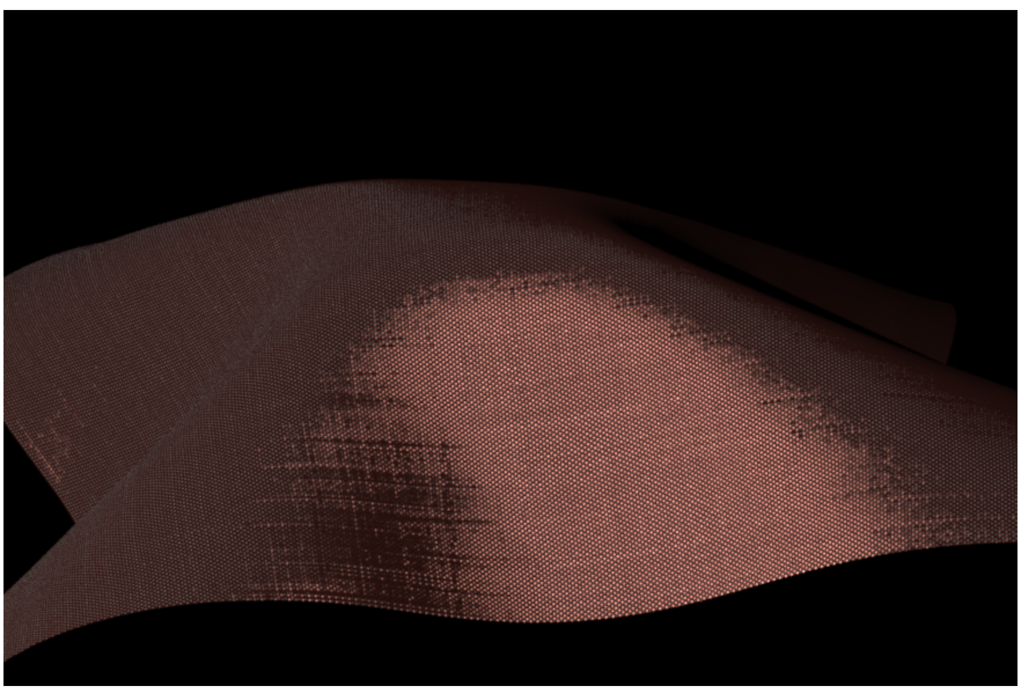

Figure 9.19: Rendering of silk shantung

weft-dominated fabrics, such as our silk shantung, the other bar is less prominent.

Polyester lining cloth demonstrates a superposition of two highlights, which is also predicted by our model. It also shows some irregularities along the edge of the highlights, which we modeled using the correlated noise described in the previous section. The edge-brightening effect seen in the photograph and the BRDF is modeled effectively by using a hyperbolic shape for the segment spine (as is appropriate for a tightly woven plain weave fabric). Silk charmeuse has much thinner and brighter highlights with no apparent edge-irregularity. Because this is a warp-dominated satin weave, we expect the warp segments to be prominent and the weft segments less so, which can be seen both in the BRDF and in the video. Silk shantung is woven with bright red weft yarns and darker warp yarns. Up close, the texture looks like a grid of red dots. Shantung shows strong irregularities along the edge of its highlights in form of cross-hatch formations. Similar to the polyester lining cloth, shantung is a plain weave fabric and shows a mild edge-brightering effect. The lack of good match for highlight profile in silk can be attributed to the properties of silk fibers (such as their unusual cross section) to be studied in future work.

9.3 Modeling New Fabrics

The examples we presented here were produced with a lot of effort to validate our model against reality. To use the model to produce images of new fabrics, it is not necessary to go through elaborate effort. Color and weave pattern (including segment rectangle width w and length l) can be observed. For relatively matte fabrics (staple fabrics and plain weave filament fabrics), the values $\alpha = 0.01$ and $\beta = 4.0$ work well; for shinier fabrics (such as charmeuse), a higher value of beta works better. On staple fabrics, $\delta = 0$; for filament fabrics, we can set $\delta = 0.5$. For staple fabrics, a value of $\psi = -30°$ or $\psi = 30°$ work well; $\psi = 0$ for filament fabrics. The value of $u_{\max}$ varies according to the weave pattern, but $u_{\max} = 30°$ is a good place to start. In twill weave and satin weave, the $u_{\max}$ for the more dominant yarn is smaller than the $u_{\max}$ of the less dominant yarn. The value of κ can be safely set to 0 for staple fabrics. For plain weave filament fabrics, κ should be set to a value less than 0 to model the edge-brightening effect. Conversely, $\kappa > 0$ works well for satin weave filament fabrics.

Chapter 10

Conclusion

The appearance of cloth depends on the textile fiber and production method. Among the many ways of transforming a collection of textile fibers into a piece of cloth, weaving is the most common method and woven cloth makes up the majority of commercial fabrics. Woven cloth is also interesting because its appearance varies greatly depending on the textile fibers and the weave pattern used, from the matte denim found in blue jeans to the shiny silk charmeuse. This work has presented an extensive study of light reflection from woven fabrics, starting from measurements and ending with a model for the appearance of woven cloth.

Our reflectance measurements show a variety of phenomena, ranging from sharp anisotropic highlights to asymmetric non-Lambertian diffuse patterns, and our model demonstrates that most of these features can be explained as resulting from specular reflection, once the structured geometry of the material is taken into account. The textures we produce, again using only specular highlights, capture the correct appearance over a remarkable range of conditions. These results are in contrast with the prevailing assumption that the most important features of the reflectance, and especially the texture, of fabrics with generally matte appearance are mainly due to diffuse reflection and shadowing–masking.

We expect our model will be useful in practice wherever realistic cloth appearance is needed. Although the derivation is fairly involved, the texture model itself is not difficult to evaluate. Although the full form of the BRDF model requires a numerical integration, the integrand is well behaved and the integration can be done with a simple numerical integration routine such as the Trapeziodal Rule.

One major advantage of using our model is that it doesn't require any data and thus can be used to model an arbitrary piece of fabric, even one that is not available or has not been manufactured. In contrast, data-based models do require BTF data of the fabric to be modeled. Not only does this require a large storage space, but it also is able to model only the specific fabric that has been captured and stored in the database. Our model also comes with physically meaningful parameters, which is very important for the users of this model to be able to tweak the appearance of the fabric to suit their particular need. This connection to the fabric properties is also important for textile applications. Ultimately, our goal is to extend the range of analytical models by making one for woven cloth available.

The framework we have established in order to build our model can be used to build other, more sophisticated fabric scattering models as future work. Research should be done into appropriate phase function models; the empirical forward-scattering function we use is just a start and a better model should be developed based on actual measurements of the scattering properties of textile fibers and yarns.

More sophisticated models for attenuation that dissipate light according to the distance it travels can also be used. Measurements of light transmission from a piece of cloth should be done. With proper analysis, it may be possible to further expand this to a model of transmission of light.

We have ignored inter-yarn interactions in order to concentrate on specular reflection, but some effects of these interactions are visible in the data. For instance, the white weft dots in denim disappear in the turntable photographs at grazing angles, and the warp component of charmeuse shows a sharpening for grazing angles that we conjecture is a shadowing effect (vertical features in the center column of the data). In order to correctly predict the appearance of materials with dissimilar warp and weft tensions or colors, a model for shadowing/masking is required. One idea is to use the idea of horizon mapping to model the height difference between the valleys and the hills of a piece of woven cloth.

To improve the appearance of rougher pieces of cloth made of wool, a model for stray fibers is required, possibly by using randomly generated curves on the surface of the cloth.

Finally, it would be interesting to extend this framework to model knitwear; instead of using conic sections to model the spine curve, we can use more complex curves to model the way yarns form loops in a knitwear. This transition from plane curves to general 3D curves will affect the specular reflections from the yarns. The yarns themselves are no longer arranged in rectangular segments and a new way to represent them will be needed.

BIBLIOGRAPHY

[1] Neeharika Adabala, Nadia Magnenat-Thalmann, and Guangzheng Fei. Visualization of woven cloth. In *EGRW '03: Proceedings of the 14th Eurographics workshop on Rendering*, pages 178–185, Aire-la-Ville, Switzerland, Switzerland, 2003. Eurographics Association.

[2] George B. Arfken, Hans J. Weber, and Hans-Jurgen Weber. *Mathematical Methods for Physicists*, chapter 11.5. Academic Press, 4^{th} edition, 1995.

[3] Michael Ashikhmin, Simon Premože, and Peter Shirley. A microfacet-based brdf generator. In *SIGGRAPH '00: Proceedings of the 27th annual conference on Computer graphics and interactive techniques*, pages 65–74, New York, NY, USA, 2000. ACM Press/Addison-Wesley Publishing Co.

[4] George S. Buck and Frank A. McCord. Luster and cotton. *Textile Research Journal*, 19:715–751, 1949.

[5] Yanyun Chen, Stephen Lin, Hua Zhong, Ying-Qing Xu, Baining Guo, and Heung-Yeung Shum. Realistic rendering and animation of knitwear. *IEEE Transactions on Visualization and Computer Graphics*, 9(1):43–55, 2003.

[6] A. K. Roy Choudhury. *Textile Preparation and Dyeing*. Science Publishers, 2006.

[7] Kristin J. Dana, Bram van Ginneken, Shree K. Nayar, and Jan J. Koenderink. Reflectance and texture of real-world surfaces. *ACM Trans. Graph.*, 18(1):1–34, 1999.

[8] Jon Dattorro. *Convex Optimization & Euclidean Distance Geometry*, chapter Appendix D, pages 527–554. Meboo Publishing USA, Palo Alto, California, 2005.

[9] Katja Daubert, Hendrik P. A. Lensch, Wolfgang Heidrich, and Hans-Peter Seidel. Efficient cloth modeling and rendering. In *Proceedings of the 12th Eurographics Workshop on Rendering Techniques*, pages 63–70, London, UK, 2001. Springer-Verlag.

[10] Katja Daubert and Hans-Peter Seidel. Hardware-based volumetric knit-wear. *Comput. Graph. Forum*, 21(3), 2002.

[11] Frédéric Drago and Norishige Chiba. Painting canvas synthesis. *Vis. Comput.*, 20(5):314–328, 2004.

[12] Philip Dutré, Philippe Bekaert, and Kavita Bala. *Advanced Global Illumination*. A K Peters, Natick, USA, 2003.

[13] Merran Evans, Nicholas Hastings, and Brian Peacock. *Statistical Distributions*, chapter 41. Wiley-Interscience, 3^{rd} edition, 2000.

[14] Carlos Felippa. *Introduction to Finite Element Methods*, chapter Appendix D. Department of Aerospace Engineering Sciences, University of Colorado at Boulder, 2006.

[15] Andrew Glassner. Digital weaving, part 1. *IEEE Computer Graphics and Applications*, 22(6):108–118, 2002.

[16] Andrew Glassner. Digital weaving, part 2. *IEEE Computer Graphics and Applications*, 23(1):77–90, 2003.

[17] Andrew Glassner. Digital weaving, part 3. *IEEE Computer Graphics and Applications*, 23(2):80–89, 2003.

[18] Alfred Gray. *Modern Differential Geometry of Curves and Surfaces with Mathematica*, chapter 12.3, pages 279–280. CRC Press, Boca Raton, FL, USA, 2^{rd} edition, 1997.

[19] Eduard Gröller, René T. Rau, and Wolfgang Straßer. Modeling and visualization of knitwear. *IEEE Transactions on Visualization and Computer Graphics*, 1(4):302–310, 1995.

[20] Eduard Gröller, René T. Rau, and Wolfgang Straßer. Modeling textiles as three dimensional textures. In *Proceedings of the eurographics workshop on Rendering techniques '96*, pages 205–ff., London, UK, 1996. Springer-Verlag.

[21] Pat Hanrahan and Wolfgang Krueger. Reflection from layered surfaces due to subsurface scattering. In *SIGGRAPH '93: Proceedings of the 20th annual conference on Computer graphics and interactive techniques*, pages 165–174, New York, NY, USA, 1993. ACM Press.

[22] R. S. Hunter and R. W. Herald. *The measurement of appearance*, page 285. Wilet-Interscience, New York, NY, USA, 2^{nd} edition, 1987.

[23] Harold Jeffreys and Bertha S. Jeffreys. *Methods of Mathematical Physics*, chapter 2.092-2.094, pages 75–76. Cambridge University Press, Cambridge, England, 3^{rd} edition, 1988.

[24] Sara J. Kadolph and Anna L. Langford. *Textiles.* Prentice Hall, 10^{th} edition, 2006.

[25] Jan Kautz, Solomon Boulos, and Frédo Durand. Interactive editing and modeling of bidirectional texture functions. *ACM Trans. Graph.*, 26(3):53, 2007.

[26] Menachem Lewin, editor. *Handbook of Fiber Chemistry.* CRC Press, 3^{rd} edition, 2007.

[27] Rong Lu, Jan J. Koenderink, and Astrid M. L. Kappers. Optical properties (bidirectional reflection distribution functions) of velvet. *Applied Optics*, 37(25):5974–5984, 1998.

[28] Rong Lu, Jan J. Koenderink, and Astrid M. L. Kappers. Specularities on surfaces with tangential hairs or grooves. *Comput. Vis. Image Underst.*, 78(3):320–335, 2000.

[29] Stephen R. Marschner, Stephen H. Westin, Adam Arbree, and Jonathan T. Moon. Measuring and modeling the appearance of finished wood. In *SIGGRAPH '05: ACM SIGGRAPH 2005 Papers*, pages 727–734, New York, NY, USA, 2005. ACM Press.

[30] David K. McAllister, Anselmo Lastra, and Wolfgang Heidrich. Efficient rendering of spatial bi-directional reflectance distribution functions. In *HWWS '02: Proceedings of the ACM SIGGRAPH/EUROGRAPHICS conference on Graphics hardware*, pages 79–88, Aire-la-Ville, Switzerland, Switzerland, 2002. Eurographics Association.

[31] Michael Meißner and B. Eberhardt. The art of knitted fabrics, realistic & physically based modeling of knitted fabrics. *Comput. Graph. Forum*, 17(3):355–362, 1998.

[32] Addy Ngan, Frédo Durand, and Wojciech Matusik. Experimental analysis of brdf models. In *Proceedings of the Eurographics Symposium on Rendering*, pages 117–126. Eurographics Association, 2005.

[33] F. E. Nicodemus, J. C. Richmond, J. J. Hsia, I. W. Ginsberg, and T. Limperis. Geometric considerations and nomenclature for reflectance. Monograph 161, National Bureau of Standards (US), 1977.

[34] Julie Parker. *All about cotton: a fabric dictionary & swatchbook / written and illustrated by Julie Parker*. Rain City Pub., 1993.

[35] Fabio Pellacini and Jason Lawrence. Appwand: editing measured materials using appearance-driven optimization. *ACM Trans. Graph.*, 26(3):54, 2007.

[36] Sylvia C. Pont and Jan J. Koenderink. Split off-specular reflection and surface scattering from woven materials. *Applied Optics*, 42:1526–1533, 2003.

[37] Mirko Sattler, Ralf Sarlette, and Reinhard Klein. Efficient and realistic visualization of cloth. In *EGRW '03: Proceedings of the 14th Eurographics workshop on Rendering*, pages 167–177, Aire-la-Ville, Switzerland, Switzerland, 2003. Eurographics Association.

[38] Peter Shirley and Kenneth Chiu. A low distortion map between disk and square. *J. Graph. Tools*, 2(3):45–52, 1997.

[39] A. Sirikasemlert and X. Tao. Effects of fabric parameters on specular reflection of single-jersey knitted fabrics. *Textile Research Journal*, 69:663–675, 1999.

[40] X. Tao and A. Sirikasemlert. A three-dimensional analysis of specular reflection from single-jersey knitted fabrics. *Textile Research Journal*, 69:43–51, 1999.

[41] Economic Research Service USDA. Usda briefing room - cotton, August 2007.

[42] Vladimir L. Volevich, Edward A. Kopylov, Andrei B. Khodulev, and Olga A. Karpenko. An approach to cloth synthesis and visualization. In *Proceedings of GRAPHICON '97*, 1997.

[43] Eric W. Weisstein. Hyperbola. *MathWorld—A Wolfram Web Resource*, May 2004.

[44] Eric W. Weisstein. Parabola. *MathWorld—A Wolfram Web Resource*, August 2004.

[45] Eric W. Weisstein. Cross product. *MathWorld—A Wolfram Web Resource*, June 2005.

[46] Eric W. Weisstein. Dot product. *MathWorld—A Wolfram Web Resource*, March 2005.

[47] Eric W. Weisstein. Ellipse. *MathWorld—A Wolfram Web Resource*, January 2006.

[48] Eric W. Weisstein. Rotation matrix. *MathWorld—A Wolfram Web Resource*, November 2006.

[49] T. Welford. *The textiles student's manual: an outline of all textile processes, from the origin of the fibre to the finished cloth.* Pitman, London, 1967.

[50] Stephen H. Westin, James R. Arvo, and Kenneth E. Torrance. Predicting reflectance functions from complex surfaces. In *SIGGRAPH '92: Proceedings of the 19th annual conference on Computer graphics and interactive techniques*, pages 255–264, New York, NY, USA, 1992. ACM Press.

[51] Ying-Qing Xu, Yanyun Chen, Stephen Lin, Hua Zhong, Enhua Wu, Baining Guo, and Heung-Yeung Shum. Photorealistic rendering of knitwear using the lumislice. In *SIGGRAPH '01: Proceedings of the 28th annual conference on Computer graphics and interactive techniques*, pages 391–398, New York, NY, USA, 2001. ACM Press.

[52] Takami Yasuda, Shigeki Yokoi, Jun ichiro Toriwaki, and Katsuhiko Inagaki. A shading model for cloth objects. *IEEE Comput. Graph. Appl.*, 12(6):15–24, 1992.